Measurement of the Hadronic Photon Structure Function $F_2^\gamma(x, Q^2)$ in Two-Photon Collisions

DISSERTATION
zur Erlangung des Grades
eines Doktors der Naturwissenschaften

vorgelegt von
Dipl.-Phys. Johannes Heß
aus Siegen

eingereicht beim Fachbereich 7
der Universität Siegen

Siegen 2002

Gutachter der Dissertation: Prof. Dr. S. Brandt
Prof. Dr. C. Grupen
Datum der Disputation: 20. Dezember 2002

Internetpublikation der Universitätsbibliotek Siegen:
Uniform Resource Name: **urn:nbn:de:hbz:467-249**

Contents

Chapter 1

Introduction

The photon is surely one of the most important elementary particles, and consequently its interaction and structure is of extraordinary interest. In the classical theory of light there is no interaction between light waves, even the photon as a particle does not exist. But quantum field theory allows that photons fluctuate into pairs of charged particles over a short period of time due to the Heisenberg uncertainty principle and in this way can interact with each other. e^+e^- colliders like LEP at CERN provide an experimental environment in which high energy photons are produced with sufficient luminosity so that interesting two-photon experiments can be performed.

In this thesis the hadronic structure function $F_2^\gamma(x, Q^2)$ of the photon is measured. Hadron production in two-photon collisions is an active field of research and provides many opportunities to check theoretical predictions, for example from QCD. A brief explanation of the theoretical background and a motivation for this analysis will be given in chapter 2.

The data analyzed were taken in the years 1998, 1999 and 2000 at centre-of-mass energies between $\sqrt{s_{e^+e^-}} = 189\,\mathrm{GeV}$ and $\sqrt{s_{e^+e^-}} = 207\,\mathrm{GeV}$ with the ALEPH detector. Overall an integrated luminosity of $548.4\,\mathrm{pb}^{-1}$ has been used. The important features of the ALEPH detector will be introduced in chapter 3.

Detector acceptance problems and inefficiencies turn out to be the major difficulties in the measurement of the structure function F_2^γ. These can be solved with standard techniques which are discussed in chapter 4. An important issue will be the discussion of uncertainties and error propagation.

The selection of the data sample as well as the discussion and treatment of background sources can be found in chapter 5. The Monte-Carlo simulations are then explained in the following chapter where also a comparison between observed data and the simulations can be found.

The details of the measurement, especially the extraction of the structure function $F_2^\gamma(x, Q^2)$ from the differential cross section and the final results are given in chapter 7. The results are compared to different theoretical models and to measurements from other experiments.

Chapter 2

Theory

2.1 Photon-Photon Interaction

Reactions of the form

$$e^+e^- \to e^+e^-\gamma^*\gamma^* \to e^+e^-X. \tag{2.1}$$

are understood as two photon collisions at electron-positron storage rings like LEP. They can be seen as a two step process. The leptons of the particle beam emit photons, which due to the kinematic situation at the $e\gamma$ vertex must be virtual. The process of emission can be calculated in the framework of QED to high accuracy. Therefore the leptons of the storage ring can be seen as a well defined source of a photon beam. These photons then collide with each other and produce a final state system X in the second step of the process (2.1).

In the classical theory of electrodynamics photons do not interact with each other. In Quantum Electrodynamics (QED) the photon is the gauge boson which is structureless and has no self coupling since the gauge group of QED is Abelian. It only interacts with electrical charge. For that it is called the "bare" or "direct" photon. But due to the Heisenberg uncertainty principle it is possible that the photon fluctuates into particle and antiparticle. This pair of particles must have the same quantum numbers as the photon for the duration of such a fluctuation. A time interval is given by the uncertainty principle[1]:

$$\Delta t \cdot \Delta E \approx 1 \tag{2.2}$$

ΔE represents the energy difference between photon and particle pair. For the time window allowed for a short violation of energy conservation an estimate can

[1] Throughout this thesis $\hbar = c = 1$ is used.

be determined as

$$\Delta t \approx \frac{1}{\Delta E} = \frac{1}{E_{f\bar{f}} - E_\gamma} = \frac{1}{\sqrt{m_{f\bar{f}}^2 + k^2} - \sqrt{q^2 + k^2}} \tag{2.3}$$

$$\approx \frac{2E_\gamma}{m_{f\bar{f}}^2 + Q^2}, \tag{2.4}$$

where E_γ is the energy of the photon and $E_{f\bar{f}}$ and $m_{f\bar{f}}$ are energy and mass of the particles in the state of fluctuation. $\vec{k}$ is the wave number vector of the photon and q its four vector. The square of this four vector is negative since the virtual photon is spacelike. While the photon is fluctuating, the produced particles can interact with other particles in their surrounding. The photon now is resolved and shows a structure. If the photon fluctuates into a pair of lepton and antilepton, the final state X will (in lowest order) be leptonic and the process can be calculated by QED. Fluctuations into pairs of quarks and antiquarks will lead to hadronic final states which are an interesting field for quantumchromodynamics (QCD) and will be the main subject of the studies in this thesis. In contrast to the leptonic final states the $q\bar{q}$ production cannot be calculated easily since it is not amenable to a perturbative approach over a large kinematic region.

The subscript $f\bar{f}$ indicates that only pairs of charged fermions can be produced, that means all kinds of known charged leptons and quarks, excluding the top quark that cannot be produced in pairs at LEPII energies due to its high mass. In principle also fluctuations into pairs of charged gauge bosons of the weak interaction $\mathrm{W^+W^-}$ are possible. But the mass of these pairs is so large that their contribution to our processes is negligible. In future linear colliders this will be an interesting field of research and unfortunately also a source of high background rates.

2.2 Kinematics and Cross Section

The basic kinematics of a two-photon process is shown in Fig. 2.1.

The quantities p_i and E_i are the four momentum vectors and energies of the two beam leptons ($i = 1, 2$), primes are attached to the same quantities after scattering. The angles Θ_i' are the angles of the scattered leptons with respect to the beam axis. The two photons have the four momenta q_1 and q_2, for convenience they are ordered $q_1^2 < q_2^2$. Some important quantities are defined:

$$Q^2 = -q_1^2 \approx 2E_1E_1'(1 - \cos\Theta_1') \quad , \tag{2.5}$$

$$P^2 = -q_2^2 \approx 2E_2E_2'(1 - \cos\Theta_2') \quad ,$$

$$x = \frac{Q^2}{2q_1 \cdot q_2} = \frac{Q^2}{Q^2 + W^2 + P^2} \quad , \tag{2.6}$$

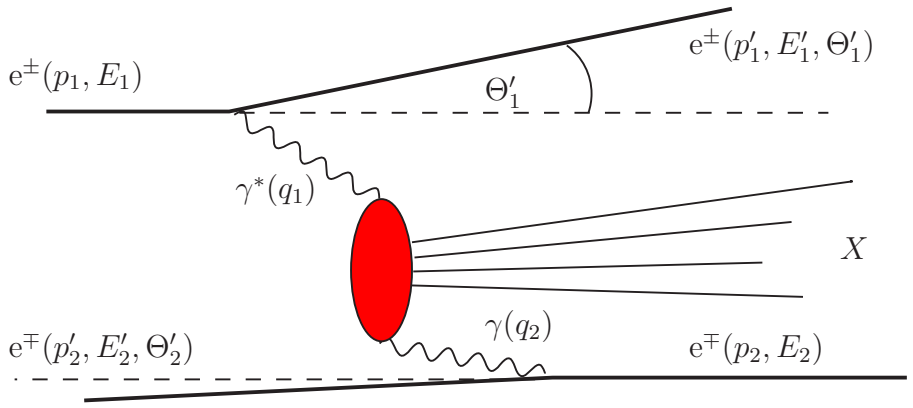

Figure 2.1: Basic diagram for the two-photon interaction between a highly virtual photon and a quasi real one.

$$\begin{aligned} W^2 &= (q_1+q_2)^2 = Q^2\frac{1-x}{x} - P^2 \quad , \\ r &= E_\gamma / E_{\text{beam}} \quad . \end{aligned} \tag{2.7}$$

E_γ is the energy of the highly virtual photon. An expression for the cross section of the process $e^+e^- \to e^+e^-\gamma^*\gamma^* \to e^+e^-X$ can be found. It separates the contributions of different helicities and polarizations [1]:

$$\begin{aligned} \mathrm{d}\sigma &= \frac{\alpha_{\text{em}}^2}{16\pi^2 q_1^2 q_2^2}\left[\frac{(q_1q_2)^2 - q_1^2q_2^2}{(p_1p_2)^2 - m_e^2m_e^2}\right]^{\frac{1}{2}} \times \\ &\times \Big[4\rho_1^{++}\rho_2^{++}\sigma_{\text{TT}} + 2|\rho_1^{+-}\rho_2^{+-}|\tau_{\text{TT}}\cos 2\tilde{\phi} + 2\rho_1^{++}\rho_2^{00}\sigma_{\text{TL}} + \\ &+ 2\rho_1^{00}\rho_2^{++}\sigma_{\text{LT}} + \rho_1^{00}\rho_2^{00}\sigma_{\text{LL}} - 8|\rho_1^{+0}\rho_2^{+0}|\tau_{\text{TL}}\cos\tilde{\phi}\Big]\frac{\mathrm{d}^3p_1'\mathrm{d}^3p_2'}{E_1'E_2'} \end{aligned} \tag{2.8}$$

In addition to the already defined quantities and the fine structure constant α_{em} the matrices $\rho_i^{\alpha\beta}$ and cross sections σ_{ab}, respectively, interference terms τ_{ab} appear. The density matrices $\rho_i^{\alpha\beta}$ only depend on q, p, p_1 and p_2 and on the electron mass m_e. They describe the helicity of the photons. The subscript i indicates to which photon the matrix refers, α, β stand for the three possible helicity states (+,–,0). For a more detailed discussion and explicit formula see [1].

The cross sections σ_{TT}, σ_{TL}, σ_{LT} and σ_{LL} and the interference terms τ_{TT} and τ_{TL} are the contributions to the total cross section from the interaction of transversely (T) and longitudinally (L) polarized photons. $\tilde{\phi}$ is the angle between the scattering planes of the two beam leptons.

Whereas the terms outside the second square brackets are fully described by quantities of the eγ vertex, the terms inside the brackets only refer to the

photon-photon interaction itself. The two steps of process (2.1) can therefore be separated in the cross section formula. The contribution of the eγ vertex and the produced photon spectrum can be calculated under the assumption of not too high virtualities. The details of that calculation will not be dealt with here. Only the results of the so called "Equivalent Photon Approximation" (EPA) [2] will be given. The photon spectrum emitted from the electron beams is of the form [3, 4]

$$\frac{\mathrm{d}N_\gamma}{\mathrm{d}\omega_i} = \frac{\alpha_{\mathrm{em}}}{2\pi}\frac{1}{\omega_i}\left[\left[1+(1-\omega_i)^2\right]\ln\left(\frac{Q^2_{\mathrm{max}}}{Q^2_{\mathrm{min}}}\right) - (1-\omega_i)\left(1-\frac{Q^2_{\mathrm{min}}}{Q^2_{\mathrm{max}}}\right)\right] \tag{2.9}$$

with the energy of the emitted photons ω_i, $i = 1, 2$ and the limits Q^2_{min} and Q^2_{max} which are directly given by the angles of the scattered electrons. Eqn. (2.9) is known as Weizsäcker–Williams approximation. For small angles $m_{\mathrm{e}}/E_{\mathrm{beam}} \ll \Theta_{\mathrm{min}} < \Theta < \Theta_{\mathrm{max}} \ll 1$

$$\frac{Q^2_{\mathrm{max}}}{Q^2_{\mathrm{min}}} = \left(\frac{\Theta_{\mathrm{max}}}{\Theta_{\mathrm{min}}}\right)^2 . \tag{2.10}$$

The kinematic limit for $\Theta = 0$ is reached at

$$Q^2_{\mathrm{min}} = \frac{m^2_{\mathrm{e}}\omega}{1-\omega} + \mathcal{O}(m^4_{\mathrm{e}}).$$

By integration under the boundary condition $\omega_1\omega_2 = z^2$ with $z = W_{\gamma\gamma}/2E$ the luminosity function for the photon beams

$$\frac{\mathrm{d}L_{\gamma\gamma}}{\mathrm{d}z} = \left(\frac{2\alpha_{\mathrm{em}}}{\pi}\right)^2 \frac{1}{z}\left(\ln\eta\right)^2 f(z) \tag{2.11}$$

with $\eta = \Theta_{\mathrm{max}}/\Theta_{\mathrm{min}}$ and the Low-function

$$f(z) = (2+z^2)^2 \ln\left(\frac{1}{z}\right) - (1-z^2)(3+z^2) \tag{2.12}$$

is obtained. The validity of this approximation has been widely discussed for different kinematic regions [5–8]. It is used in most of the calculations and estimations for two-photon physics and allows the interpretation of Eqn. (2.1) as photon-photon scattering processes.

2.3 Special Kinematic Situation

Most experiments use detectors measuring the two-photon processes that are not optimized for that purpose and which in addition suffer from acceptance problems in the very forward direction. Since the scattering angles of the beam leptons are

usually small, most of the beam leptons escape through the beam pipe without being detected. For that reason events are classified by the number of observed electrons, which are usually detected in the luminosity calorimeters since these are closest to the beam pipe and cover the smallest angles in the forward direction. For the detected leptons the four momentum transfer to the photon q_i can be calculated completely from the measured energy and angle with Eqn. (2.5). The measured electron is called the tag electron. Depending on the number of detected leptons no-tag, single-tag and double-tag events are distinguished. In double-tag events all quantities of the $\gamma\gamma$ system like $W_{\gamma\gamma}$ are known from the measured electrons and also the angle between the scattering planes of the beam leptons can be measured. Unfortunately the luminosity function for single- and double-tag events is about one or two orders of magnitude smaller than the luminosity function for no-tag events. Therefore measurements based on tagged events are limited by the available statistics.

In this analysis single tag events are used. That leads to somewhat simplified expressions in the cross section formula. The photon emitted by the undetected beam lepton can be treated as quasi real,

$$P^2 = -q_2^2 \approx 0. \tag{2.13}$$

Because of their P^2 dependence the terms σ_{TL}, σ_{LL} and τ_{TL} vanish [1]. Only the virtual photons emitted from the tagged lepton give significant contributions to the longitudinal component.

Since the angle $\tilde{\phi}$ cannot be measured, the measurement integrates over $\tilde{\phi}$ and is not sensitive to the term τ_{TT} although the term τ_{TT} itself does not vanish.

2.4 Structure Functions

For leptonic final states the remaining cross sections are defined within the framework of QED. In the case of hadronic final states it is not possible within perturbative QCD to calculate the full cross sections explicitly. It cannot be avoided to introduce parametrizations for the cross sections in the form of so called structure functions. For the reduced expression

$$\begin{aligned} \mathrm{d}^2\sigma \;=\; & \frac{\alpha_{\mathrm{em}}^2}{16\pi^4 Q^2 P^2}\left[\frac{(pq)^2 - Q^2P^2}{(p_1p_2)^2 - m_{\mathrm{e}}^2 m_{\mathrm{e}}^2}\right]^{\frac{1}{2}} \times \\ & \times 4\rho_1^{++}\rho_2^{++}\left[\sigma_{\mathrm{TT}} + \frac{\rho_1^{00}}{2\rho_1^{++}}\sigma_{\mathrm{LT}} + \frac{2|\rho_1^{+-}\rho_2^{+-}|}{\rho_1^{++}\rho_2^{++}}\tau_{\mathrm{TT}}\cos 2\tilde{\phi}\right] \times \\ & \times \frac{\mathrm{d}^3p_1'\mathrm{d}^3p_2'}{E_1'E_2'} \end{aligned}$$

structure functions $F^\gamma(x,Q^2)$ are defined in such a way, that the following equations are valid for the limit $P^2 \to 0$:

$$\begin{aligned} 2xF_{\mathrm{T}}^\gamma(x,Q^2) &= \left(\frac{Q^2}{4\pi^2\alpha}\right)\sigma_{\mathrm{TT}}(x,Q^2) \;=\; F_1^\gamma(x,Q^2) \\ F_2^\gamma(x,Q^2) &= \left(\frac{Q^2}{4\pi^2\alpha}\right)\left[\sigma_{\mathrm{TT}}(x,Q^2)+\sigma_{\mathrm{LT}}(x,Q^2)\right] \\ F_{\mathrm{L}}^\gamma(x,Q^2) &= \left(\frac{Q^2}{4\pi^2\alpha}\right)\sigma_{\mathrm{LT}}(x,Q^2) \\ F_x^\gamma(x,Q^2) &= \left(\frac{Q^2}{4\pi^2\alpha}\right)\tau_{\mathrm{TT}}(x,Q^2) \;=\; F_3^\gamma(x,Q^2) \end{aligned}$$

The structure function $F_x^\gamma(x,Q^2)$ is not accessible in our measurement but is not necessarily small. The differential cross section can now be written as

$$\frac{\mathrm{d}\sigma}{\mathrm{d}x\mathrm{d}Q^2} = \frac{2\pi\alpha^2}{xQ^4}\left((1-(1+y^2)^2)F_2^\gamma(x,Q^2) - y^2F_{\mathrm{L}}^\gamma(x,Q^2)\right].$$

Since in our kinematic region $y \ll 1$ holds, even $F_{\mathrm{L}}^\gamma(x,Q^2)$ can be neglected compared to $F_2^\gamma(x,Q^2)$ and

$$F_2^\gamma(x,Q^2) \sim \frac{\mathrm{d}\sigma}{\mathrm{d}x\mathrm{d}Q^2}\,. \tag{2.14}$$

The proportionality factor is given by the photon flux that can be calculated within EPA. Hence not only the dependence in Q^2 and x but also the absolute normalization of the structure function can be measured.

2.5 Physical Interpretation of the Structure Function

Another view on structure functions is possible in analogy to the interpretation of structure functions in deep inelastic electron-nucleon scattering. It can be related to the distribution of partons in a photon. The scattering process of a highly virtual photon from a tagged electron with a quasi real one is indeed very similar to the electron-nucleon scattering and is also known as electron-photon scattering. In Fig. 2.2 the two processes are schematically drawn.

The highly virtual photon whose Q^2 can be measured from the tagged electron has a spatial resolution according to the Heisenberg uncertainty principle of

$$\Delta x \approx \frac{1}{p_{\mathrm{T}}} \approx \frac{1}{\sqrt{Q^2}} \tag{2.15}$$

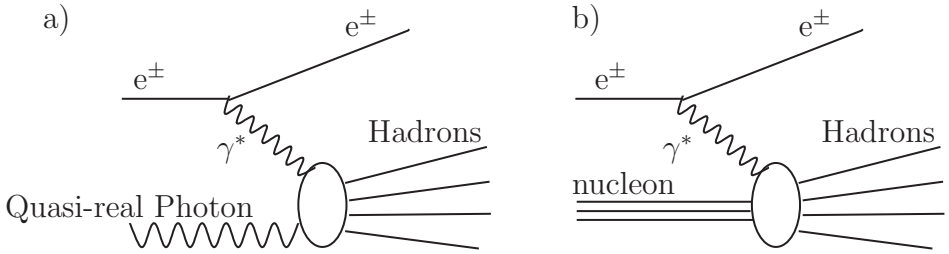

Figure 2.2: Two photon scattering (a) is very similar to deep inelastic electron-nucleon scattering (b) and can be treated with similar methods.

which is much smaller than the resolution of the quasi real photon ($P^2 \ll Q^2$). That being the case the highly virtual photon is called the "probing photon" and the quasi real one the "target photon".

For the structure of the photon three different contributions to the two-photon interaction are distinguished:

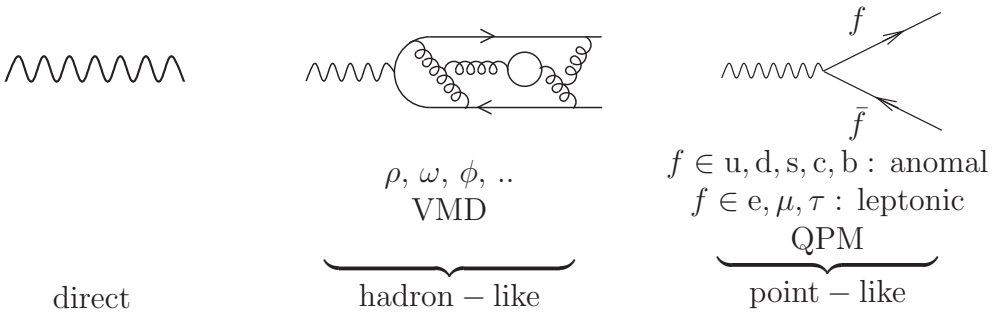

The weight of the different contributions depends on the virtuality Q^2 of the photon. For small Q^2 the photon fluctuates into a state with quantum numbers identical to the state of light vector mesons like ρ, ω, ϕ, ... The $q\bar{q}$ pair has a small transverse momentum p_{T} and thus stays in a bound state where the binding is due to gluon interactions between the quarks. These states of fluctuations cannot be calculated by perturbative QCD. A phenomenological approach for a description is given by the **V**ector-**M**eson **D**ominance model (VMD) [9–12]. The contribution to the photon structure is called the hadron-like component.

Photons with higher Q^2 fluctuate into $q\bar{q}$ pairs which have a higher transverse momentum p_{T} and so that the gluon interactions between these quarks are less important. The produced partons can be seen as essentially free and calculated within perturbative QCD. The structure is called point-like or QPM part according to the **Q**uark-**P**arton **M**odel that describes it. It is similar to the fluctuation into lepton pairs which is a pure QED process. In this thesis the lepton coupling

and the leptonic structure function are not discussed in detail. More on them can be found in the literature [13].

The photon wave function can now be written as a sum of different contributions like

$$|\gamma\rangle = \underbrace{c_{\mathrm{dir}}|\gamma_{\mathrm{dir}}\rangle}_{\text{direct}} + \underbrace{\sum_{V=\rho,\omega,\phi,\ldots} c_{\mathrm{V}}|V\rangle}_{\text{VMD}} + \underbrace{\sum_{q=\mathrm{u,d,s,c,b}} c_{\mathrm{q}}|q\bar{q}\rangle}_{\text{point-like}} + \underbrace{\sum_{l=\mathrm{e},\mu,\tau} c_{\mathrm{l}}|l\bar{l}\rangle}_{\text{leptonic}} . \tag{2.16}$$

The interpretation of the structure function $F_{2\,\mathrm{had}}^{\gamma}$ as the parton density is now obvious. The subscript "had" indicates that only the distributions of quarks and gluons are taken into account. In the following this subscript is suppressed. Now the hadronic structure function is

$$F_2^{\gamma}(x,Q^2) = x \sum_{i=\mathrm{u,d,s,\ldots,g}} e_i^2 f_i^{\gamma}(x,Q^2) \tag{2.17}$$

where $f_i^{\gamma}(x,Q^2)$ is the probability for finding a parton of type i with charge e_i and fraction x of the momentum of the photon; in leading order only the sum over the parton distributions has to be performed.

2.5.1 Hadron-like Structure, VMD

These distributions are not easily calculable. Their dynamics cannot be treated by a perturbative approach because of the low momentum transfer to the partons and the gluon exchange between them. Consequently phenomenological parametrizations with some theoretical model input have to be found. Again the VMD and the point-like part are treated separately. In the VMD part the structure function is approximated by the structure function of the pion, which is known from measurements of the Drell–Yan process $\pi^{\pm}N \to \mu^{+}\mu^{-}X$ [14–16]. In principle the structures of the lightest vector mesons are needed which are not known but assumed to be similar to the pion structure. An incoherent sum of the ρ and ω parts leads to the frequently used form obtained in [17, 18]

$$F_{2\,\mathrm{VMD}}^{\gamma}(x) = \frac{8}{9}\frac{4\pi\alpha_{\mathrm{em}}}{f_\rho^2} x q_i^{\rho}(x) = \alpha\,[0.2(1-x)] \tag{2.18}$$

with the ρ decay constant $f_\rho^2 = 2.2/4\pi$ as in [12]. One difficulty in the calculation of the VMD part is the scale dependence due to the Q^2 dependence of the gluon density that contributes to the x distribution. The differently motivated theoretical models vary in the reference scale Q_0^2 about which the Q^2 dependence

should be expanded [13]. Further models for a parametrization can be found in the literature, see for example Duke and Owens [19]:

$$F_{2,\,\mathrm{VMD}}^{\gamma} = \frac{4\pi\alpha}{f_\rho^2}\left[0.417\sqrt{x}(1-x) + 0.133(1-x)^5\right] \qquad \text{at } Q^2 = 3\,\mathrm{GeV}\,.$$

Their model has also been fitted to experimental data at low Q^2. The Collaboration TPC/2γ used

$$F_{2,\,\mathrm{had}}^{\gamma} = \alpha\left[(0.22 \pm 0.01)x^{0.31\pm0.02}(1-x)^{0.95} + (0.06 \pm 0.01)(1-x)^{2.5\pm1.1}\right]$$

for $0.3\,\mathrm{GeV} < Q^2 < 1.6\,\mathrm{GeV}$ [20]. The parametrization of the VMD part of the photon structure function is still a very active field of theoretical work.

2.5.2 Point-like Structure, QPM

Due to the Q^2 dependence of the vector meson propagator the point-like structure becomes more important with increasing virtuality of the photon. The different approaches for the treatment of the intermediate region between VMD model and point-like structure have to be tested by experiments and are one of the motivations for this work.

While the structure function of hadrons and as a consequence also the hadron-like motivated VMD part of the photon structure function decreases with increasing x, the point-like part becomes larger for higher values of x. This part which is similar to the QED structure is described by the Quark-Parton Model (QPM) and dominates the region of high transverse momenta and virtualities Q^2. The structure function of the QPM model is given by

$$F_{2,\,\mathrm{QPM}}^{\gamma}(x,Q^2) = N_c \sum_{k=1}^{n_f} \frac{e_{q_k}^4\,\alpha}{\pi} x \left\{\left[x^2 + (1-x)^2\right]\ln\frac{W^2}{m_{q_k}^2} - 1 + 8x(1-x)\right\} \quad (2.19)$$

with the numbers of color charges N_c and quark flavors n_f taken into account. For the detailed calculations see [21–23]. The logarithmic evolution with Q^2 incorporates the scale dependence of the structure function. This becomes more obvious for the substitution

$$\ln\left(\frac{W^2}{m_q^2}\right) = \ln\left(\frac{Q^2}{m_q^2}\right) + \ln\left(\frac{1-x}{x}\right) \quad (2.20)$$

that holds for $P^2 \ll Q^2$. In Fig. 2.3 both VMD and QPM part of the structure function are shown as a function of x for a fixed value Q^2. The very different behavior of both parts is clearly visible.

Because of this behavior it is assumed in the present measurement that the probing photon being highly virtual ($Q^2 \geq 10\,\mathrm{GeV}^2$) has a completely point-like structure. This ensures that it is really the hadronic structure of the quasi real photon which is measured.

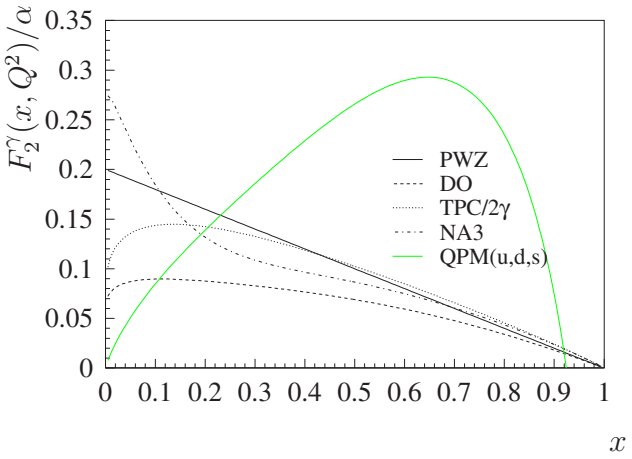

Figure 2.3: Different parametrizations of the photon structure function are plotted to show the different dependence on x for the VMD part and the QPM motivated contributions. The parametrizations of Peterson, Walsh and Zerwas (PWZ), Duke and Owens (DO) and the fits of the TPC/2γ and the NA3 collaborations exhibit the typical decrease of the VMD model. The QPM part is calculated for three quark flavors only at $Q^2 = 1\,\mathrm{GeV}^2$ and shows a characteristic rise towards larger values of x.

2.5.3 QCD Corrections

The quark parton model does not take into account any gluon coupling in leading order. This is too simplistic for a detailed analysis of the structure function although the basic dependence in Q^2 and x is described correctly. There are a lot of calculations of these higher order corrections. As shown in Fig. 2.4 the radiated gluons lead to a change in the four momentum of the quarks which then interact with the highly virtual probing photon. Other corrections have to be applied for the case that one of the radiated gluons produces another $q\bar{q}$ pair and one of this so called sea quarks interacts with the probing photon. The evolution of the parton density functions of the photon with respect to $\ln(Q^2)$ is described by the DGLAP equations (**D**okshitzer–**G**ribov–**L**ipatov–**A**ltarelli–**P**arisi) [24–28] [29]. Calculations based on these equations do not change the general shape of the structure function with Q^2: For the hadron-like part the function increases with Q^2 only for small x whereas it decreases for large x. The contribution of the point-like process increases for all x with Q^2. This scale dependence of the parton density functions leads to uncertainties and an arbitrariness in the choice of the reference scale Q_0^2. Widely used choices are of the order $1\,\mathrm{GeV}^2$.

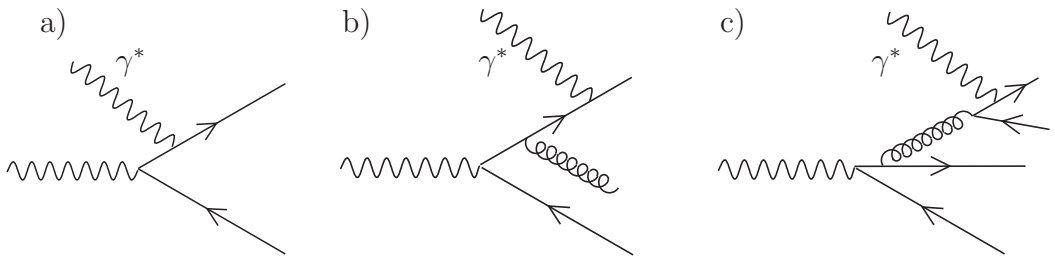

Figure 2.4: Examples where QCD corrections have to be applied: The virtual photon can interact directly with a quark from the fluctuation state like in leading order QPM calculations (a) or with a quark after it radiated a gluon (b). Even an interaction with a sea quark is possible as drawn in (c). Many more diagrams for QCD corrections are possible and have to be calculated.

2.6 Parametrizations of the Photon Structure Function

For the structure function of hadrons only the shape can be calculated. Initiated by the work of Witten [30] who first had the idea to separate point-like and hadron-like contributions, the calculation of the absolute normalization of the photon structure function for high Q^2 seemed to be possible. There is now aggreement that hadron-like contributions have to be included for high Q^2 point-like calculations to avoid singularities in higher order. A prediction of an absolute value for the structure function from QCD is not possible. More details and further references can be found in [31]. Some parametrizations will be presented here as examples of theoretical calculations. All of them start at a reference scale Q_0^2 and develop the Q^2 dependence by use of the DGLAP equations. Some different assumptions are made which are briefly mentioned. A rather complete overview on presently available work in that field can be found in [13]. The reason to choose these three parametrizations is the fact that they are quite different from the theoretical input point of view and that the results of this analysis are compared to these models later in this thesis. Given the limited precision of this measurement it is, however, hardly possible to discriminate between them. For that reason no attempt is made to fit parameters or give more quantitative comparisons. Most of the authors mentioned have actually published more than one set of parameters. All available parametrizations and references to the original publications can be found in the PDFLIB [59] and calculated with the functions provided there.

LAC [32] **L**evy, **A**bramowicz and **C**harchula used the same approach as was used in the DG (Drees,Grassie) parametrization that was published earlier [33]. Twelve parameters in the x dependent ansatz are fitted to data

while evolution equations at a fixed $\Lambda = 0.2\,\mathrm{GeV}$ are used to compute the contributions of four quark flavors and an ansatz for the gluon density function is made. In different available sets different starting scales Q_0^2 are used (LAC1, LAC2: $Q_0^2 = 4\,\mathrm{GeV}^2$; LAC3: $Q_0^2 = 1\,\mathrm{GeV}^2$) and, correspondingly, different gluon density functions: (LAC1: $xg(x) \sim x^b(1-x)^c$; LAC2: $xg(x) \sim (1-x)^c$; b, c are fitted to data). Contributions of the charm quark are taken into account only for $W^2 \geq (2m_\mathrm{c})^2$ with an assumed mass for the c quark of $m_\mathrm{c} = 1.5\,\mathrm{GeV}$. The improvement compared to the older DG parametrizations is due to the availability of larger data samples at higher Q^2 for the fit of the free parameters and the first attempt to fit the gluon density functions.

GRV **G**lück, **R**eya and **V**ogt base their calculations on the known structure function of the pion and those of other vector mesons originating from that and on the structure function of the proton [34–37] [16, 38, 39]. These structure function are available in leading (LO) and next-to-leading order (NLO). A starting scale of $Q_0^2 = 0.25\,\mathrm{GeV}$ is used for the LO calculations and $Q_0^2 = 0.3\,\mathrm{GeV}$ for NLO. The Q^2 evolution is treated by the DGLAP equation. Since the parton density function of the pion cannot be calculated in absolute normalization, a free parameter κ is introduced which has to be fitted to the data. At the starting scale a purely hadron-like state is assumed. The point-like part is dynamically developed for $Q^2 > Q_0^2$. For small values of W the heavy quarks ($m_\mathrm{c} = 1.5\,\mathrm{GeV}$, $m_\mathrm{b} = 4.5\,\mathrm{GeV}$) are introduced with the help of the Bethe–Heitler formula [40]. For high W they are also treated as massless.

SaS [41] **S**chuler **a**nd **S**jöstrand distinguish between hadron-like and point-like contributions in their ansatz. Another fundamental difference to all other parametrizations is the use of measured photon-proton cross sections for the input density functions. Various sets are available which all use $\Lambda = 0.2\,\mathrm{GeV}$ as the QCD scale parameter. The starting scale is $Q_0^2 = 0.36\,\mathrm{GeV}^2$ and $Q_0^2 = 4\,\mathrm{GeV}^2$ in sets SaS1 and SaS2. The light quarks are treated as massless, charm and bottom contributions are again introduced with the Bethe–Heitler formula ($m_\mathrm{c} = 1.3\,\mathrm{GeV}$, $m_\mathrm{b} = 4.6\,\mathrm{GeV}$). Special weight is put on the question how the VMD part of the photon in the parametrization depends on the start scale Q_0^2. SaS2 predicts a larger VMD part and as a result a stronger rise of the structure function at low x than SaS1 does. Furthermore both sets are computed in deep inelastic scattering scheme (DIS) as well as in the modified momentum subtraction scheme ($\overline{MS}$). Small differences appear in these methods. For small x the $\overline{MS}$ leads to slightly larger values but for $x \to 1$ it drops faster than the DIS calculations.

Chapter 3

Detector

The data used in this analysis is taken with the ALEPH detector at the e^+e^- storage ring LEP at CERN. Both the ALEPH detector as well as the LEP accelerator have been described in detail in various publications and a description is beyond the scope of this work. References [42–45] give a detailed picture of the experimental setup. In Fig. 3.1 a sketch of the detector is shown. It is built as a 4π–detector covering almost the complete solid angle around the interaction point.

Only detector parts which are used in this measurement are mentioned briefly. No description of the hardware itself but rather of its performance in terms of energy and momentum resolution etc. is given.

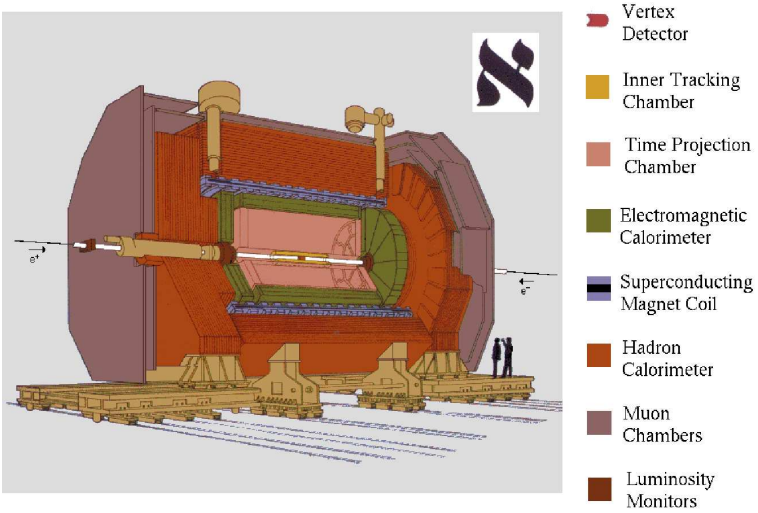

Figure 3.1: Drawing of the ALEPH detector, it shows the typical structure of a 4π–detector. The position of all important components can be seen.

Luminosity Calorimeter

At a distance of about 2.5 m on either side of the main interaction point the two luminosity calorimeters SiCAL (Silicon Calorimeter) and LCAL (Luminosity Calorimeter) are located around the beam pipe. Both are used to detect the scattered beam leptons. To obtain Q^2 a measurement of the energy E_{tag} and the scattering angle Θ_{tag} is needed (see Eqn. (2.5)). The angular acceptance of the luminosity calorimeters overlaps slightly: The inner detector, SiCAL, covers the range between 24 and 58 mrad but due to a tungsten shielding against backscattered synchrotron photons which was added in 1996 it is now sensitive only for angles larger than 34 mrad. LCAL which is located behind SiCAL extends the angular acceptance from 45 to 160 mrad. The angular resolution of SiCAL is 0.5 mrad, for LCAL it is about 1 mrad. The energy resolution for SiCAL is $\sigma_E/E = 0.34/\sqrt{E}$ and $\sigma_E/E = 0.15/\sqrt{E} \oplus 0.034$ for the LCAL detector respectively (E in GeV).

Tracking Devices

Particles produced at the main interaction point pass up to three different tracking devices. The innermost one is a two-layer silicon strip vertex detector (VDET), followed by a cylindrical drift chamber (ITC) and the central time projection chamber (TPC) as the main tracking device with a diameter of 3.6 m and a length of 4.4 m. Together with an axial magnetic field of 1.5 T provided by a superconducting solenoidal coil the transverse momentum of charged particles can be measured with a precision of $\Delta p_{\text{T}}/p_{\text{T}} = 0.005 \oplus 6 \times 10^{-4} p_{\text{T}}$ with p_{T} in GeV.

Calorimeter

Two different calorimeters are used to measure the energy of the final state particles. The inner one is the electromagnetic calorimeter (ECAL) that absorbs all photons and electrons. It has a certain granularity that allows a spatial resolution of $\sigma_\Theta/\sin\Theta = 0.32\,\text{mrad} \oplus 2.7\,\text{mrad}/\sqrt{E}$ and an energy resolution of $\sigma_E/E = 0.009 \oplus 0.18/\sqrt{E}$ with E in GeV. The energy and spatial resolution are a little different for the central barrel and the end caps. In the overlap region and at the edges of the end caps, the resolution can be worse by up to 30%.

The hadron calorimeter (HCAL) is located outside the magnetic coil and is also used as the iron return yoke for the magnetic field. The energy resolution for charged and neutral hadrons is $0.84/\sqrt{E}$. While hadrons are absorbed in the HCAL, muons with momentum larger than 2.4 GeV can pass through HCAL and are identified in the muon chambers that form the outer layer of ALEPH.

Trigger

The trigger system of ALEPH is designed in three levels to select interesting data by a fast reduction of background events to keep the amount of data that has to be stored as small as possible without loosing "good" events. The first-level trigger is a hardware trigger using ITC and calorimeter information. If the first-level trigger decision is positive, the TPC is read out and some track requirements are checked in the next level. A positive level-two decision leads to a read out of the whole detector. Level three is a pure software trigger using information from a simplified event reconstruction.

Since ALEPH has no explicit $\gamma\gamma$ trigger condition, it is hard to give a value for the trigger efficiency. There are no two different independent triggers available for this kind of events. From various studies it is understood that the trigger efficiency for events with hadronic masses and a total transverse momentum as selected for this analysis is close to 100%, slightly depending on x [46]. In the low x region it should be safe to assume a 100% efficiency. For higher x it is estimated to be $\geq$ 95%. Since no exact number can be found, the analysis is done under the assumption of a fully efficient detector. In the region, where a slightly lower efficiency is possible, the statistical and systematic uncertainties of the analysis are large, so that the trigger uncertainty would not increase the errors significantly.

Energy-Flow Objects

During the event reconstruction the energy-flow algorithm is applied to form a set of disjoint particles. Information from energy measurements in the calorimeters are combined with momentum measurements from the curvature of the tracks which can be associated with energy depositions in the direction of the tracks. Since energy measurement and momentum measurement of the same charged particle is redundant, the energy-flow object is formed from the quantity that provides the best accuracy which usually is the momentum measurement. For all tracks some quality requirements have to be passed like a minimum number of four hits in TPC, distance from main vertex etc.. Energy depositions that cannot be associated with tracks or exceed the expected energy deposition for the associated track by a certain amount are treated as stemming from neutral particles. Electrons are identified by their shower profile in the calorimeters for momenta larger than 1.5 GeV and muons are identified by hits in the muon chambers for momenta larger than 2.4 GeV, respectively. For more details of the energy-flow algorithm see [43].

Chapter 4

Detector Resolution and Unfolding

4.1 Detector Resolution

As in all particle physics experiments the measured quantity is affected by detector effects like limited resolution and acceptance. Since only the "true" value as produced by the investigated physics process is of interest, a correction for these detector influences is necessary. This is especially important for a comparison between different experiments and with theories. The process of correcting for these effects is called "unfolding".

In this analysis the differential cross section $\mathrm{d}\sigma/\mathrm{d}x$ has to be measured. It is directly obtained from the number of reconstructed events N in each x bin, $\mathrm{d}N/\mathrm{d}x$, and the luminosity. The Bjorken variable x is defined as

$$x = \frac{Q^2}{Q^2 + W^2} \qquad (P^2 \approx 0)$$

in chapter 1. Both variables Q^2 as well as W^2 are measured with large uncertainties.

The measurement error in Q^2 originates in the limited energy resolution of the luminosity calorimeters. In Fig. 4.1 the observed quantity Q^2_{vis} is plotted versus the true value Q^2_{true} as given by the Monte Carlo simulation. Although the mean value of the seen distribution is close to the true value as shown in Fig. 4.2, the measured values are smeared out significantly around the central value. Especially for small Q^2 this effect is important because the relative error in Q^2 is energy dependent and improves for high Q^2.

The measurement of the invariant mass of the hadronic final state W^2 does not suffer too much from the uncertainty in the measured track quantities. The main

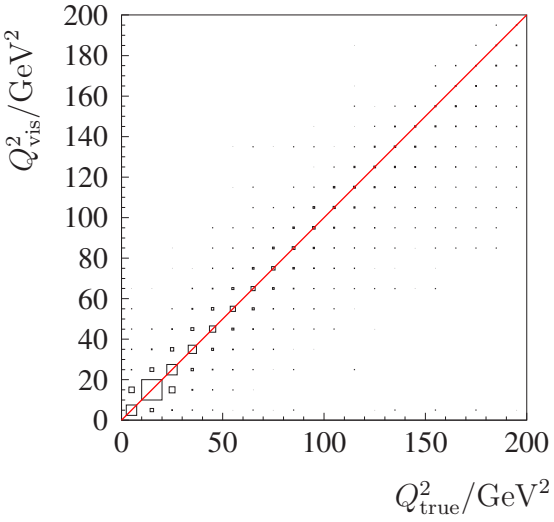

Figure 4.1: Detector resolution for the virtualities of the tagged photons. The reconstructed quantities $Q^2_{\rm vis}$ are plotted versus the generated values $Q^2_{\rm true}$.

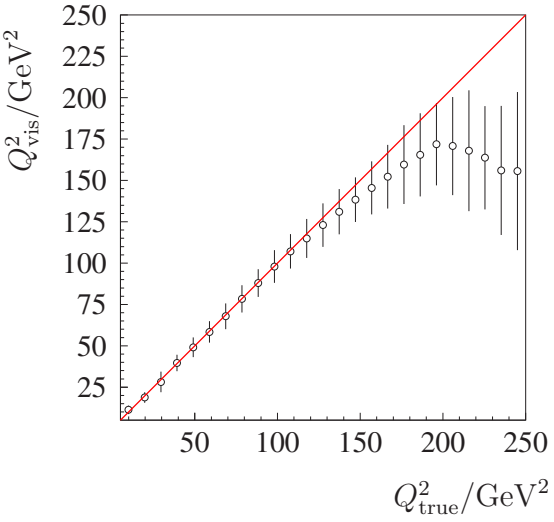

Figure 4.2: Same quantities plotted as in Fig. 4.1 but as central reconstructed values plus error bars giving the smearing of the detector.

effect here comes from particles lost due to acceptance problems in the forward direction of the detector. The two photons colliding differ very much in energy and momentum, especially in the case of single-tag events. For that reason the $\gamma\gamma$ centre-of-mass system is not identical with the laboratory system in which the detector is at rest. This leads to a strong Lorentz boost of the hadronic system that increases with the beam energy. Unfortunately the precision and acceptance of ALEPH is less good around the beam pipe in the forward direction which is of importance for boosted events. Final state hadrons produced in forward direction are the main reason for a large uncertainty in the measured quantity $W_{\gamma\gamma}$. The diagram in Fig. 4.3 shows the ϑ distribution of the particles in the hadronic system. No tracks are reconstructed below $\vartheta \approx 0.03\,\text{rad}$. In Fig. 4.4 the distribution of the polar angle Θ of the scattered beam lepton as generated in the Monte Carlo and as seen after full detector simulation is shown. Fig. 4.5 shows $W_{\rm vis}$ plotted versus $W_{\rm true}$. Unlike for the measurement of Q^2 the $W_{\rm vis}$ distribution is not smeared out symmetrically but tends to show $W_{\rm vis} < W_{\rm true}$. The resolution of the Bjorken variable x is finally shown in Fig. 4.6.

For the measured x spectrum these resolution and acceptance effects have several consequences in different regions:

- For low Q^2 the measurement suffers a lot from the poor energy resolution for the tagged electron.
- At low x the spectrum is dominated by low Q^2 events.

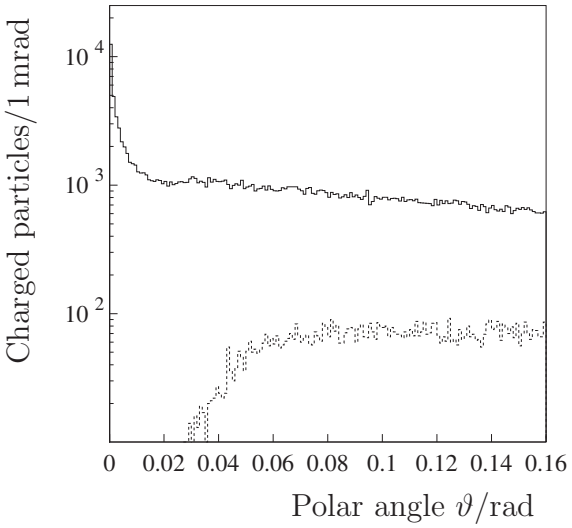

Figure 4.3: The diagram shows the ϑ distribution of the charged particles in the hadronic system. The solid line represents the true distribution as produced by the HERWIG Monte Carlo generator. The dashed line gives the distribution for the reconstructed particles.

- The W^2 measurement tends to pull events towards higher x.
- Events generated with a large W^2 of the hadronic system, usually at lower x, lose some tracks and are then observed at higher x, but the detection efficiency for these events is quite good. In contrast events with a small W are frequently lost completely. Therefore the x spectrum suffers more from inefficiencies at large values of x, where the Q^2 measurement is better.

Already from these considerations large uncertainties in the measurement at the edges of the experimentally accessible x spectrum are expected.

4.2 Detector-Response Matrix

The influence of the detector can be described by a detector-response matrix [47]. Let the true distribution follow a normalized probability density function $f_{\text{true}}(y)$. Then the probability of an event being produced in bin j of the x spectrum is given by

$$p_j = \int_{\text{Bin}\,j} f_{\text{true}}(y)\mathrm{d}y.$$

After the measurement one is interested in the probability of finding the event in bin i. If the conditional probability for measuring an event produced with y at a value x is given by $s(x|y)$ and the probability of seeing the event is given by the efficiency $\epsilon(y)$, then the probability for the migration of an event from bin j into bin i is given by

$$p_{ij} = \int_{\text{Bin}\,i} \{ \int_{\text{Bin}\,j} s(x|y)\epsilon(y) f_{\text{true}}(y)\mathrm{d}y \}\mathrm{d}x.$$

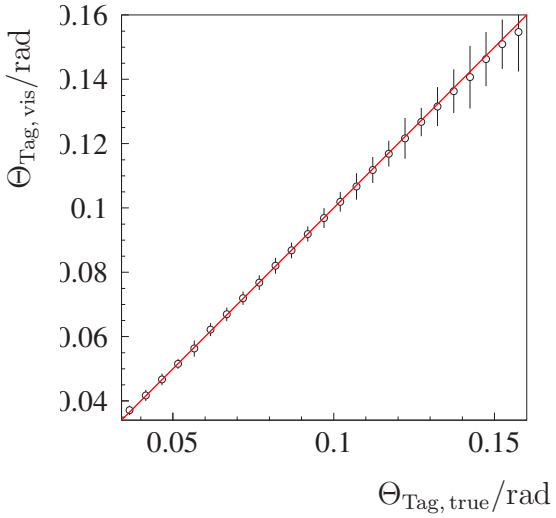

Figure 4.4: The precision of the measurement of the scattering angle of the tagged beam lepton can be judged from this diagram where $\Theta_{\mathrm{Tag,\,vis}}$ is plotted versus $\Theta_{\mathrm{Tag,\,true}}$.

The response function

$$r(x|y) \equiv s(x|y)\epsilon(y)$$

contains all experimental effects.
The expectation value for the measured number of events in bin i is then

$$E(x_{\mathrm{vis},i}) = \sum_{j=1}^{M} p_{ij} \cdot x_{\mathrm{true},j}. \tag{4.1}$$

where $x_{\mathrm{true},j}$ is the number of events generated in bin j. The expectation value $E(x_{\mathrm{vis},i})$ is identified with the observed number of events in bin i, $x_{\mathrm{vis},i}$, as the best available estimate.

Writing the true and visible spectra as vectors[1] $\mathbf{x}_{\mathrm{true}}$ and $\mathbf{x}_{\mathrm{vis}}$ giving the number of events in bin i as the ith component of the vector, Eqn. (4.1) defines a matrix equation

$$\mathbf{x}_{\mathrm{vis}} = A\mathbf{x}_{\mathrm{true}} \tag{4.2}$$

with a detector-response matrix A and

$$A_{ij} = p_{ij}$$

which is surely not independent of the probability density function $f_{\mathrm{true}}(y)$ of the true quantity. The matrix becomes independent of this if the bins are chosen in such a way that the response function $r(x|y)$ is almost constant over the whole

[1]Vector quantities are set in bold letters, for example $\mathbf{x}$. Their components are written in italic letters with subscript, x_i. Italic letters without a number subscript denote the norm of the vector, $x = ||\mathbf{x}||$.

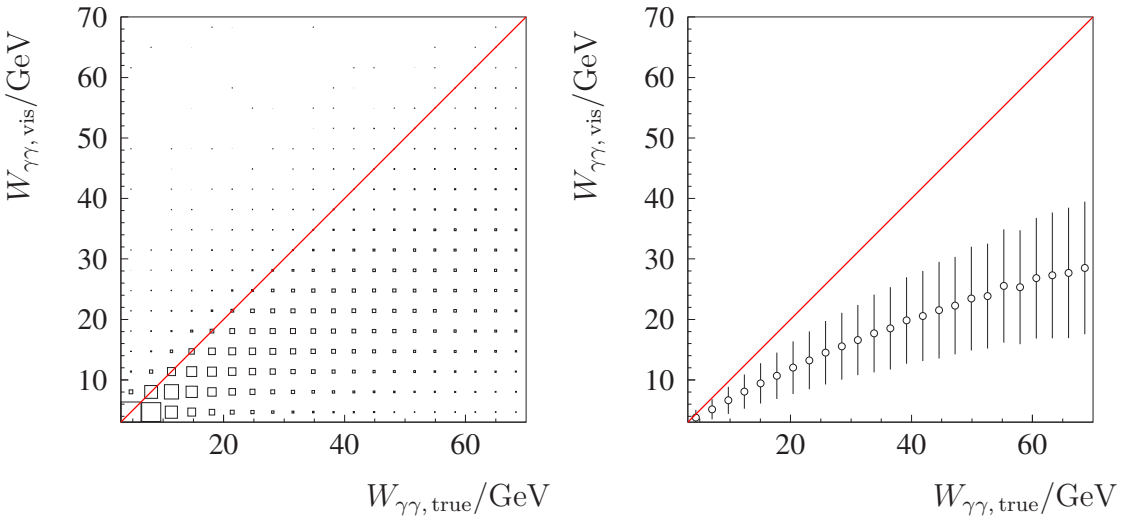

Figure 4.5: Resolution of the invariant hadronic mass $W_{\gamma\gamma}$.

bin. Then the integrals separate and the sum over all bins of the true distribution always adds up to unity since the probability density function $f_{\mathrm{true}}(y)$ was assumed to be normalized.

If additional background processes are present in the experiment, they can be included in Eqn. (4.2) by an additional vector $\mathbf{b}$:

$$\mathbf{x}_{\mathrm{vis}} = A\mathbf{x}_{\mathrm{true}} + \mathbf{b} \tag{4.3}$$

If the background is well understood it can be subtracted as is done in this analysis. In the following $\mathbf{x}_{\mathrm{vis}}$ is usually understood as the background subtracted visible spectrum so that Eqn. (4.2) can be used.

Throughout the explanation of the unfolding method in this chapter and the calculations in the appendix, a superscript δ, for example $\mathbf{v}^\delta$ or M^δ, indicates that the quantity is not known exactly but has an error. The vector $\delta\mathbf{v}$ and the matrix δM then consist of the uncertainties of the components of the vector or the matrix.

$$\mathbf{v}^\delta = \mathbf{v} \pm \delta\mathbf{v} = \begin{pmatrix} v_1 \\ \vdots \\ v_n \end{pmatrix} \pm \begin{pmatrix} \sigma_1 \\ \vdots \\ \sigma_n \end{pmatrix}, \qquad M^\delta = M \pm \delta M = (m_{ij}) \pm (\sigma_{ij})$$

The vector $\boldsymbol{\delta}$ always stands for the uncertainties in the measured quantity.

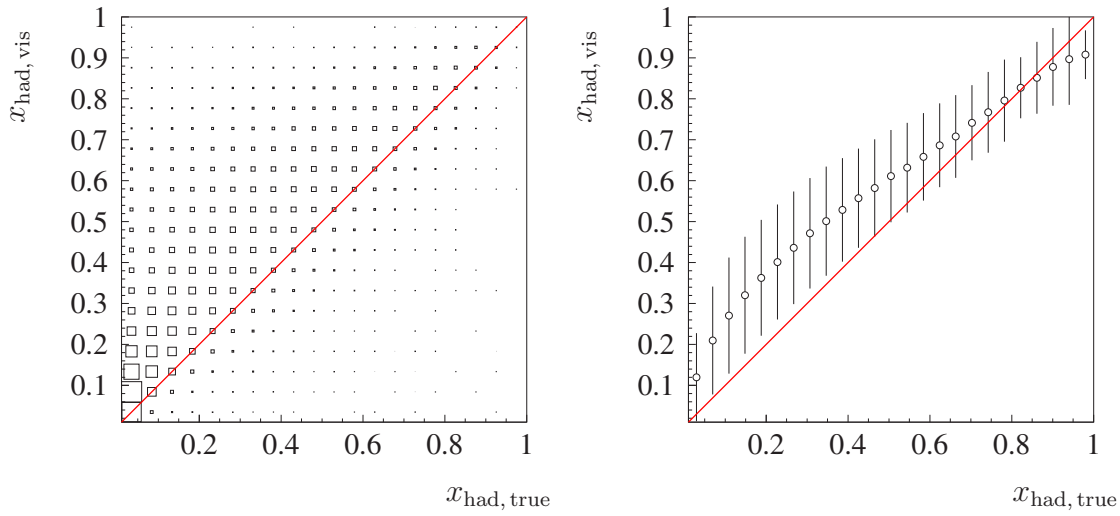

Figure 4.6: Resolution of the Bjorken variable x_{had}. Both, the uncertainties in the measurement of Q^2 and $W_{\gamma\gamma}$ contribute to the distortion of the x spectrum.

4.3 Ill-Conditioned Systems

Since one is interested in $\mathbf{x}_{\mathrm{true}}$ rather than in the measured histogram $\mathbf{x}_{\mathrm{vis}}$ Eqn. (4.2) has to be inverted. Unfortunately Eqn. (4.2) represents what is known as an ill-conditioned system. To explain the impact on the unfolding process we use a Monte Carlo sample for which the true distribution is well known. The simplest ansatz one could think of would be to invert Eqn. (4.2) and obtain

$$\mathbf{x}_{\mathrm{unf}} = A^{-1}\mathbf{x}_{\mathrm{vis}}. \tag{4.4}$$

If the matrix A is singular one would use the pseudo-inverse matrix $A^{\dagger}$ instead of the exact inverse matrix A^{-1}. In the present case there is no numerical or other problem so that the inverse matrix A^{-1} is always available. The results, however, are not satisfactory as is shown in Fig. 4.7. Of course, for a sample built from the full available Monte Carlo statistics that is used to build the matrix A, Eqns. (4.2) and (4.4) hold and $\mathbf{x}_{\mathrm{unf}} = \mathbf{x}_{\mathrm{true}}$. The measured data sample as well as a smaller Monte Carlo test sample is always influenced by measurement errors which cannot be avoided simply because of statistical fluctuations in the number of observed events which is Poisson distributed. This would be different for infinite statistics which is, of course, never available. For a well-conditioned problem one would now demand a continuous dependence of the unfolded spectrum on the uncertainties and small fluctuations in the visible distribution such that small fluctuations in the measurement only lead to small differences between the unfolded spectrum and the true spectrum. That the dependence is continuous is ensured by the

linearity of Eqn. (4.2). The size of the uncertainties in the unfolded spectrum can be calculated by error propagation. The covariance matrix $C_{x,\,\mathrm{vis}}$ is given by a diagonal matrix with elements

$$C_{\mathrm{vis},ii} = \sqrt{x_{\mathrm{vis},i}} \tag{4.5}$$

containing the statistical error of the number of events observed in bin i. The covariance matrix $C_{x,\,\mathrm{unf}}$ for the unfolded spectrum is calculated in appendix A, Eqn. (A.2). One has to be aware of the fact that Eqn. (A.2) only holds for Gaussian-distributed quantities. It can be applied here because the binning is chosen such that the number of observed events in every bin is large enough (> 100) and that therefore the Poisson distribution does not differ too much from the Gaussian. Because of the migration between different bins contained in the matrix A, the values in $\mathbf{x}_{\mathrm{true}}$ are now highly correlated and the correlation coefficients can be found in the off-diagonal elements of the matrix $C_{x,\,\mathrm{unf}}$.

It can be seen in Fig. 4.7 that the uncertainty in the unfolded spectrum is not small at all although the relative statistical errors in the visible distribution are on a 5% level as plotted in Fig. 4.8. A system with such behavior is called ill-conditioned.

To give a more quantitative approach to the phenomenon the condition number of a matrix M is defined through:

$$\mathrm{cond}(M) := ||M||||M^{-1}||$$

with a norm $||.||$. For a detailed and mathematical precise definition one of the many available textbooks should be used. The introduction given here mainly bases on the discussion in [48] and the very detailed work in [49]. Although the subject is developed in a much larger context, it is needed here only for real square matrices A with the Euclidean norm $||.||$ defined as

$$\begin{aligned} ||\mathbf{x}|| &= \sqrt{\sum_{i=1}^{N} x_i^2} \quad \text{for vectors and} \\ ||M|| &= \sqrt{\rho(M^{\mathrm{T}}M)} \leq \sqrt{\sum_{i,j=1}^{N} |m_{ij}|^2} \quad \text{for matrices} \end{aligned}$$

with the spectral radius of a matrix M

$$\rho(M) := \max\left\{|\lambda| : \lambda \text{ eigenvalues of } M\right\}.$$

For real square matrices A, the matrix $H = A^{\mathrm{T}}A$ is a Hermitian matrix and the eigenvalues of H are real, too. The condition of the matrix H is then

$$\mathrm{cond}(H) = \frac{|\lambda_{\max}|}{|\lambda_{\min}|}, \quad \lambda_{\min} \neq 0 \tag{4.6}$$

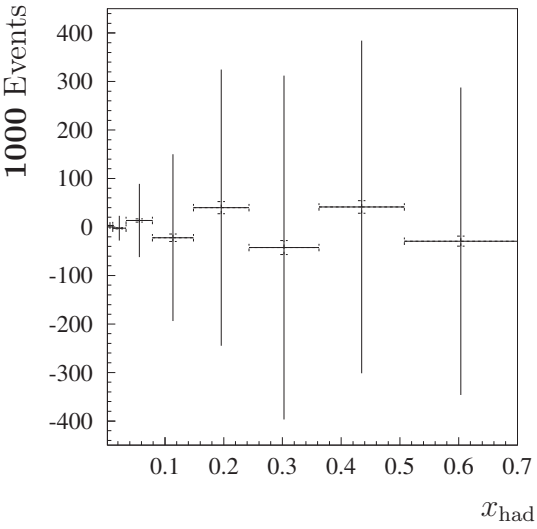

Figure 4.7: Unfolded x spectrum without regularization. The inner error bars indicate the uncertainty that originates from the limited data statistics. The outer error bars also contain the uncertainties δA due to limited Monte Carlo statistics. Both errors are added up in quadrature.

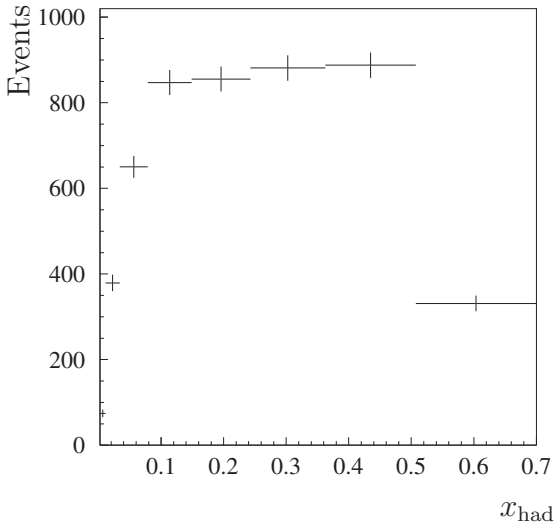

Figure 4.8: Visible x spectrum that leads to Fig. 4.7 by unregularized unfolding. Error bars are drawn for the statistical errors only.

with $\lambda_{\max}$ and $\lambda_{\min}$ being the eigenvalues with largest and smallest modulus.

The condition number now yields a quantitative measure for the ill-conditionedness or the instability of the linear system in Eqn. (4.2). Let $\mathbf{x}_{\mathrm{vis}}^{\delta}$ be the measured distribution with the uncertainties given by a vector $\boldsymbol{\delta}$ with $\delta = ||\boldsymbol{\delta}||$. $\mathbf{x}_{\mathrm{vis}}^{\delta=0} = \mathbf{x}_{\mathrm{vis}}$ would be the visible histogram for a measurement with infinite statistics. Since even A is not given with arbitrary high precision A^{δ} is introduced:

$$A^{\delta} = A + \delta A$$

Here the error of the matrix A, δA, is given by the statistical uncertainty of the matrix elements because of a limited number of available Monte Carlo events. For the difference between the unfolded result $\mathbf{x}_{\mathrm{unf}} = A^{-1}\mathbf{x}_{\mathrm{vis}}^{\delta}$ and $\mathbf{x}_{\mathrm{true}}$ it can be found that

$$\frac{||\mathbf{x}_{\mathrm{unf}} - \mathbf{x}_{\mathrm{true}}||}{||\mathbf{x}_{\mathrm{true}}||} \leq \frac{\mathrm{cond}(A)}{1 - \mathrm{cond}(A)\frac{||A^{\delta}-A||}{||A||}} \left\{ \frac{||\mathbf{x}_{\mathrm{vis}}^{\delta} - \mathbf{x}_{\mathrm{vis}}^{\delta=0}||}{||\mathbf{x}_{\mathrm{vis}}^{\delta=0}||} + \frac{||A^{\delta} - A||}{||A||} \right\}.$$

The error of the matrix A can be made small by using a larger Monte Carlo sample. The Monte Carlo sample used in this analysis is sufficient to keep the influence of the matrix error small compared to the error introduced by the statistically limited data sample for the regularized result that is introduced later in this chapter. For the unregularized unfolding described so far, the matrix uncertainty δA actually dominates the error in the unfolded spectrum. The full error propagation including the effects of δA is given in appendix A. In Fig. 4.9 the contribution of δA to the total statistical error can be seen. A problem arises from the fact, that the detector-response matrix is as well affected by systematic uncertainties, since it is almost singular. The relative error of small elements cannot be made arbitrarily small by larger Monte Carlo samples and they would still suffer from uncertainties in the detector simulation. But these small matrix elements are extremely important for the matrix inversion.

The most stable linear system from this point of view is given by the identity matrix I with $\mathrm{cond}(I) = 1$. The stability decreases with increasing condition number. Typical condition numbers for the detector-response matrices A are of the order

$$\mathrm{cond}(A^T A) \approx 10^6$$

which is surely ill-conditioned. Because of the Hermitian nature of $A^{\mathrm{T}}A$ the equivalent equation

$$A^{\mathrm{T}} A \mathbf{x}_{\mathrm{true}} = A^{\mathrm{T}} \mathbf{x}_{\mathrm{vis}}$$

is used instead of Eqn. (4.2) in the following.

It has to be stressed that the ill-conditionedness of the matrix A is a consequence of the imperfectness of the detector for the measurement of physics processes as they are investigated here. The problem cannot be solved by a better Monte Carlo simulation since that would alone improve the precision of the matrix but not its condition. There are only two possible solutions to improve the relative error $||\mathbf{x}_{\mathrm{unf}} - \mathbf{x}_{\mathrm{true}}||/||\mathbf{x}_{\mathrm{true}}||$:

1. $\delta \to 0$, that means a more precise measurement of the visible data.

2. Manipulation of A to improve the condition and the effects of matrix uncertainties artificially.

The first approach is simply not possible since LEP and ALEPH are dismantled. Even for a completely new experimental setup there are limitations: Necessarily near the beam there is a space free of detectors. Here particles pass undetected. The second way seems to be dangerous because a manipulation of the detector-response matrix is equivalent to changing the detector and it is certainly difficult to overcome hardware problems by purely mathematical techniques. But it comes out, that this manipulation can be handled in terms of uncertainties in a well

defined way. This method is called a regularized unfolding and has proven its potential in many applications.

4.4 Tikhonov Regularization

For each real $m \times n$, $m \geq n$, matrix A the square $n \times n$ matrix $H = A^{\mathrm{T}}A$ is Hermitian and positive semidefinite. The square roots of the eigenvalues of H, which are always real and nonnegative, are called the singular values of H. In general the rank r of the matrix A can be less then n. In this analysis the detector-response matrix A is always a real square matrix and the inverse matrix A^{-1} exists. Furthermore there are no singular matrices within the range $A \pm \delta A$. This is particularly important for the calculations of the uncertainties in the appendix A since otherwise the linear expansion of the Matrix A^{-1} would not be appropriate. In cases where the matrix A is not a square matrix but $A^{\mathrm{T}}A$ is not singular, the equation

$$A'\mathbf{x}_{\mathrm{true}} = \mathbf{x}'_{\mathrm{vis}}$$

with

$$A' = A^{\mathrm{T}}A \text{ and } \mathbf{x}'_{\mathrm{vis}} = A^{\mathrm{T}}\mathbf{x}_{\mathrm{vis}}$$

can be considered instead of the original Eqn.(4.3). It is conceivable that a treatment in analogy to the calculation described in appendix A can be carried out for singular matrices by a substitution of A^{-1} with the pseudo-inverse matrix $A^{\dagger}$. But this has not been checked. For the treatment of singular matrices see also [49].

It is possible to find two unitary matrices $U = (\mathbf{u}_1, ..., \mathbf{u}_n)$ $(n \times n)$ and $V = (\mathbf{v}_1, ..., \mathbf{v}_m)$ $(m \times m)$ so that the matrix A can be written as

$$A = V\Sigma U^* \tag{4.7}$$

where Σ is a $m \times n$ diagonal matrix with the singular values $\mu_1, .., \mu_n$ as its diagonal elements Σ_{ii}. $\mathbf{u}_1, ..., \mathbf{u}_n$ and $\mathbf{v}_1, ..., \mathbf{v}_m$ are the column vectors of U and V. For practical reasons the singular values are ordered such that $\mu_1 \geq \mu_2 \geq ... \geq \mu_r > \mu_{r+1} = ... = \mu_n = 0$. This is known as a singular values decomposition of the matrix A. It is easy to see that

$$A\mathbf{x} = \sum_{j=1}^{r} \mu_j(\mathbf{x}, \mathbf{u}_j)\mathbf{v}_j$$

with $(.,.)$ denoting the Euclidean scalar product. On the other hand for the equation

$$A\mathbf{x} = \mathbf{y} \tag{4.8}$$

the solution is given by

$$\mathbf{x} = \sum_{j=1}^{r} \frac{1}{\mu_j}(\mathbf{y}, \mathbf{v}_j)\mathbf{u}_j. \tag{4.9}$$

For $r = n$ this is the exact solution $\mathbf{x} = A^{-1}\mathbf{y}$. Otherwise Eqn. (4.9) is the solution

$$\mathbf{x} = A^{\dagger}\mathbf{y}$$

with $A^{\dagger}$ being the pseudo inverse or Moore–Penrose inverse of the matrix A. The solution $\mathbf{x}$ is the least square solution of Eqn. (4.8) with smallest norm [50].

With the knowledge of the relation between singular values and the condition of a matrix given in Eqn. (4.6) one can now see the consequence of small singular values on the solution $\mathbf{x}$. For some δ we disturb the right hand side of Eqn. (4.8) by replacing $\mathbf{y}$ by $\mathbf{y}^{\delta} = \mathbf{y}+\delta\mathbf{v}_j$. The obtained solution for $\mathbf{x}^{\delta}$ is then $\mathbf{x}^{\delta} = \mathbf{x}+\delta\mathbf{u}_j/\mu_j$. The ratio $||\mathbf{x}^{\delta} - \mathbf{x}||/||\mathbf{y}^{\delta} - \mathbf{y}|| = 1/\mu_j$ becomes large if the singular values μ_j are small.

This observation motivates in a straight-forward manner the idea of a regularized unfolding as it was introduced by Phillips in 1962 [51] and independently by Tikhonov 1963 [52,53]. In Eqn. (4.9) the contributions of small singular values are damped by a weighting factor

$$\frac{\mu_j^2}{\alpha + \mu_j^2}$$

where α is a positive parameter called regularization parameter. For $\alpha = 0$ the system remains unchanged. For $\alpha > 0$ the influence of small singular values decreases with increasing α. One can show that

$$\mathbf{x}_{\alpha} = \sum_{j=1}^{r} \frac{\mu_j}{\alpha + \mu_j^2}(\mathbf{y}, \mathbf{v}_j)\mathbf{u}_j \tag{4.10}$$

solves the equation

$$(\alpha I + A^{\mathrm{T}}A)\mathbf{x}_{\alpha} = A^{\mathrm{T}}\mathbf{y} \tag{4.11}$$

uniquely and that for $\alpha \to 0$ the regularized solution $\mathbf{x}_{\alpha}$ converges towards the exact solution given in Eqn. (4.9). Furthermore one finds that

$$||A\mathbf{x}_{\alpha} - \mathbf{y}||^2 + \alpha||\mathbf{x}_{\alpha}||^2 = \inf_{\mathbf{x}\in\mathbb{R}^n} \left\{||A\mathbf{x} - \mathbf{y}||^2 + \alpha||\mathbf{x}||^2\right\}.$$

This gives an interpretation of the Tikhonov regularization method: The residual $||A\mathbf{x}_{\alpha} - \mathbf{y}||^2$ is kept small to stay close to the original system. The penalty term $\alpha||\mathbf{x}_{\alpha}||^2$ prevents $\mathbf{x}_{\alpha}$ from becoming too large.

4.4.1 Approximation Error

The condition of the matrix $(\alpha I - A^{\mathrm{T}}A)$ is

$$\mathrm{cond}(\alpha I - A^{\mathrm{T}}A) = \frac{\alpha + \mu_1^2}{\alpha + \mu_n^2} \leq \frac{2\mu_1^2}{\alpha}, \quad 0 < \alpha \leq \mu_1^2.$$

It is obvious that a large regularization parameter α supports a better stability. On the other hand clearly a small parameter α keeps the changes to the system reasonably small.

These changes have to be looked at a little closer. For an erroneous $\mathbf{y}^\delta$ with $||\mathbf{y}^\delta - \mathbf{y}|| \leq \delta$ the vector $\mathbf{x}_\alpha$ solves the equation

$$(\alpha I + A^{\mathrm{T}}A)\mathbf{x}_\alpha = A^{\mathrm{T}}\mathbf{y}^\delta.$$

The estimate

$$||\mathbf{x}_\alpha - \mathbf{x}|| \leq ||(\alpha I + A^{\mathrm{T}}A)^{-1}A^{\mathrm{T}}||\delta + ||(\alpha I + A^{\mathrm{T}}A)^{-1}A^{\mathrm{T}}\mathbf{y} - A^\dagger \mathbf{y}||$$

divides the total error into two terms where one term only depends on the error level δ and the calculation of the second term requires a knowledge of the exact right hand side. Going back to the measurement, the erroneous $\mathbf{y}^\delta$ are accessible data, given by the visible distribution $\mathbf{x}_{\mathrm{vis}}$. Accordingly the first term is called the data error $E_{\mathrm{data}} = ||\mathbf{E}_{\mathrm{data}}||$. It can even be given bin-by-bin by normal error propagation. This calculation is performed for the statistical error of the final results. The second part of the error estimation is not accessible from data. Consequently the approximation error

$$\mathbf{E}_{\mathrm{approx}} = (\alpha I + A^{\mathrm{T}}A)^{-1}A^{\mathrm{T}}\mathbf{y} - A^\dagger \mathbf{y}$$

can only be estimated to a certain extent. Here it is done with some reference distribution $\mathbf{x}_{\mathrm{vis}}^{\delta=0}$ from Monte Carlo models (GRV and SaS) which describe the data well in various event shape variables. Therefore it is expected to be not too far away from the "true" $\mathbf{y}$. To avoid the relative approximation error fluctuating artificially between two neighboring bins, the mean of the calculated $\mathbf{E}_{\mathrm{approx}}$ value for the bin itself and its two neighbors is assigned to each bin. It must be stressed, that in regions where the approximation error becomes large, no local information can be taken from the unfolded distribution.

The two components of the total error $\mathbf{E}_{\mathrm{data}}$ and $\mathbf{E}_{\mathrm{approx}}$ show completely different behavior in their dependence on the regularization parameter α. While for $\alpha \to 0$ the data error becomes large as in the unregularized unfolding, for $\alpha > 0$ the estimate

$$\begin{aligned} E_{\mathrm{data}} &= \sqrt{\sum_i C^2_{x,ii}(\boldsymbol{\delta}, \alpha)} \\ &\approx ||(\alpha I + A^{\mathrm{T}}A)^{-1}A^{\mathrm{T}}||\delta \geq \frac{\mu_r}{\alpha + \mu_r^2}\delta \end{aligned}$$

holds. The statistical error can be made arbitrarily small by a large regularization parameter α. The approximation uncertainty is the expense for that improvement. While $\mathbf{E}_{\text{approx}}$ goes to zero for $\alpha \to 0$ it increases with increasing α.

A remark has to be made concerning the uncertainty introduced by the matrix A itself which is not known with arbitrary accuracy. As shown in appendix A the error $\mathbf{E}_{\delta A}$ depends on the regularization parameter and can be included into the statistical uncertainty $\mathbf{E}_{\text{data}}$. In Fig. 4.9 all three contributions E_{data} (excl. $E_{\delta A}$), $E_{\delta A}$ and E_{approx} are plotted separately together with the total error E_{tot} which is the sum of all three added up in quadrature. It is important, that the uncertainty $E_{\delta A}$ is shrinking with increasing α. The diagram in Fig. 4.9 is produced using real ALEPH data taken between $\sqrt{s} = 205\,\text{GeV}$ and $207\,\text{GeV}$.

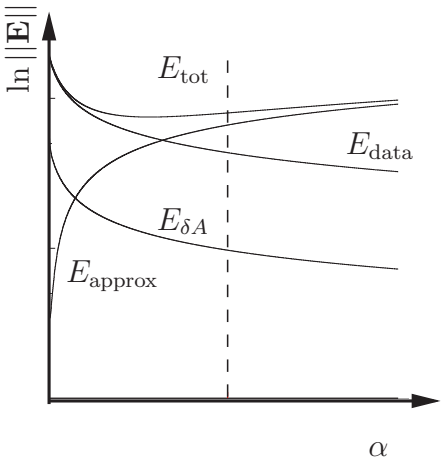

Figure 4.9: Behavior of the three components E_{data}, $E_{\delta A}$ and E_{approx} that contribute to the total uncertainty E_{tot} as functions of the regularization parameter α. The logarithm of the norm of the uncertainty vector is plotted. The dashed line marks the choice of α as discussed in section 4.4.2 for that special data sample. Numerical values for α can be found in Tab. 7.1.

4.4.2 Determination of the Regularization Parameter

The choice of the regularization parameter α is a compromise between accuracy and stability. An efficient and straightforward strategy is to look for a distribution which is regularized such that

$$||A\mathbf{x}_\alpha - \mathbf{y}^\delta|| = \delta \tag{4.12}$$

is satisfied. That means that the regularized histogram $\mathbf{x}_\alpha$ is in agreement with the observed histogram $\mathbf{y}^\delta$ after folding with the detector-response matrix A within the experimental errors. This solution can be uniquely found and the discrepancy principle (4.12) is regular in the sense that the exact solution is obtained as the error level $\boldsymbol{\delta}$ tends to zero:

$$\mathbf{x}_\alpha \to A^\dagger \mathbf{y}, \quad \text{for } \boldsymbol{\delta} \to 0.$$

Algorithms can be found that give α in a direct and not iterative way. In this analysis the algorithm described in [48] is modified because the measurement in the side bins is subject to larger experimental uncertainties and the content is not considered to be measured with the same quality as in the central bins. Hence only the central bins are used to find the regularization parameter α that solves the equation

$$\sum_{i=2}^{n-1}(A\mathbf{x}_\alpha - \mathbf{y}^\delta)_i^2 = \sum_{i=2}^{n-1}\delta_i^2\,. \tag{4.13}$$

α is well defined by that equation and can be found easily since Eqn. (4.13) only depends on α. It has to be stressed that one is essentially free in the choice of the regularization parameter α since the uncertainties introduced by it are taken into account properly. Of course, different methods to determine α lead to a different behavior of the solution $\mathbf{x}_\alpha$ as a function of the measurement error $\boldsymbol{\delta}$. The determination of the particular value of α described here is not optimal in terms of convergence rates for the limit

$$\mathbf{x}_\alpha \to \mathbf{x}_{\text{true}} = \mathbf{x}_{\alpha=0} \qquad \text{for } \boldsymbol{\delta} \to 0.$$

Interesting discussions about convergence rates can be found in the mathematical literature [49]. For a single measurement with $\boldsymbol{\delta}$ given by the statistics of the experiment like in this analysis, the question of convergence rates is of no further importance.

4.5 Discussion of Alternative Methods

Detailed introductions and descriptions of algorithms for alternative regularization methods can be found in references. Here only some advantages and disadvantages are mentioned briefly to explain the choice of the method described above.

- Truncated Singular Value Decomposition (TSVD)

  This method has no continuous regularization parameter but cuts away the contributions of the smallest singular values. Although the discrepancy principle is regular in the same sense as in the Tikhonov regularization, the results obtained have either quite large statistical errors or large approximation errors compared to the standard Tikhonov procedure. Especially for a small number of bins as is the case in this analysis, the method seems to be less efficient.

- Non-Standard Tikhonov Regularization

Penalty terms other than $\alpha||\mathbf{x}_\alpha||^2$ depending on preferences for the unfolded vector can be used. In general it is possible to have a penalty term $\alpha||L\mathbf{x}_\alpha||^2$ where L is a matrix. For a Tikhonov unfolding of the second kind a matrix L is introduced that estimates the curvature or second derivative of the spectrum with respect to x. Algorithms used in the standard Tikhonov unfolding can be widely used since in many cases a general Tikhonov unfolding can be transformed into a standard one. For this analysis it was found that a Tikhonov unfolding of the second kind does not improve the result significantly, so the simpler standard method seemed to be sufficient.

- Tikhonov-like Regularization with Nonlinear Penalty Terms

  Unfolding methods using nonlinear penalty terms are widely used. Instead of the norm $\alpha||L\mathbf{x}_\alpha||^2$ a function $S(\mathbf{x}, \alpha, \mathbf{y}^\delta)$ gives a measure of the stability of the unfolded solution. Especially probability functions with some "physical" motivation like Maximum Entropy or Shannon-Entropy [54] or similar functions are of interest. It could not be shown, that these entropy-based methods would improve the results of this analysis although they were studied in detail. But it was found, that simple algorithms, as for example suggested in [47], are not sufficient to ensure a proper convergence. There is no doubt, that these algorithms work well, as long as the condition of the matrix is not too bad, that means off diagonal elements are small and the singular values do not vary too much. It is especially useful in cases, where the measurement is mainly affected by a background noise level, rather than from resolution effects of the detector device. In our case that is not true and the algorithm failed frequently. Especially the fact, that an Entropy function is not defined for the (exact) maximum likelihood solution leads to some "minimum" regularization. The discrepancy principle is not regular. Even worse, the regularized solution contains unphysical values for a softer regularization. It seems not to be clear, whether and how matrix and approximation uncertainties are propagated. A more sophisticated discussion about convergence and algorithms of nonlinear regularization terms can be found in [49]. Studies of multidimensional unfolding using the Shannon-Entropy introduced in [47, 55] where not successful in our case. Apparent improvements came out to be a result of reprojecting the unfolded two-dimensional solution on the first dimension. In that process, the mean value is taken over all bins in the second dimension, which is less fluctuating than the values themselves. The same effect could be achieved by unfolding in more bins in a single dimension and averaging over some bins in a second step. The idea, that a measure in a second variable could improve the measurement by discriminating between better and less well measured events in the first variable, seems to be a valid and useful procedure in principle.

However, in the present case the number of well measured events is much smaller than the number of poorly measured events, so that there are no bins in the two dimensional $\mathbf{x}_{\text{vis}}$ array, where the detector resolution is significantly better than in others. Consequently the measurement does not profit from them. For the cross-entropy it would in principle be possible, to vary the size of the bins such, that better resolution in some bins is achievable. But then the number of events observed in those bins is so small, that statistical uncertainties dominate. For the Shannon-entropy the freedom of choice for a binning is limited, since the convergence of iterative algorithms depends on the fact, that the unfolded solution contains a similar number of events in each bin. A second argument against a cross-entropy based unfolding method was the need of some a-priori probability function for the unfolded spectrum.

There is no "perfect" unfolding technique for all kind of problems which might appear. The properties of the detector-response matrix and their consequences on the dominating uncertainties have to be checked carefully in order to chose a particular method.

Chapter 5

Data

This analysis is performed with data taken by the ALEPH experiment during the years 1998, 1999 and 2000 at six different e^+e^- centre-of-mass energies E_{cms}. The total integrated luminosity collected is $548.4\,\mathrm{pb}^{-1}$, where $177.0\,\mathrm{pb}^{-1}$ are taken at $\sqrt{s} = 189\,\mathrm{GeV}$, $82.6\,\mathrm{pb}^{-1}$ at $\sqrt{s} = 196\,\mathrm{GeV}$, $87.8\,\mathrm{pb}^{-1}$ at $\sqrt{s} = 200\,\mathrm{GeV}$, $71.6\,\mathrm{pb}^{-1}$ at $\sqrt{s} = 205\,\mathrm{GeV}$, $67.9\,\mathrm{pb}^{-1}$ at $\sqrt{s} = 206\,\mathrm{GeV}$ and $61.5\,\mathrm{pb}^{-1}$ at $\sqrt{s} = 207\,\mathrm{GeV}$. The data taken in the year 2000 ($\sqrt{s} = 205\,\mathrm{GeV} - 207\,\mathrm{GeV}$) are analyzed together. The other samples are processed separately for each centre-of-mass energy. All results are combined at a later stage of the analysis.

5.1 Preselection of $\gamma\gamma$ Events

In a first step of the data selection a clean sample of hadronic $\gamma\gamma$ events has to be obtained. Therefore cuts are applied to suppress background from e^+e^- annihilation and $\gamma\gamma$ events with a leptonic final state, i. e. $\gamma\gamma \to e^+e^-$ and $\gamma\gamma \to \mu^+\mu^-$.

5.1.1 Tag Definition

Since only single-tag events are taken into account in the analysis, the first criterion is the presence of exactly one tag candidate in the event. A tag candidate is defined as an energy-flow object detected either in SiCAL or in LCAL with an energy of at least 40% of the beam energy. The polar angle of the tag lepton with respect to the beam axis has to be larger than 32 mrad.

5.1.2 Cut on Background Sources

For events identified as single tag events, certain cuts on the properties of the final state are applied. The invariant mass of the final state excluding the tag

has to be larger than 2.5 GeV. This cut excludes exclusive resonance production and is also necessary because of uncertainties in the Monte Carlo simulations. For invariant masses below that, the simulations are considered not to describe reality well enough.

No events with less than three charged particles in the final state are accepted. This cut efficiently discriminates against $\gamma\gamma \to e^+e^-$ and $\gamma\gamma \to \mu^+\mu^-$. To exclude this leptonic final states there may also no energy-flow object be identified as electron or muon. In the energy-flow algorithm leptons can only be identified if their momentum is larger than about 1.4 GeV for electrons and 2.4 GeV for muons. Leptons generated in the hadronic system as decay products or from γ conversion are usually softer and not affected by this cut on identified leptons.

It has to be mentioned that the use of energy-flow objects implies some intrinsic cuts performed to ensure a certain data quality. For charged particles this includes a minimum of four hits in the TPC and a shortest distance from the nominal interaction point of not more than 20 cm in the z direction and 2 cm in the plane perpendicular to the beam axis. For more details see [43].

The total energy of charged and neutral objects measured excluding the tag lepton must not exceed 70 GeV to avoid background from annihilation events.

The preselection is done with the same cuts for all centre-of-mass energies and results in a sample of **20188** events collected at $\sqrt{s} = 189\,\text{GeV}$, **8748** events at $\sqrt{s} = 196\,\text{GeV}$ and **8768** events at $\sqrt{s} = 200\,\text{GeV}$. For energies $205\,\text{GeV} \leq \sqrt{s} \leq 207\,\text{GeV}$ **19450** events were selected.

5.2 Final Selection and Data Sample

The final data sample is selected in a second step with slightly different cuts for different centre-of-mass energies. Since the mean Lorentz boost of the $\gamma\gamma$ events varies with the beam energy, the acceptance changes and different detector-response matrices account for the experimental setup. Cuts are chosen in such a way, that a variation has minimal effect on the results.

The data sample is divided in two different bins of the virtuality Q^2 of the probing photon. The border between lower and upper bin is given by a minimum in the Q^2 spectrum as shown in Fig. 5.1. It originates from the reduced acceptance in the overlap region between the two luminosity calorimeters SiCAL and LCAL.

The final binning and the mean value of Q^2 can be read off from Tab. 5.1. There also the numbers of selected events are presented that have survived all cuts suppressing the background as discussed later in this section.

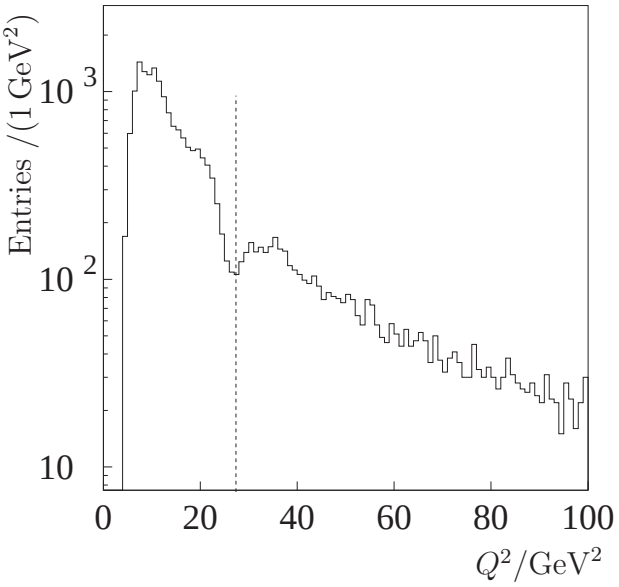

Figure 5.1: Q^2 spectrum for data taken at $\sqrt{s} = 189\,\text{GeV}$. The separation between the lower and the upper Q^2 bin is done at $Q^2 = 27\,\text{GeV}^2$ as indicated by the dashed line.

5.2.1 Background Processes

Four different kinds of background are discussed. For most of them the same cuts are applied for all different centre-of-mass energies. Exceptions are mentioned explicitly.

Off-momentum electrons

The major background after data preselection is due to so called off-momentum electrons. These are beam electrons which - having lost an appreciable amount of energy through synchrotron radiation - are no longer focused on the orbit of the storage ring but are lost from the lepton bunch. They are preferentially emitted in the LEP plane, mostly around an azimuthal angle of $\varphi \approx \pi$, which is the direction pointing away from the center of the LEP ring.

If such an off-momentum electron is scattered into the luminosity calorimeter at the same time together with a no-tag $\gamma\gamma$ event, it is impossible to distinguish such an event from a single-tag event as used for this analysis.

The properties of off-momentum background are studied in detail in [56]. The value of Q^2 for such a fake tag lepton is typically small ($< 15\,\text{GeV}^2$) since the energy of the electron is usually below 80% of the beam energy and the reconstructed scattering angle is not larger than 45 mrad. With elliptical cuts in the ϑ-φ plane as shown in Fig.5.2 (a) and a requirement for the energy of the tag lepton of at least $70\% \times E_{\text{beam}}$ (Fig.5.2 (b)) the off-momentum background can be suppressed significantly. The remaining contribution to the final data sample

E_{cms} /GeV	# of events	Q^2 range /GeV^2	$\langle Q^2 \rangle$ /GeV^2
189	5411	10-27	16.1
189	3537	27-250	61.7
196	2577	10-28	16.7
196	1643	28-250	65.7
200	2694	10-29	17.4
200	1648	29-250	68.3
205-207	6167	10-32	18.4
205-207	3560	32-250	72.9
$\sum$	15849	$\langle Q^2 \rangle = 17.3\,\mathrm{GeV}^2$	
	10388	$\langle Q^2 \rangle = 67.2\,\mathrm{GeV}^2$	

Table 5.1: Number of selected events after all cuts listed for all centre-of-mass energies and Q^2 ranges. The range of Q^2 of the two bins analyzed is given in column three. Background is not yet subtracted.

can be estimated to be not more than 1% in the low Q^2 sample. As a Boolean expression the off-momentum cut reads as follows:

$$
\begin{aligned}
E_{\mathrm{Tag}} \quad &> \quad 0.7 \cdot E_{\mathrm{beam}} \\
&\text{.AND.} \\
\Big[\text{If } E_{\mathrm{Tag}} \quad &< \quad 0.8 \cdot E_{\mathrm{beam}} \\
&\text{then} \\
1 \quad &< \quad \left(\frac{\varphi - \pi}{HA_\varphi}\right)^2 + \left(\frac{\frac{\pi}{2} - \left|\frac{\pi}{2} - \vartheta\right| - 0.035}{HA_\vartheta}\right)^2 \quad \text{.AND.} \\
1 \quad &< \quad \left(\frac{\pi - |\pi - \varphi|}{HA_\varphi}\right)^2 + \left(\frac{\frac{\pi}{2} - \left|\frac{\pi}{2} - \vartheta\right| - 0.035}{HA_\vartheta}\right)^2 \Big] .
\end{aligned}
$$

The free parameters $HA_{\varphi/\vartheta}$ determine the size of the half axes in φ and ϑ direction of the ellipses used for cutting. There is no need to introduce different parameters for the elliptic cut that excludes off-momentum leptons which were scattered around $\varphi \approx \pi$ and those which were scattered around $\varphi \approx 0$. At ALEPH the direction $\varphi = 0$ lies in the LEP plane and points towards the center of the LEP ring. The final cuts are

$$
\begin{aligned}
HA_\vartheta &= 8\,\mathrm{mrad}, \text{ and} \\
HA_\varphi &= 5\,\mathrm{mrad}\,.
\end{aligned}
$$

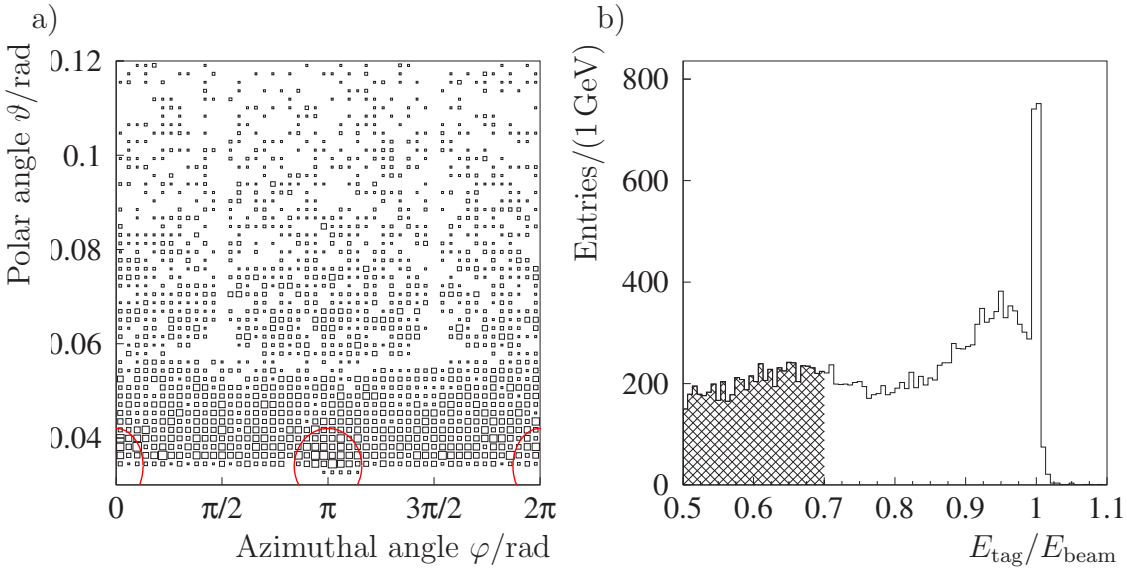

Figure 5.2: Contamination of the data sample by off-momentum electrons can be seen in the $\vartheta - \varphi$-plane (a). They are preferably radiated in the LEP plane, $\varphi \approx 0/\pi/2\pi$. The elliptic cuts are drawn as performed in the analysis. Histogram (b) shows the dominance of off-momentum background for small tag energies compared to the continuously falling spectrum of the tag electrons from $\gamma\gamma$ events. The hatched part reflects events rejected by the cut on E_{tag}.

The angular distribution of the tag leptons azimuthal angle φ is plotted in Fig.5.3. The histogram shows the angular distribution after the cuts against off-momentum background have been applied. The hatched histogram plotted on top of it presents the events which are rejected by the elliptic cut. The data sample containing the upper Q^2 bin is not affected by off-momentum contamination.

Beam-gas interaction

Interactions of the beam leptons with remaining gas molecules inside the beam pipe can be excluded to a large extent by an additional cut on the interaction vertex. The reconstructed vertex of the $\gamma\gamma$ events has to be located inside a cylindrical volume around the nominal interaction point with a length of 10 cm in z direction ($\pm\,5\,$cm from main vertex) and a radius of 1 cm.

Background from $\gamma\gamma$ and annihilation processes

Several processes at a e^+e^- collider can show a signature similar to the typical topology of a hadronic single-tag $\gamma\gamma$ event. First there are $\gamma\gamma$ events with leptonic

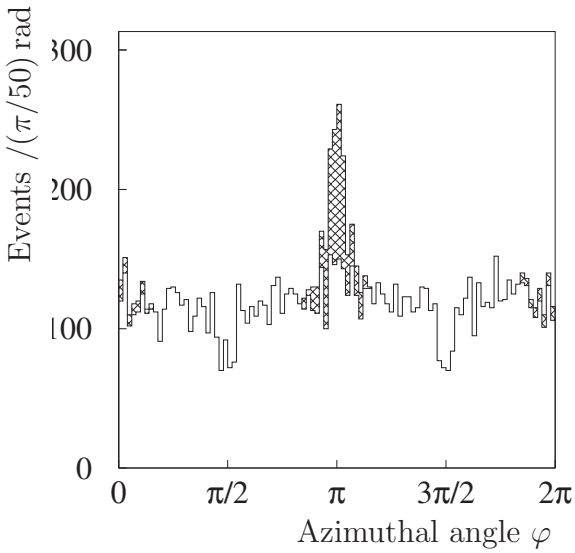

Figure 5.3: Distribution of azimuthal angle φ after off-momentum cuts have been applied. The hatched histogram accounts for those events which are excluded by the elliptic cut. A cut $E_{\mathrm{Tag}} \geq 0.7 \cdot E_{\mathrm{beam}}$ has been performed before.

final state:

$$\begin{aligned} \gamma\gamma &\rightarrow \mathrm{e}^+\mathrm{e}^- \\ \gamma\gamma &\rightarrow \mu^+\mu^- \\ \gamma\gamma &\rightarrow \tau^+\tau^- \end{aligned}$$

The contamination by the first two processes can be kept small by the cut on the minimal number of charged particles ($N_{\mathrm{chrg}} \geq 3$). The $\tau^+\tau^-$ final state events cannot be suppressed that easily because the τ lepton decays inside the beam pipe and can produce a multi-particle final state like a hadronic interaction. The tau leptons cannot be fully reconstructed due to the fact that not all decay products are detected. As for all other background where no special cuts can be applied for an identification, also the background from τ pair production has to be simulated with Monte Carlo techniques and subtracted from the data. Fortunately these background processes are usually much better understood than the hadron production in $\gamma\gamma$ events that is investigated here.

Background from annihilation processes originates from

$$\begin{aligned} \mathrm{e}^+\mathrm{e}^- &\rightarrow \mu^+\mu^- \\ \mathrm{e}^+\mathrm{e}^- &\rightarrow \tau^+\tau^- \\ \mathrm{e}^+\mathrm{e}^- &\rightarrow q\bar{q} \\ \mathrm{e}^+\mathrm{e}^- &\rightarrow We\nu \\ \mathrm{e}^+\mathrm{e}^- &\rightarrow Zee \end{aligned}$$

The most important criterion to exclude these events is to reject all events with a reconstructed invariant mass of more than 50 GeV.

In Tab. 5.2 the various physics processes that contribute to background are listed together with the Monte Carlo generator used for simulation and determination of the cross section of the process. The contamination of the final data sample is listed in Tab. 5.3. The cross section is given for a centre-of-mass energy of 200 GeV although it varies slightly for energies between 189 GeV and 207 GeV. Of course the exact centre-of-mass energy is used for the correction.

Process	MC Generator	σ [pb] (@200 GeV)	# simulated events [1000] @189/196/200/205 − 207 GeV
$\gamma\gamma \to e^+e^-$	PHOT02	9617.5	3400/3600/3600/1200
$\gamma\gamma \to \mu^+\mu^-$	PHOT02	4480.2	3200/3600/3600/1200
$\gamma\gamma \to \tau^+\tau^-$	PHOT02	452.0	500/600/600/600
$e^+e^- \to q\bar{q}$	PHYTHIA	88.1	960/2000/2000/490
$e^+e^- \to \mu^+\mu^-$	KORL08	7.3	150/70/100/50
$e^+e^- \to \tau^+\tau^-$	KORL08	7.3	150/140/200/100
$e^+e^- \to We\nu$	PHYTHIA	0.8	200/100/100/200
$e^+e^- \to Zee$	PHYTHIA	99.0	1960/800/900/600

Table 5.2: Various background processes from two-photon collisions and annihilation events. The Monte Carlo generators will be explained in more detail in chapter 6.1.

Q^2 resolution effects

The detector response matrix A introduced in chapter 4 is generated from a large Monte Carlo sample in such a way, that the matrix corrects the x distribution for events generated in a certain Q^2 range which are also reconstructed with a virtuality inside the same Q^2 range. It is clear that events which are reconstructed at other values of Q^2 are simply treated as being lost through inefficiency.

More difficult is the migration of events into the considered Q^2 region. In Fig. 5.4 this effect is illustrated in the Q^2_{true}-Q^2_{vis} plane. Events generated at other values of Q^2 which are selected by the data sample have to be treated as background and must be subtracted. Unfortunately there is no way to identify those events. The background has to be simulated the same way as other physics background processes. Of course the hadronic structure function has to be known in the Monte Carlo calculations and consequently a model dependence is introduced. The contamination of the selected data sample calculated with a GRV-LO parametrization used for the simulation is less than 5% in the low Q^2 region and approximately 2% for the upper Q^2 region. Exact numbers can be found in Tab. 5.3. It has been checked that the use of different parametrizations has

Process	Contamination [%]			
	$\langle Q^2 \rangle = 17.3\,\mathrm{GeV}^2$			
	189 GeV	196 GeV	200 GeV	$205 - 207$ GeV
$\gamma\gamma \to \mathrm{e^+e^-}$	0.22±0.03	0.26±0.05	0.25±0.05	0.27±0.09
$\gamma\gamma \to \mu^+\mu^-$			< 0.1	
$\gamma\gamma \to \tau^+\tau^-$	3.4±0.1	3.9±0.1	4.1±0.1	4.3±0.1
$\mathrm{e^+e^-} \to q\bar{q}$	0.24±0.01	0.23±0.01	0.24±0.01	0.22±0.01
$\mathrm{e^+e^-} \to \mu^+\mu^-$			< 0.1	
$\mathrm{e^+e^-} \to \tau^+\tau^-$			< 0.1	
$\mathrm{e^+e^-} \to We\nu$			< 0.1	
$\mathrm{e^+e^-} \to Z\mathrm{ee}$	0.15±0.01	0.14±0.01	0.16±0.01	0.15±0.01
Q^2 resolution	4.97±0.06	4.17±0.05	3.80±0.05	2.50±0.04
	$\langle Q^2 \rangle = 67.2\,\mathrm{GeV}^2$			
	189 GeV	196 GeV	200 GeV	$205 - 207$ GeV
$\gamma\gamma \to \mathrm{e^+e^-}$	0.3±0.04	0.22±0.05	0.31±0.07	0.41±0.14
$\gamma\gamma \to \mu^+\mu^-$			< 0.1	
$\gamma\gamma \to \tau^+\tau^-$	6.1±0.2	6.6±0.2	7.1±0.2	7.0±0.2
$\mathrm{e^+e^-} \to q\bar{q}$	0.88±0.02	0.91±0.02	0.93±0.02	0.98±0.03
$\mathrm{e^+e^-} \to \mu^+\mu^-$			< 0.1	
$\mathrm{e^+e^-} \to \tau^+\tau^-$			< 0.1	
$\mathrm{e^+e^-} \to We\nu$			< 0.1	
$\mathrm{e^+e^-} \to Z\mathrm{ee}$	0.61±0.01	0.55±0.02	0.58±0.02	0.62±0.02
Q^2 resolution	1.72±0.04	1.63±0.04	1.79±0.04	2.35±0.05

Table 5.3: Contamination of the selected data sample through background processes.

almost no effect on the unfolded results since the main reason for this migration is the limited energy resolution of the tag lepton in the luminosity calorimeter.

5.2.2 Observed Data

The number of observed events after all selection cuts and background subtraction can be read off in Tab. 5.4. The binning in the measured quantity x can be taken from that table as well. For a Monte Carlo sample, that consists of all generated true events, it has been chosen such that the number of entries in each bin would be the same.

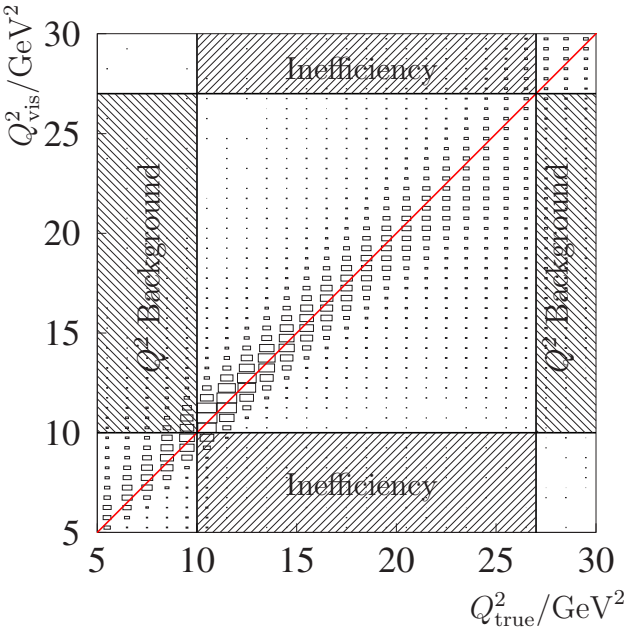

Figure 5.4: Q^2 resolution as determined from Monte Carlo studies. The hatched areas account for events which contribute to inefficiencies or to the Q^2 resolution background as discussed before.

x Bin	$\langle Q^2 \rangle = 17.3\,\mathrm{GeV}^2$			
$\sqrt{s} =$	189 GeV	196 GeV	200 GeV	205 − 207 GeV
0.0020 - 0.0110	68.8	22.8	28.3	72.6
0.0110 - 0.0338	395.1	227.9	217.9	505.8
0.0338 - 0.0787	671.5	325.9	358.6	775.5
0.0787 - 0.1487	859.9	397.8	424.0	971.2
0.1487 - 0.2429	861.8	412.1	439.0	943.0
0.2429 - 0.3624	895.2	423.0	419.5	954.3
0.3624 - 0.5074	898.3	379.8	400.9	992.8
0.5074 - 0.7000	329.8	182.8	193.5	517.9
x Bin	$\langle Q^2 \rangle = 67.2\,\mathrm{GeV}^2$			
$\sqrt{s} =$	189 GeV	196 GeV	200 GeV	205 − 207 GeV
0.0060 - 0.0362	67.9	34.2	37.0	68.2
0.0362 - 0.0950	302.1	145.5	139.6	297.2
0.0950 - 0.1811	385.5	182.9	208.9	381.5
0.1811 - 0.2907	460.8	227.9	204.4	441.3
0.2907 - 0.4204	475.5	216.0	214.6	482.7
0.4204 - 0.5714	543.3	219.6	257.6	564.5
0.5714 - 0.7356	574.0	259.3	220.8	517.8
0.7356 - 0.9600	396.9	199.1	192.1	415.2

Table 5.4: Background-corrected number of observed events in two bins in Q^2 and eight bins in the Bjorken variable x listed separately for each analyzed centre-of-mass energy.

Chapter 6

Monte Carlo Simulation

6.1 Generators

Monte Carlo simulations are used on the one hand for the construction of the detector-response matrix and on the other hand for the simulation of background processes. The latter is done with the generators listed in Tab.5.2. They were tuned for the ALEPH experimental setup. Since no adaption of these generators is needed for this analysis, simulated events were taken from the central ALEPH Monte Carlo production. Details can be found in the KINGAL documentation [57, 58].

For the construction of the detector-response matrix, a set of two-photon events has to be generated. The HERWIG program is used in version 6.2 with the general ALEPH tuning parameters also found in the documentation of the official ALEPH Monte Carlo production mentioned above. A parametrization for the structure function F_2^γ has to be used by the generator. It is possible to choose sets of parameters from the library of parton density functions PDFLIB [59]. Two different samples of Monte Carlo events have been produced for each LEP energy that is analyzed separately. In one of them a parametrization according to GRV-LO (PDFLIB Nptype=3/Ngroup=5/Nset=3) has been applied and the second sample is generated with a structure function as given by SaS-1D (PDFLIB Nptype=3/Ngroup=9/Nset=5) Each sample consists of 1 000 000 events.

For the details of the event simulation in the HERWIG program and the cluster fragmentation model see the references [60–65].

6.2 Comparison of Data and Monte Carlo Simulation

For a comparison between observed data and events generated by the Monte Carlo methods, important event quantities are plotted in histograms below. The data points show the sample after subtraction of all background sources. The histograms for the Monte Carlo samples are normalized to the data luminosity to compare not only the shape of the distributions but also their absolute normalization. The GRV-LO sample is drawn with a solid line, the dashed line shows the spectra from the SaS-1D sample. In addition the spectra for annihilation background $e^+e^- \to q\bar{q}$ and from $\gamma\gamma \to \tau\tau$ are plotted as well as the background due to resolution effects in the Q^2 measurement. The histograms of the background processes are plotted on top of each other so that the degree of contamination can easily be seen in comparison to observed data.

6.3 Construction of the Detector-Response Matrix

The detector-response matrix A describes the effects of the experimental setup on data. For the spectrum of the measured variable that means either an inefficiency or a migration of events within the histogram due to an imperfect measurement. It is important to know for a sample of events both the true information about the quantity of interest and the value that would be measured in the detector. For that reason the $\gamma\gamma$ Monte Carlo sample mentioned above is subjected to a full detector simulation and to the same reconstruction algorithm as used on real data. The detector simulation is done by the GALEPH program [66], a GEANT [67] based simulation of the ALEPH detector. JULIA [68] is used for the reconstruction of the events. The events of the Monte Carlo sample undergo the same selection cuts on their reconstructed quantity as the real data do.

The spectrum of the measured Bjorken variable x is divided into a certain number of N bins. For a given Q^2 range, in which the structure function is to be measured, and for a minimum true hadronic mass of 2.5 GeV, the number of events generated in each x bin j has to be determined:

$$n_{j,\,\mathrm{true}} = \text{Number of events generated in } x \text{ bin } j, \;\; j = 1, ..., N$$

This is done for all generated events, even if they do not pass the selection cuts on their reconstructed properties. The cut on the true hadronic mass is done because of uncertainties in the Monte Carlo generator for production of low mass final states. The cut has to be well below the cut on the visible hadronic mass.

The matrix element A_{ij} is then defined as

$$A_{ij} = \frac{n_{(i,\,\mathrm{vis}|j,\,\mathrm{true})}}{n_{j,\,\mathrm{true}}}$$

with $n_{(i,\,\mathrm{vis}|j,\,\mathrm{true})}$ being the number of events generated in x bin j but reconstructed in x bin i. The efficiency for all events generated in bin j is then

$$\epsilon_j = \sum_{i=1}^{N} A_{ij} \leq 1.$$

The detector-response matrix shows a lot of migration between bins which lead to large off diagonal elements. Consequently strong correlations between the measured points of the structure function F_2^γ are expected.

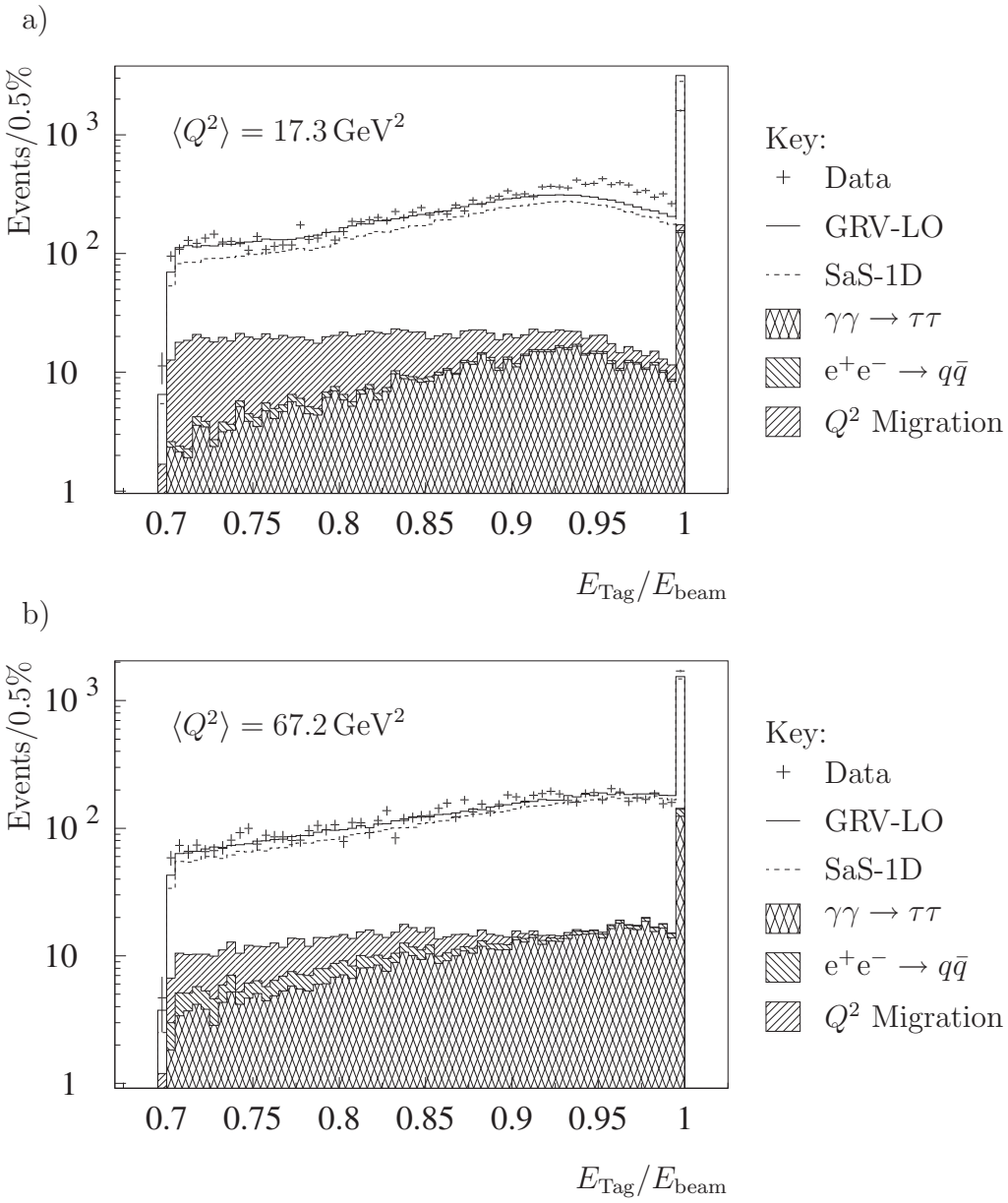

Figure 6.1: The diagrams show the energy spectrum of the tagged beam leptons. Data measured with the ALEPH detector are compared to Monte Carlo simulations based on either GRV-LO parametrization or on the SaS-1D set of parameters. The hatched histograms present the contamination by the three main types of background plotted on top of each other. All histograms are normalized to the data luminosity. In plot (a) the diagrams of the low Q^2 are drawn, plot (b) contains data from the high Q^2 region.

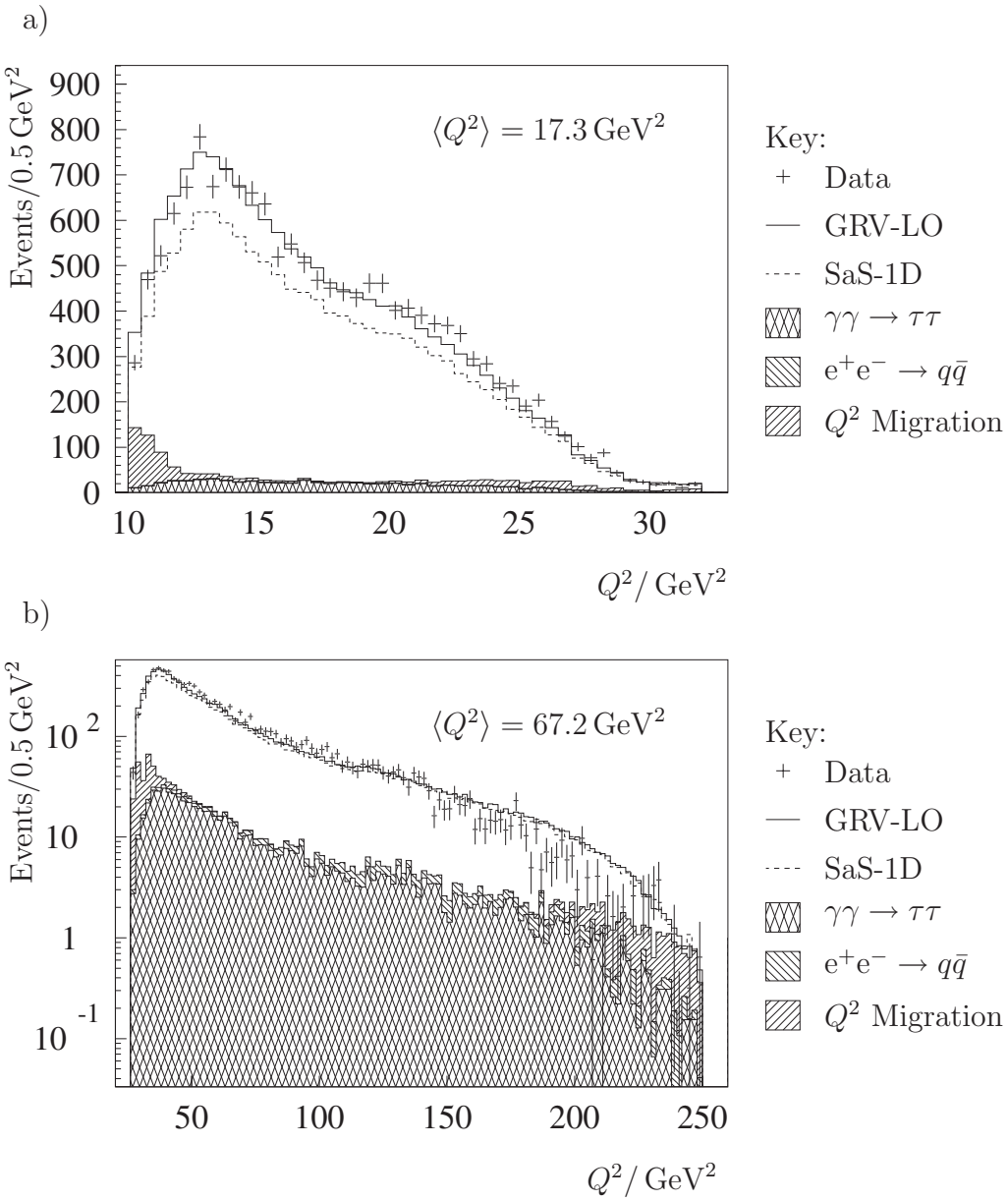

Figure 6.2: Comparison between ALEPH data and Monte Carlo for the virtuality Q^2 of the photon radiated by the tagged beam lepton.

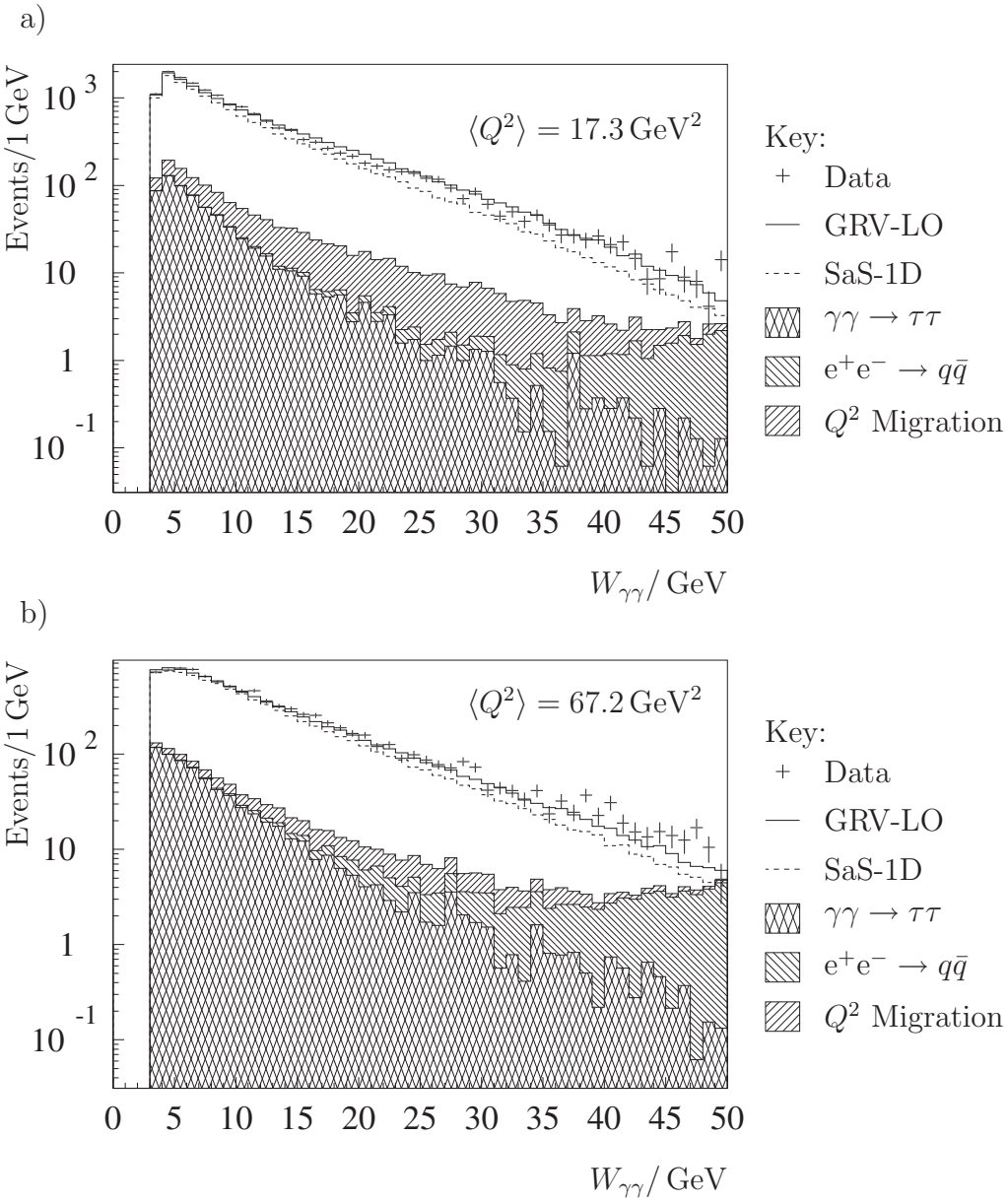

Figure 6.3: Diagrams as in Fig. 6.1 but for the visible invariant hadronic mass $W_{\gamma\gamma}$.

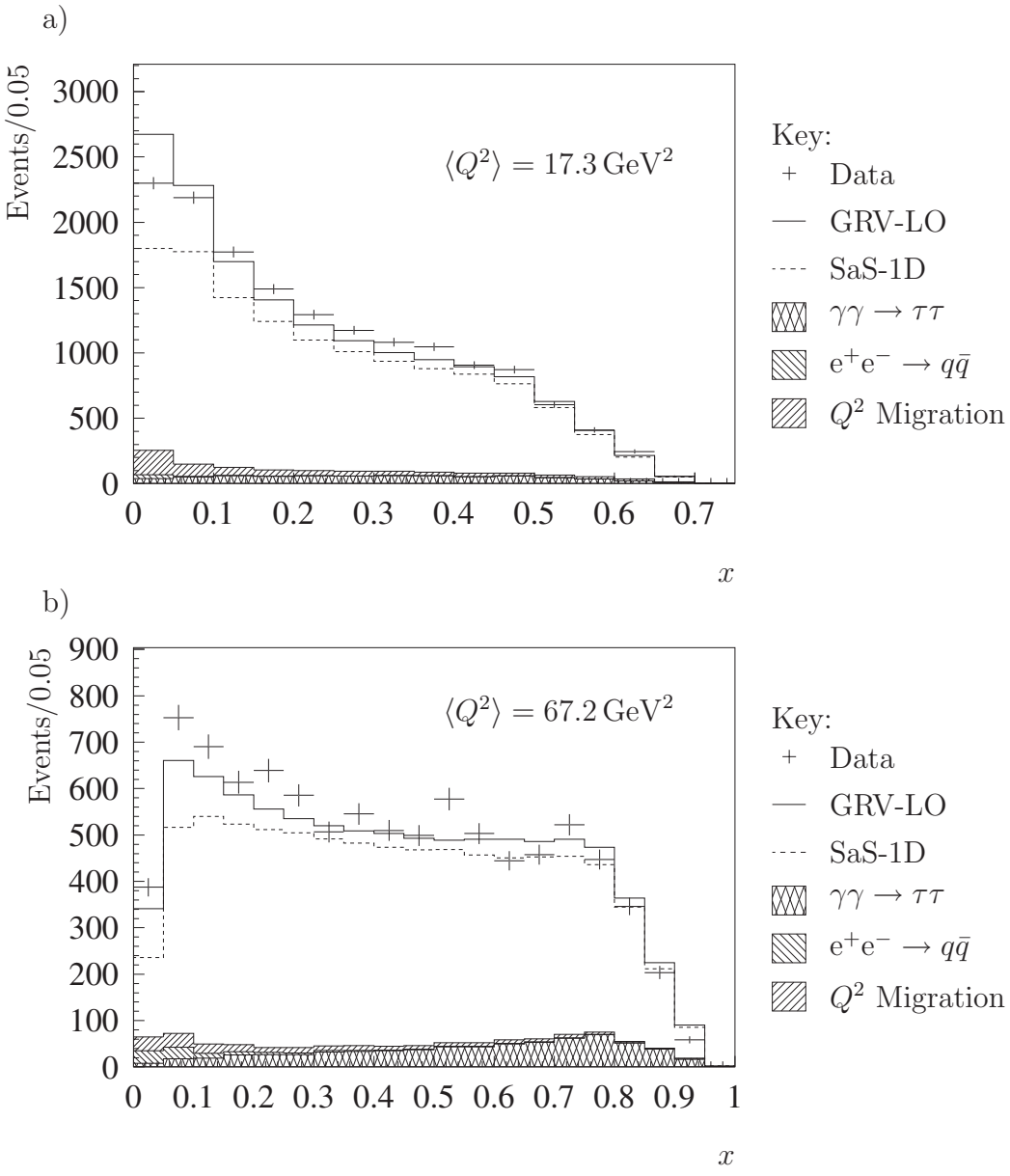

Figure 6.4: Bjorken variable x as seen in the experiment and simulated by Monte Carlo programs.

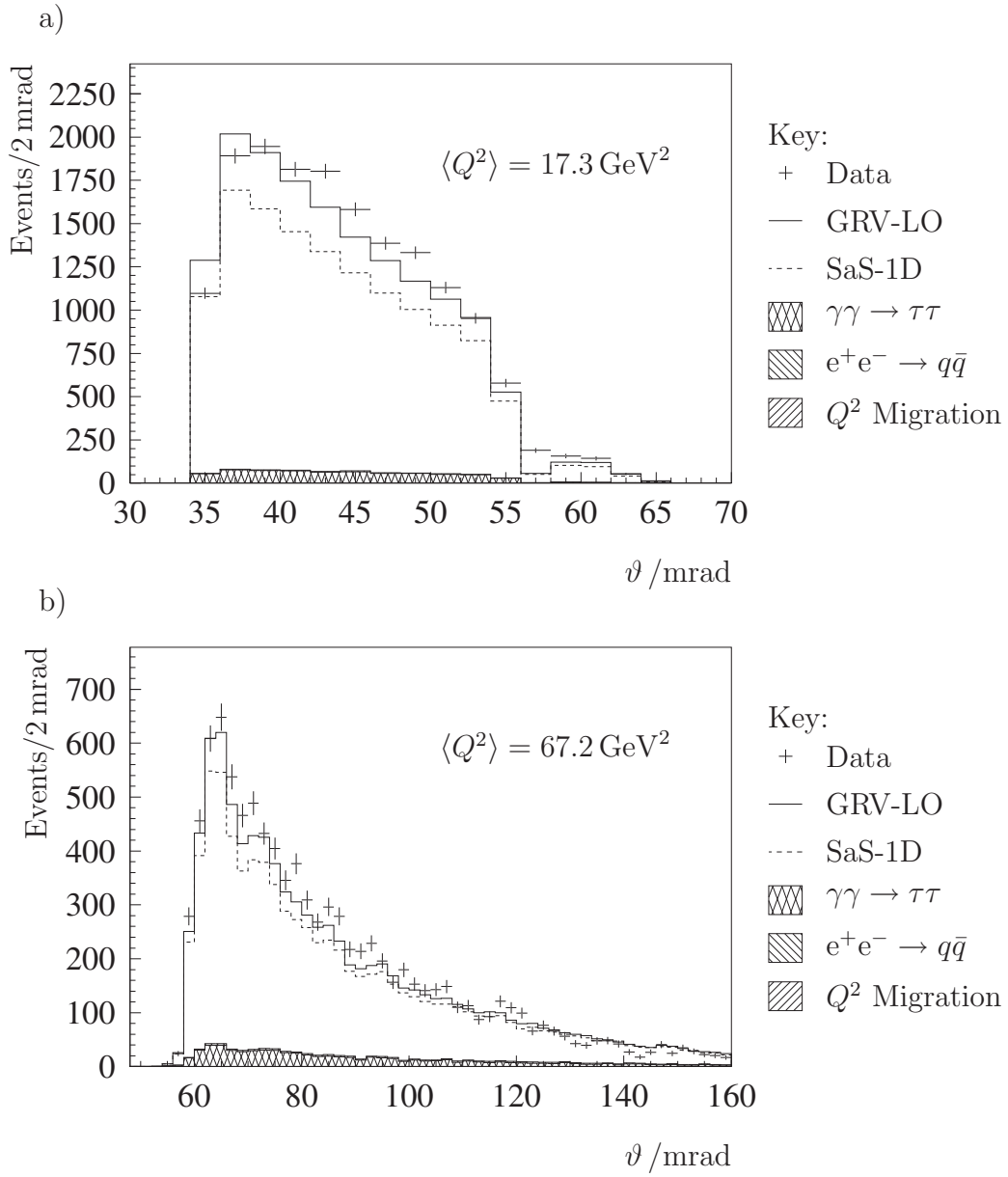

Figure 6.5: Distributions of the scattering angle ϑ of the tag electron with respect to the beam direction.

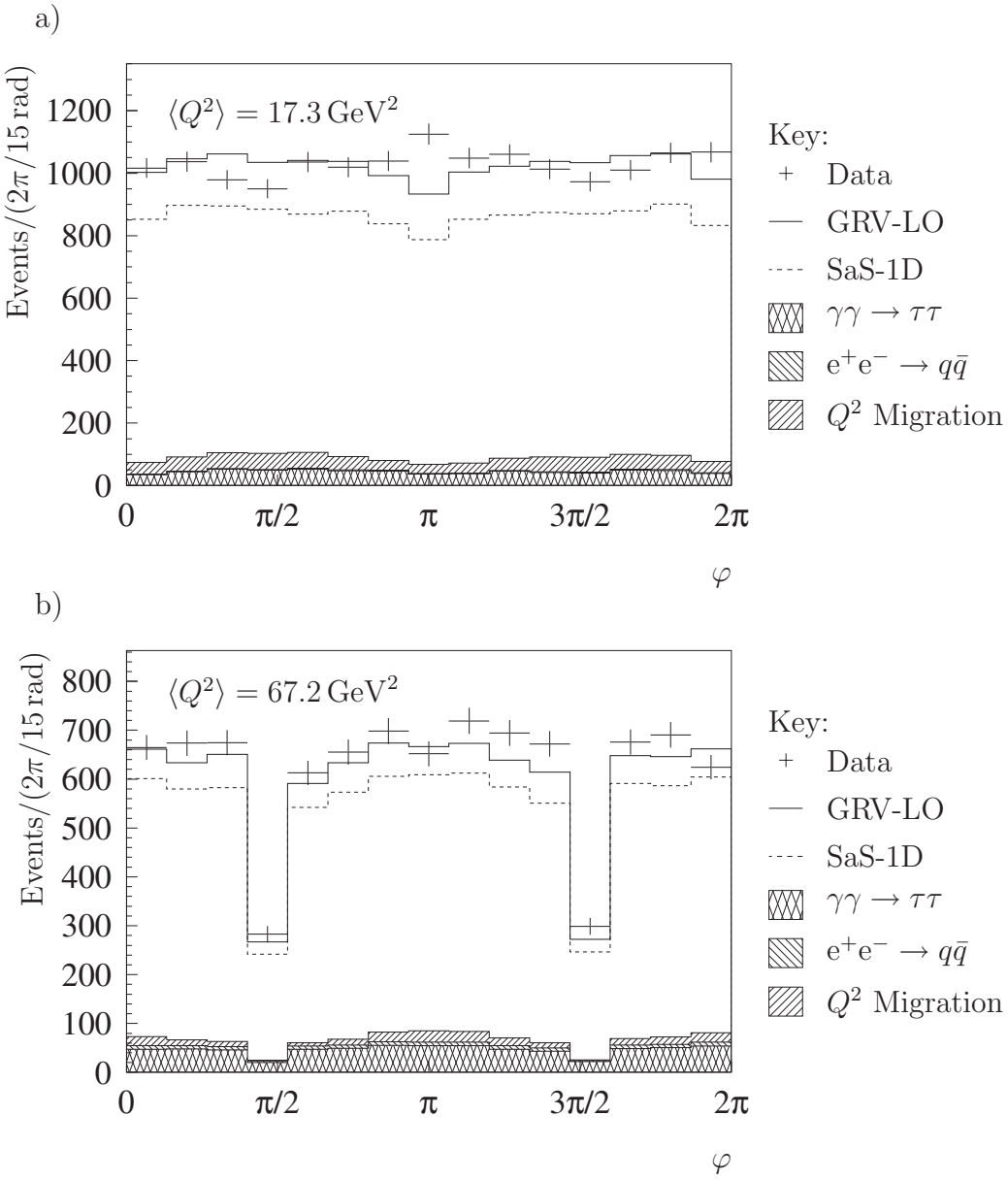

Figure 6.6: The histograms show the azimuthal angle φ of the tagged beam lepton. The two dips in the spectrum of high Q^2 tag electrons appear because of inefficiencies at the borders of the two LCAL modules. Each of them covers an azimuthal angle of π.

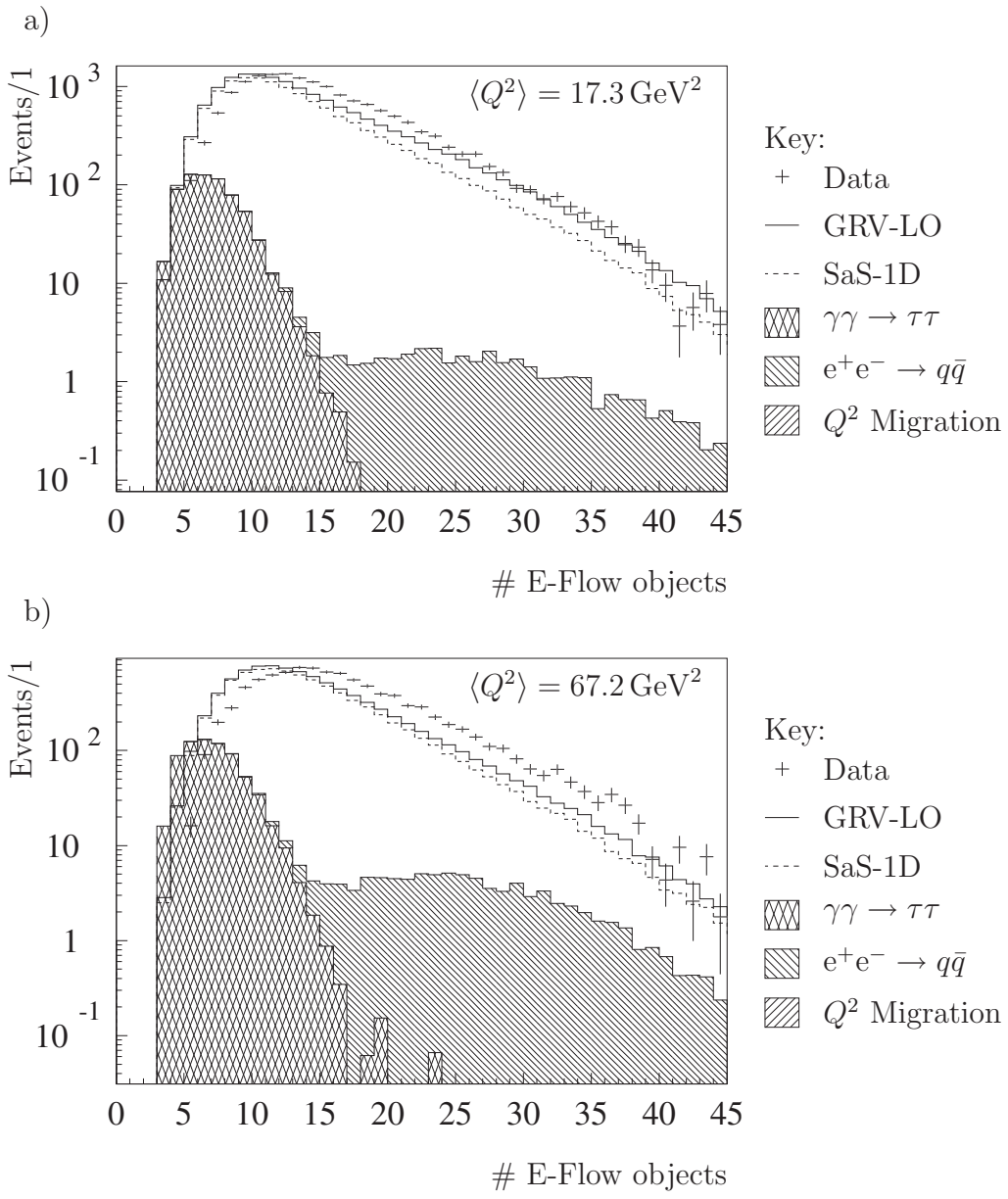

Figure 6.7: Comparison of reconstructed number of energy-flow objects in Monte Carlo and ALEPH data. The histograms contain both charged and neutral objects. It seems that the spectrum of the ALEPH data is shifted by about two units towards larger multiplicity compared to the Monte Carlo simulations.

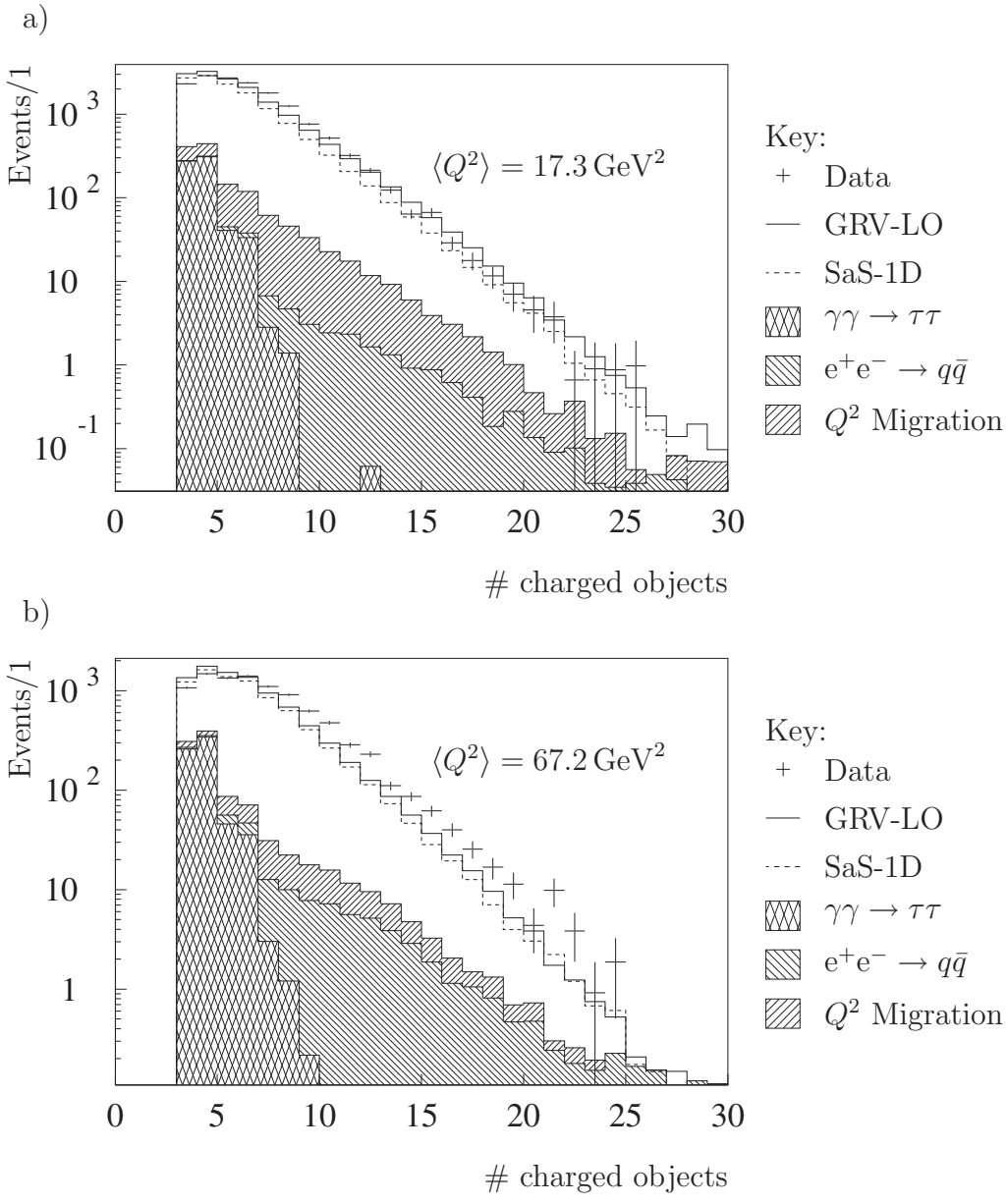

Figure 6.8: The diagrams plotted give the number of reconstructed charged particles in an event. The multiplicity of the data events again seems to be slightly larger than in Monte Carlo simulations for high Q^2. In the upper diagram for low Q^2 the agreement seems to be better.

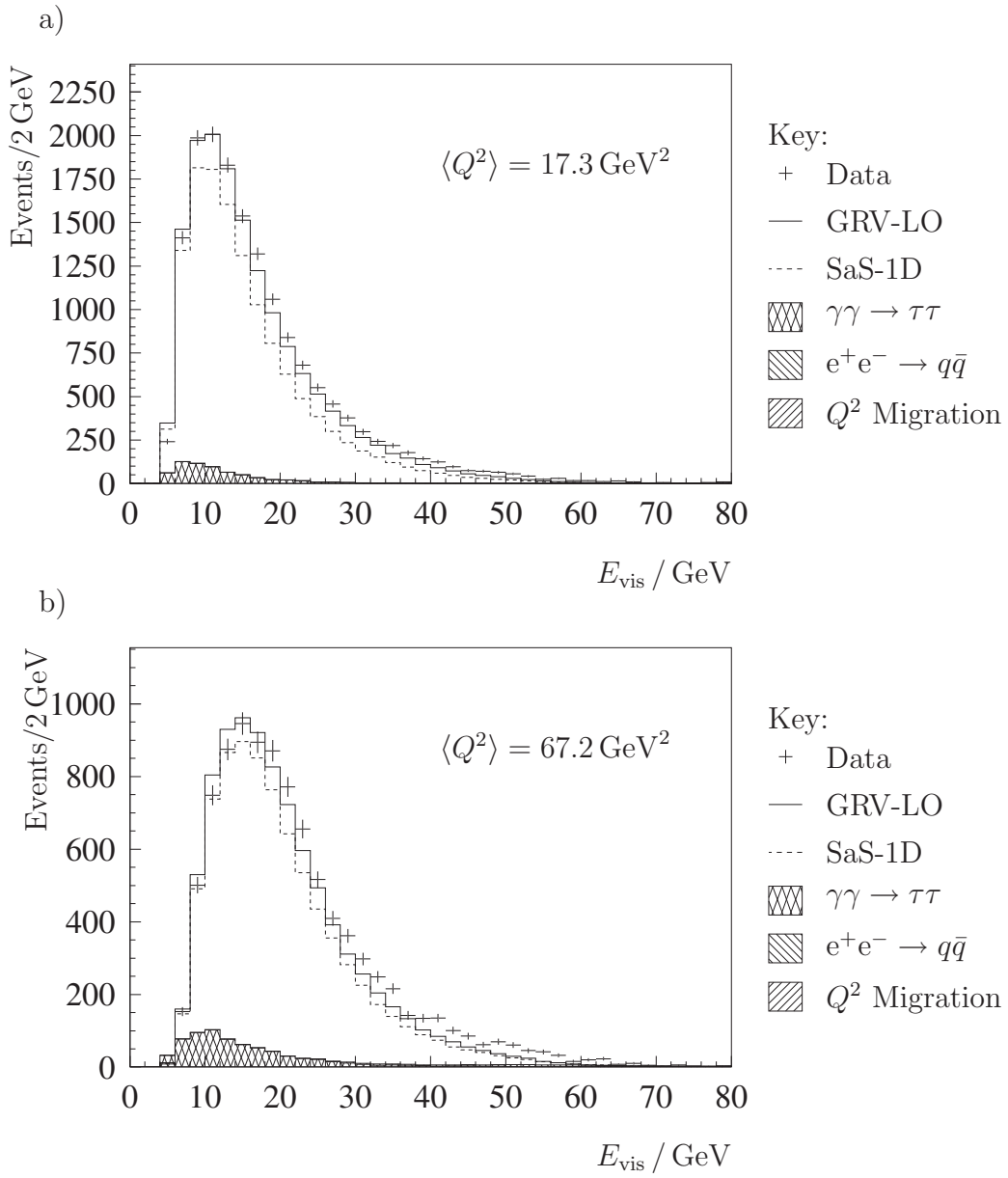

Figure 6.9: Same comparison as in the figures above but for the total reconstructed energy excluding the tag electron.

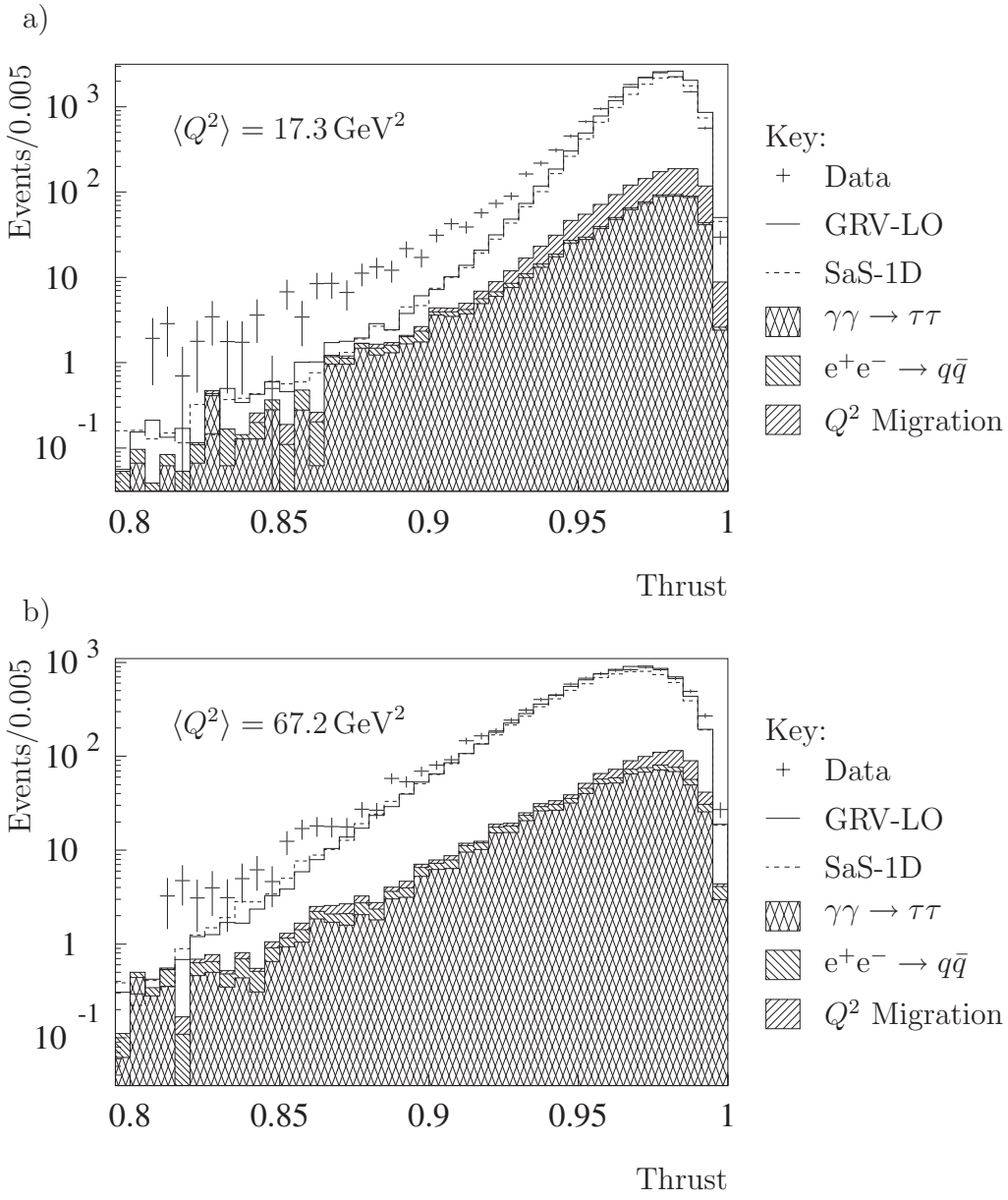

Figure 6.10: Monte Carlo simulated thrust of the reconstructed hadronic system compared to measured data. The reason for the disagreement between data and simulations is not clear. A possible explanation could be that there are more three-jet like events in data than are produced in Monte Carlo calculations. More higher order corrections in the simulations might be able to account for the difference.

Chapter 7

Measurement and Results

In this section the measurement is described in detail. Since the structure function $F_2^\gamma(x, Q^2)$ is proportional to the differential cross section $\mathrm{d}^2\sigma/\mathrm{d}x\mathrm{d}Q^2$, it is necessary to obtain the corrected x spectrum and integrate over a range in Q^2. That is done in the measurement, where the structure function is given at the mean value of Q^2. The spectrum of the Bjorken variable x is divided into eight bins, the binning can be read off from Tab. 5.4 in Chap. 5. It has been checked that the results are sufficiently insensitive to reasonable changes in the bin bounderies.

7.1 Observed Data

After applying all selection cuts discussed in Chap. 5 and after subtraction of background the visible spectra shown in Fig.7.1 and 7.2 are obtained. The histograms are shown with a logarithmic x axis for the low Q^2 samples. Error bars indicate statistical errors only. In addition there are the re-folded histograms plotted into the same diagrams. They were obtained when the distributions from the regularized Tikhonov unfolding are again multiplied with the original detector-response matrix. The histogram drawn with a dashed line shows the re-folded distribution obtained from a matrix that is based on the GRV-LO Monte Carlo sample. The SAS-1D detector-response matrix is used for the histogram drawn with the dotted line. These tests are done to demonstrate that the spectra achieved with the regularized unfolding method applied here are consistent with the measured data within statistical errors.

7.2 Unfolding Parameters

A Tikhonov regularization method as described in Chap.4 has been applied to the visible spectra shown in the previous section. The regularization parameter

α has been determined according to Eqn. (4.13). In Tab.7.1 and 7.2 the obtained parameters as well as the condition numbers of the original and the regularized system are listed. The condition number, beeing the ratio of the modulus of the largest and the smallest eigenvalue, is significantly lower for the regularized system. Therefore a better stability in the unfolded spectrum is ensured.

	189 GeV	196 GeV	200 GeV	205 − 207 GeV
Matrix build from GRV-LO Monte Carlo sample				
$\mathrm{cond}(A^{\mathrm{T}}A)$	$1.7 \cdot 10^6$	$1.7 \cdot 10^6$	$3.0 \cdot 10^6$	$3.2 \cdot 10^6$
α	$3.2 \cdot 10^{-3}$	$6.0 \cdot 10^{-3}$	$5.9 \cdot 10^{-3}$	$2.7 \cdot 10^{-3}$
$\mathrm{cond}(\alpha I + A^{\mathrm{T}}A)$	52.7	25.8	25.1	45.8
Matrix build from SaS-1D Monte Carlo sample				
$\mathrm{cond}(A^{\mathrm{T}}A)$	$1.9 \cdot 10^6$	$1.5 \cdot 10^6$	$1.1 \cdot 10^6$	$2.0 \cdot 10^6$
α	$3.3 \cdot 10^{-3}$	$6.1 \cdot 10^{-3}$	$5.9 \cdot 10^{-3}$	$2.8 \cdot 10^{-3}$
$\mathrm{cond}(\alpha I + A^{\mathrm{T}}A)$	51.5	26.0	25.1	45.8

Table 7.1: Regularization parameter α and condition numbers for the unfolding of low Q^2 data with the LEP energy given in the first line.

	189 GeV	196 GeV	200 GeV	205 − 207 GeV
Matrix build from GRV-LO Monte Carlo sample				
$\mathrm{cond}(A^{\mathrm{T}}A)$	$3.9 \cdot 10^4$	$4.1 \cdot 10^4$	$8.7 \cdot 10^4$	$8.0 \cdot 10^4$
α	$4.2 \cdot 10^{-3}$	$7.4 \cdot 10^{-3}$	$3.8 \cdot 10^{-3}$	$3.9 \cdot 10^{-3}$
$\mathrm{cond}(\alpha I + A^{\mathrm{T}}A)$	54.4	31.1	61.4	64.6
Matrix build from SaS-1D Monte Carlo sample				
$\mathrm{cond}(A^{\mathrm{T}}A)$	$1.8 \cdot 10^4$	$2.3 \cdot 10^4$	$2.2 \cdot 10^4$	$1.9 \cdot 10^4$
α	$4.8 \cdot 10^{-3}$	$8.0 \cdot 10^{-3}$	$4.7 \cdot 10^{-3}$	$4.9 \cdot 10^{-3}$
$\mathrm{cond}(\alpha I + A^{\mathrm{T}}A)$	49.6	29.3	50.0	52.2

Table 7.2: Same as Tab.7.1 but for high Q^2 data.

7.3 Unfolded Distributions

The unfolded spectra $\mathrm{d}\sigma/\mathrm{d}x$ are shown in Fig.7.3 and 7.4 for low and high Q^2 events, respectively. Both detector-response matrices were used and the results are plotted into the same diagrams. The mean value of both results has been performed for later use in the calculation of the structure function. The error bars

represent the statistical and approximation error added in quadrature. No other systematic errors are included so far. They will be considered later. Especially the error introduced by the use of two different matrices has not been taken into account yet. Beside the unfolded spectra for the ALEPH data, the theoretical prediction of the differential cross section $\mathrm{d}\sigma/\mathrm{d}x$ is shown in the same diagrams as histograms with no error bars attached. The solid line represents the GRV-LO parametrization and the dashed lines again the prediction for the SaS-1D model.

7.4 Extraction of $F_2^\gamma(x, Q^2)$

The structure function F_2^γ can be extracted from the measured differential cross section with Eqn. (2.14). For a reference parametrization of the structure function, the differential cross section $\mathrm{d}\sigma/\mathrm{d}x$ can be calculated with Monte Carlo techniques, as is for instance done for the Monte Carlo sample that is used for constructing the detector-response matrix. With the formula

$$F_2^\gamma(x, \langle Q^2 \rangle)_{\mathrm{data}} = \frac{\left(\frac{\mathrm{d}\sigma}{\mathrm{d}x}\right)_{\mathrm{data}}}{\left(\frac{\mathrm{d}\sigma}{\mathrm{d}x}\right)_{\mathrm{ref}}} \cdot F_2^\gamma(x, \langle Q^2 \rangle)_{\mathrm{ref}}$$

the hadronic structure function is finally determined. In this analysis the two models GRV-LO and SaS-1D are used as references, the mean of both distributions $F_2^\gamma(x, \langle Q^2 \rangle)_{\mathrm{data}}$ is taken as the final result. Half of the difference between them is taken into account as a systematic error. Fig. 7.5 and 7.6 show the results for both Q^2 ranges analyzed and for all centre-of-mass energies separately. The inner error bars show statistical errors only, the systematic errors taken into account are the approximation error from regularization and the error introduced by different reference distribution and unfolding matrices.

7.5 Systematic Uncertainties

The most important systematic uncertainty arises from the regularization in the unfolding. It has been discussed in chapter 4.

It has to be stressed that although the number of observed events is larger for higher x, the approximation uncertainty dominates the error in that region compared to low x because the visible hadronic invariant mass $W_{\gamma\gamma}$ is usually less than the value generated and $W_{\gamma\gamma}$ is especially large for low x events. Therefore low x events might be shifted and thus be observed with higher x values but the detector simulation accounts for that. For high x events the situation is worse because these are frequently lost completely.

Further effects give rize to additional systematic errors: The detector-response matrix is not independent of the model used to generate it. The unfolding is done separately with matrices from two different models and the mean of both results is taken as the final result. Half the difference of the two separate results is taken as a systematic error. Limited Monte Carlo statistics for the construction of the matrix is found to give a non negligible effect. It is not treated as a systematic uncertainty but as a part of the statistical error because it can be calculated in terms of error propagation as done in Appendix A.

The energy and momentum calibration of the detector was detuned artificially by $\pm 2\%$ for all particles in the hadronic system. The effect has only minor influence on the results ($< 2\%$) since the major uncertainty in the measurement of the hadronic system comes from lost tracks rather than from the resolution of the tracking devices and calorimeters. The variation was added to the systematic error.

The virtuality of the target photon is small but not vanishing. In the Monte Carlo generated by HERWIG it is produced with $\langle P^2 \rangle \approx 0.45\,\mathrm{GeV}^2$. The shape of the virtuality spectrum of the quasi real target photon can be taken as a ρ pole as the simplest vector meson or from the generalized vector meson dominance model (GVMD), and the effect on the result then be computed with the GALUGA [69] program. The uncertainty is 2-5%, depending slightly on x.

All systematic uncertainties and the statistical error are added in quadrature to obtain the total error plotted in Fig. 7.5 and 7.6.

7.6 Results

The structure function F_2^γ measured in this way is shown in Fig. 7.7 for both regions in Q^2. The unfolded spectra from all different centre-of-mass energies are combined. The inner marks on the error bars indicate the statistical errors, the whole error bars show systematic and statistical errors added in quadrature. The horizontal bars are the bin widths. A more detailed list of particular values for different uncertainties can be found in Tab. 7.3. Due to the unfolding and the properties of the detector-response matrix the measured points of the structure function are highly correlated. The correlation matrices are given in Tab. 7.4.

The curves plotted show three examples of different models for a parametrization calculated from PDFLIB functions. For medium values of x the significance of this measurement is too low to distinguish between different models. The shape seems to be similar to the GRV-LO and SaS-1D but the absolute value is slightly higher. For low x, where the structure function is sensitive to the gluon content, the LAC1 parametrization seems to be clearly too high. Overall a GRV-

like parametrization seems to fit the data best. The calculations are done for a mass of the charm quark of $m_c = 1.4\,\mathrm{GeV}$.

7.7 Comparison to Other Experiments

Since the hadronic structure function of the photon was first measured by the PLUTO collaboration [70], many experiments have made contributions so that data are now available for F_2^γ in a wide range of Q^2. In Fig. 7.8 the ALEPH results from this analysis are plotted together with measurements which are comparable in $\langle Q^2 \rangle$ from OPAL ($\langle Q^2 \rangle = 17.8\,\mathrm{GeV}^2$) [71], TOPAZ ($\langle Q^2 \rangle = 16\,\mathrm{GeV}^2$) [72], L3 ($\langle Q^2 \rangle = 15.3\,\mathrm{GeV}^2$) [73], DELPHI ($\langle Q^2 \rangle = 13\,\mathrm{GeV}^2$) [74] and OPAL ($\langle Q^2 \rangle = 59\,\mathrm{GeV}^2$) [75], AMY ($\langle Q^2 \rangle = 73\,\mathrm{GeV}^2$) [76] and PLUTO ($\langle Q^2 \rangle = 45\,\mathrm{GeV}^2$) [77].

7.8 Q^2 Dependence

The Q^2 dependence of the structure function cannot be fitted to the measurement, since only two bins in Q^2 are considered. Usually the mean values of F_2^γ are compared for a medium x range. A value can be calculated for both Q^2 regions, but the uncertainties are large, especially for lower Q^2. The results from this measurement are

$$\begin{aligned} F_2^\gamma(0.1 \le x \le 0.5, \langle Q^2 \rangle = 17.3\,\mathrm{GeV}^2) &= 0.42 \pm 0.01\ (\mathrm{stat.}) \pm 0.10\ (\mathrm{sys.}), \\ F_2^\gamma(0.1 \le x \le 0.7, \langle Q^2 \rangle = 67.2\,\mathrm{GeV}^2) &= 0.53 \pm 0.01\ (\mathrm{stat.}) \pm 0.05\ (\mathrm{sys.}). \end{aligned}$$

In Fig. 7.9 the results are shown in comparison to other experiments.

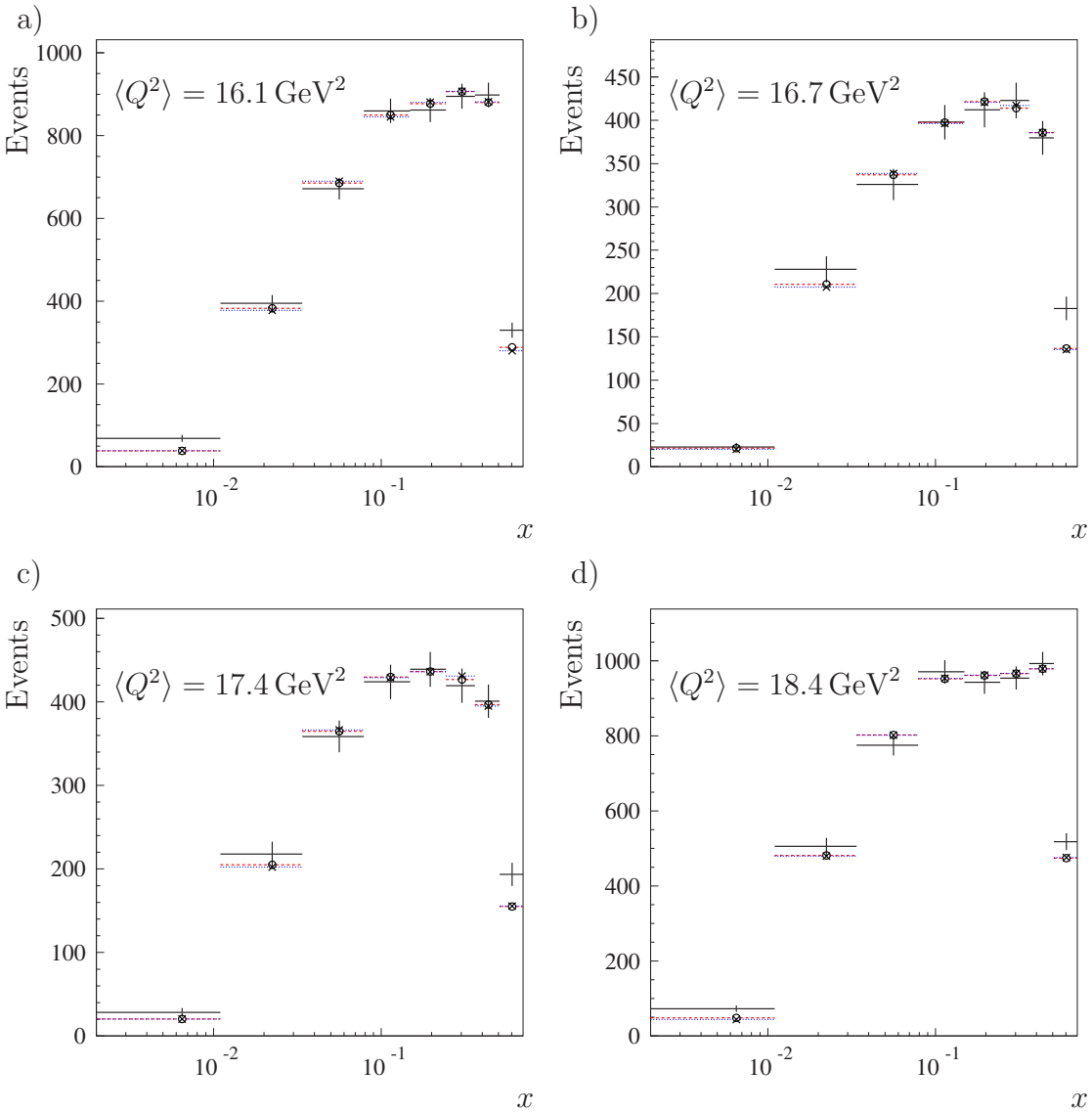

Figure 7.1: The histograms show the observed spectra of the Bjorken variable x for the low range of Q^2 and different centre-of-mass energies: a) $E_{\mathrm{cms}} = 189\,\mathrm{GeV}$, b) $E_{\mathrm{cms}} = 196\,\mathrm{GeV}$, c) $E_{\mathrm{cms}} = 200\,\mathrm{GeV}$ and d) $E_{\mathrm{cms}} = 205-207\,\mathrm{GeV}$. The mean value $\langle Q^2 \rangle$ is given in the histograms. The marks drawn with a solid line show the observed number of events in the original data sample after all cuts and background subtraction. The re-folded histograms are plotted in colored dashed and in dotted lines. The histogram that is obtained with an unfolding based on a response matrix built from a GRV-LO Monte Carlo (red) in addition is marked with a circle, the one obtained from a SaS-1D model (blue) is plotted with a small x.

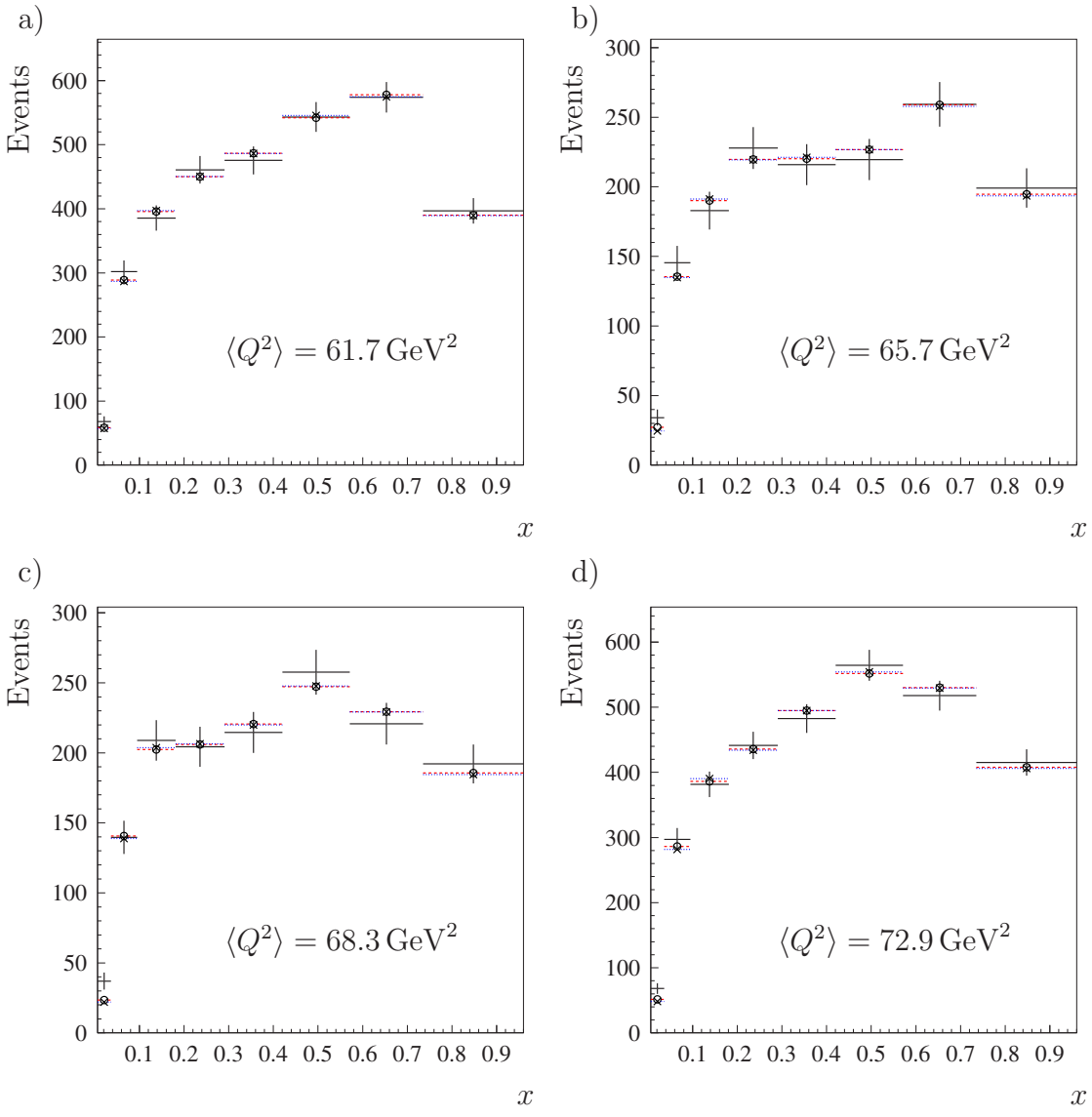

Figure 7.2: Same as in Fig.7.1 but for high values of $\langle Q^2 \rangle$

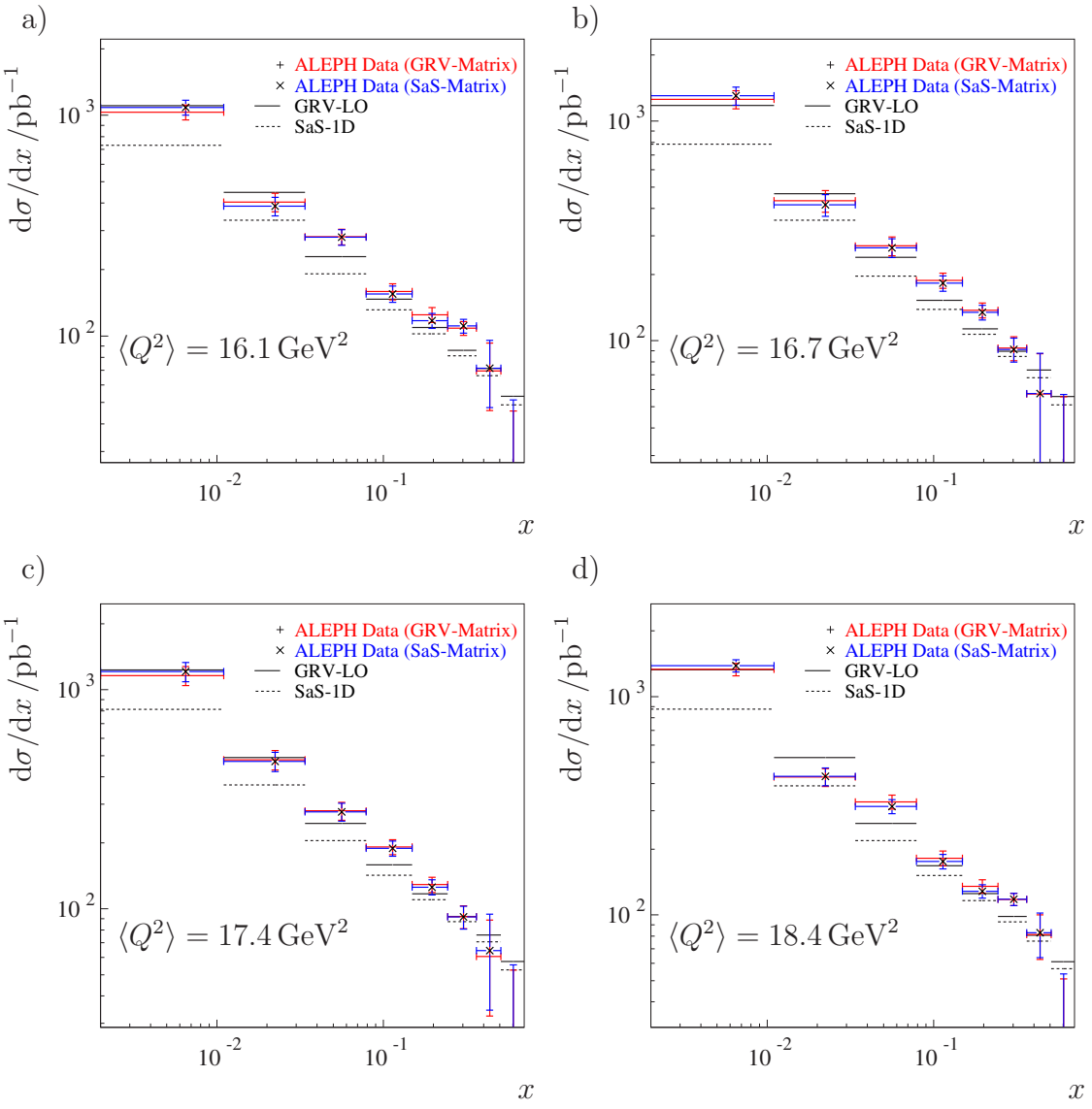

Figure 7.3: Differential cross section $\mathrm{d}\sigma/\mathrm{d}x$ as obtained after unfolding for the low range of Q^2 and different centre-of-mass energies: a) $E_{\mathrm{cms}} = 189\,\mathrm{GeV}$, b) $E_{\mathrm{cms}} = 196\,\mathrm{GeV}$, c) $E_{\mathrm{cms}} = 200\,\mathrm{GeV}$ and d) $E_{\mathrm{cms}} = 205 - 207\,\mathrm{GeV}$. The mean value $\langle Q^2\rangle$ is given in the histograms. No error bars are attached to the theoretical predictions. The solid error bars are plotted with the results obtained with a matrix constructed from the GRV-LO Monte Carlo. For the SaS-1D matrix the error bars are drawn with a dotted line. In addition the SaS-1D unfolded results are marked with a small x for better visibility.

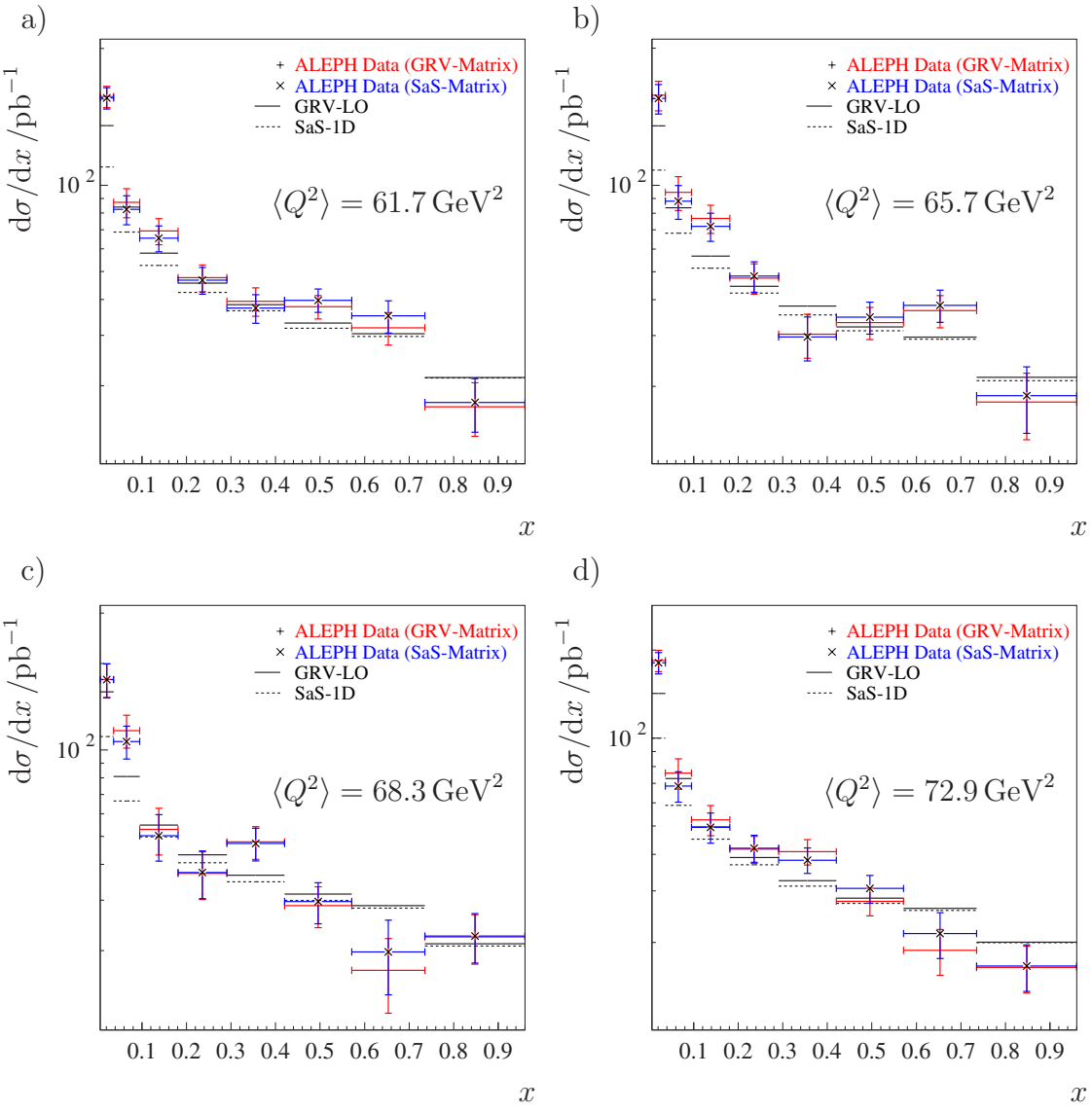

Figure 7.4: Same as in Fig.7.3 but for high values of $\langle Q^2 \rangle$

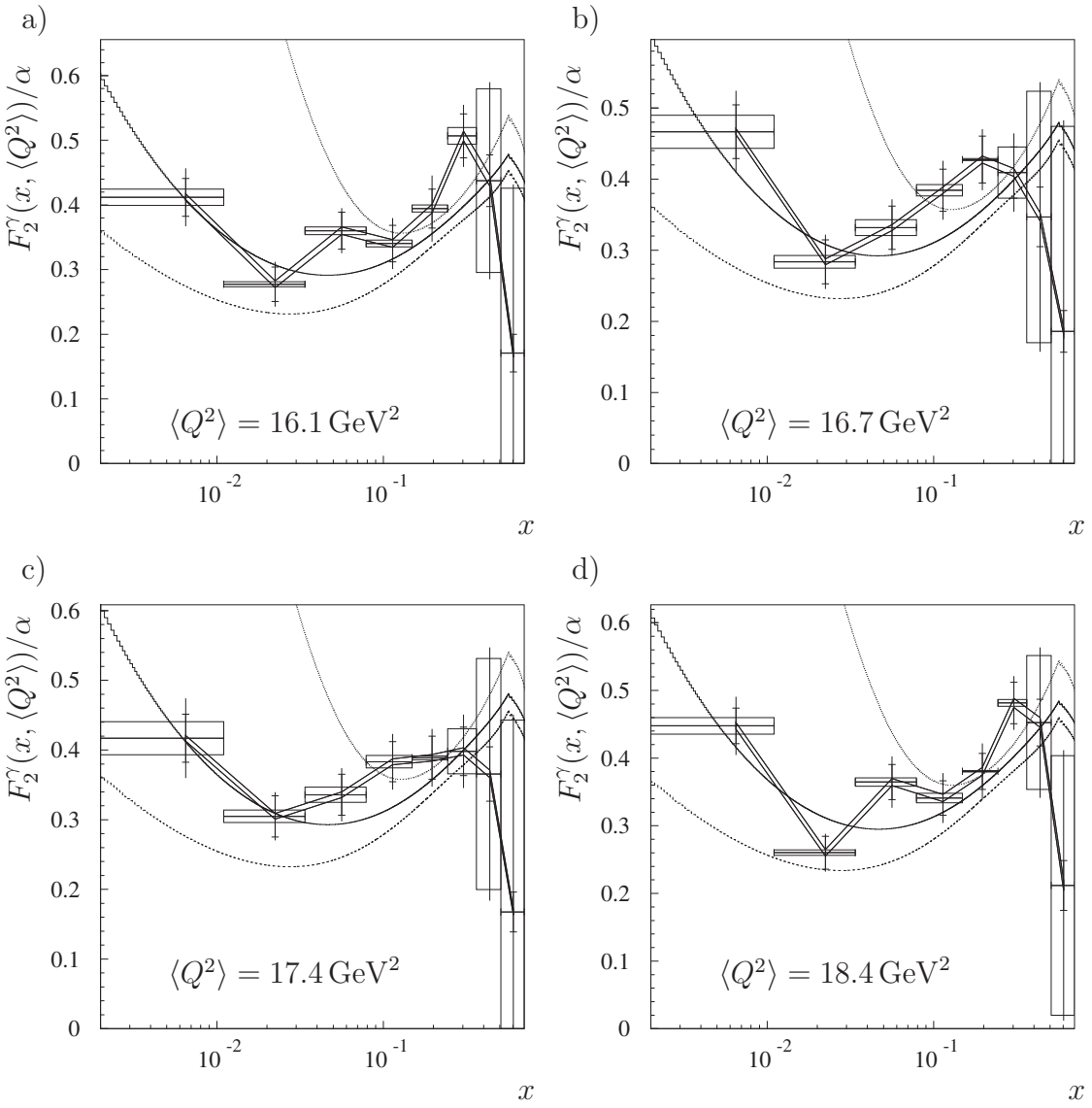

Figure 7.5: Final result for the hadronic structure function F_2^γ for low Q^2. The continous lines plotted are examples for theoretical predictions: GRV-LO parametrization is plotted as a solid line, the lower dashed line shows the structure function according the the SaS-1D set of parameters and the upper dotted line follow the LAC1 parametrization. The data are plotted with full uncertainty. Small inner error bars represent the statistical uncertainty and the error bars plotted as boxes exhibit the approximation error introduced by the regularization process. The additionally plotted lines that connect neighboring bins show the uncertainty from limited Monte Carlo statistics available for the construction of the detector-response matrix. Again the data sets collected at different LEP energies are presented separately: a) $E_{\mathrm{cms}} = 189\,\mathrm{GeV}$, b) $E_{\mathrm{cms}} = 196\,\mathrm{GeV}$, c) $E_{\mathrm{cms}} = 200\,\mathrm{GeV}$ and d) $E_{\mathrm{cms}} = 205 - 207\,\mathrm{GeV}$.

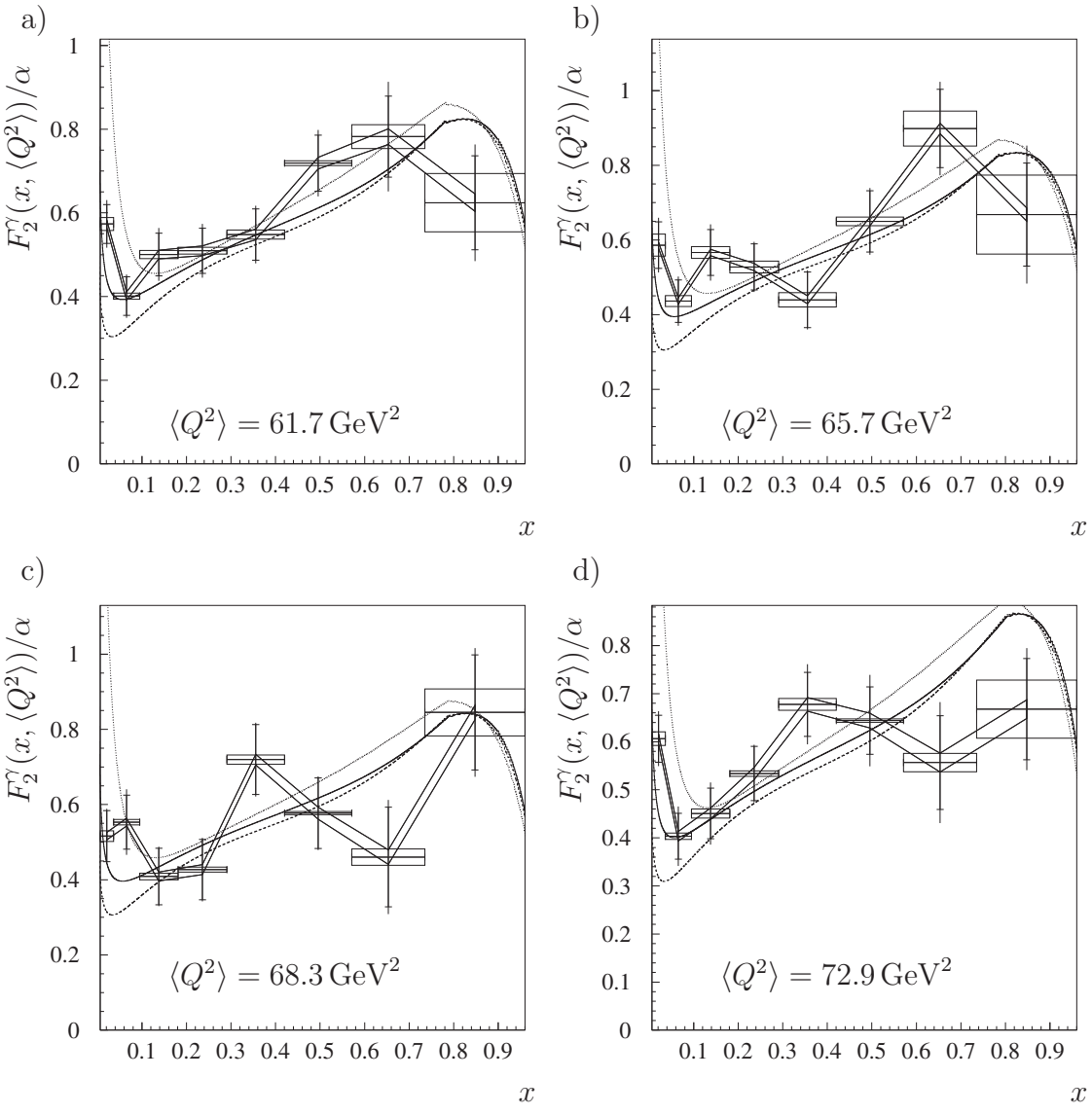

Figure 7.6: Same as in Fig.7.5 but for high values of $\langle Q^2\rangle$

$\langle Q^2 \rangle = 17.3\,\mathrm{GeV}^2$							
x Bin	F_2^γ	Uncertainties					
		Total	Stat.	System.	Approx.	Model	others
1	0.43	0.042	0.016	0.039	0.018	0.009	0.034
2	0.28	0.024	0.014	0.019	0.006	0.004	0.017
3	0.35	0.029	0.015	0.024	0.009	0.003	0.023
4	0.35	0.031	0.015	0.028	0.007	0.004	0.027
5	0.39	0.036	0.015	0.032	0.003	0.007	0.031
6	0.47	0.039	0.018	0.035	0.022	0.003	0.027
7	0.42	0.16	0.02	0.15	0.15	0.01	0.05
8	0.19	0.26	0.02	0.26	0.25	0.01	0.05

$\langle Q^2 \rangle = 67.2\,\mathrm{GeV}^2$							
x Bin	F_2^γ	Uncertainties					
		Total	Stat.	System.	Approx.	Model	others
1	0.58	0.042	0.027	0.031	0.018	0.007	0.025
2	0.43	0.045	0.027	0.037	0.009	0.017	0.031
3	0.48	0.046	0.030	0.036	0.011	0.014	0.031
4	0.51	0.041	0.031	0.027	0.009	0.003	0.025
5	0.61	0.051	0.037	0.035	0.014	0.010	0.031
6	0.66	0.058	0.039	0.043	0.006	0.020	0.037
7	0.67	0.10	0.05	0.08	0.03	0.03	0.06
8	0.68	0.11	0.06	0.09	0.08	0.01	0.05

Table 7.3: Measured values of F_2^γ and their uncertainties. The total error in column three is a quadratic sum of statistical and systematic errors, given in column four and five. The last three columns show contributions from the approximation error due to regularization, model dependence from different parametrizations in the Monte-Carlo simulations for the detector-response matrix and others like cut variations, energy and momentum resolution. These three errors add up in quadrature to the systematic error.

$\langle Q^2 \rangle = 17.3\,\mathrm{GeV}^2$								
x Bin	1	2	3	4	5	6	7	8
1	1.00	-0.49	0.05	0.13	-0.07	-0.03	0.02	0.01
2		1.00	-0.48	-0.13	0.26	-0.01	-0.08	-0.01
3			1.00	-0.33	-0.49	0.23	0.16	-0.04
4				1.00	0.02	-0.66	-0.01	0.18
5					1.00	0.09	-0.64	-0.12
6						1.00	0.28	-0.47
7							1.00	0.30
8								1.00

$\langle Q^2 \rangle = 67.2\,\mathrm{GeV}^2$								
x Bin	1	2	3	4	5	6	7	8
1	1.00	-0.48	0.01	0.20	-0.11	-0.02	0.04	-0.02
2		1.00	-0.45	-0.28	0.32	-0.05	-0.07	0.04
3			1.00	-0.23	-0.52	0.34	0.01	-0.05
4				1.00	-0.12	-0.70	0.39	-0.12
5					1.00	0.02	-0.71	0.43
6						1.00	-0.10	-0.32
7							1.00	-0.51
8								1.00

Table 7.4: Correlation coefficients for the results of the F_2^γ measurement.

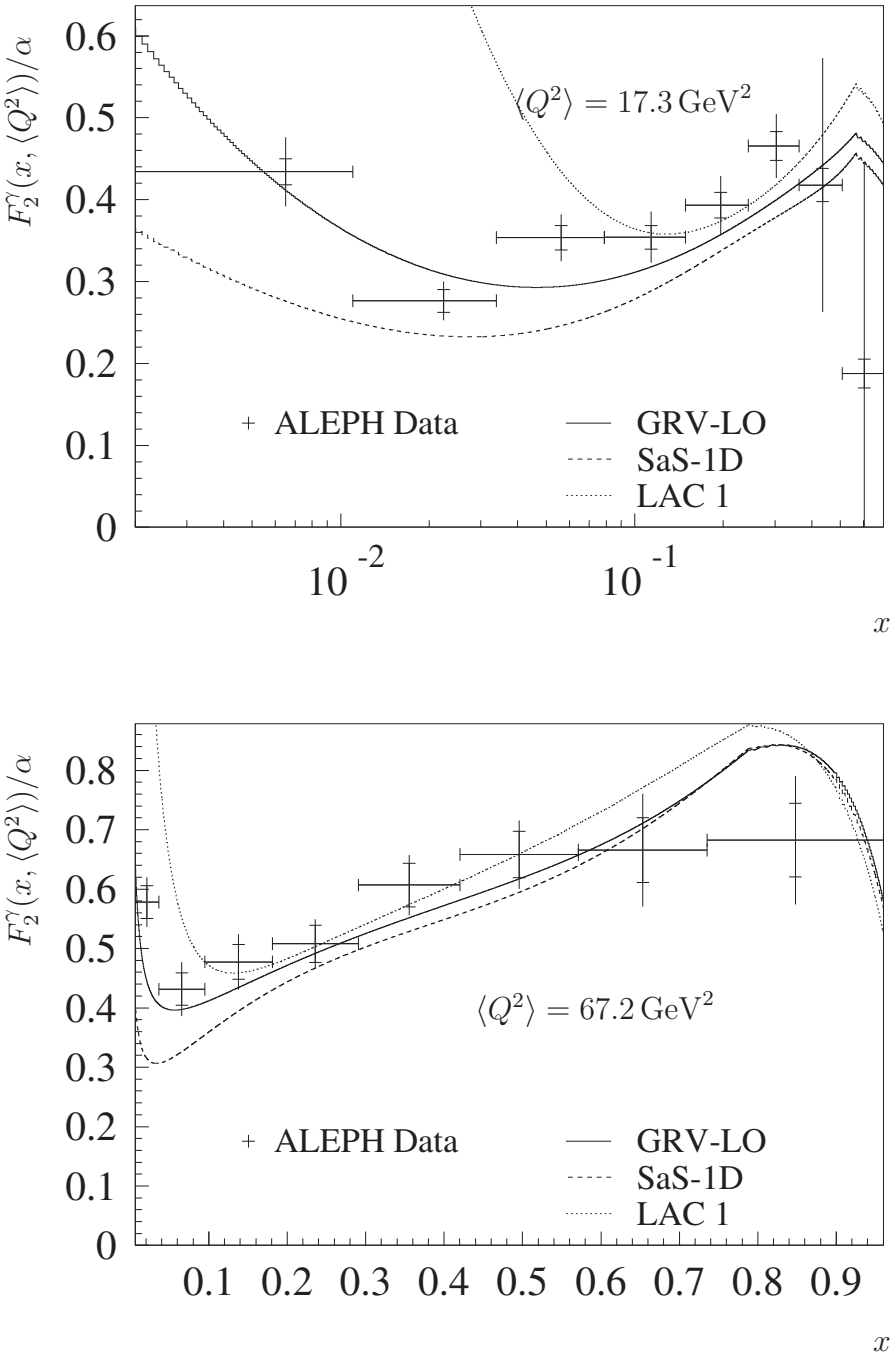

Figure 7.7: Final results for the measurement of the hadronic structure function $F_2^\gamma(x,\langle Q^2\rangle)/\alpha$ from ALEPH data. Statistical and systematic uncertainties are added up in quadrature for the outer error bars. The inner error bars exhibit statistical uncertainties only.

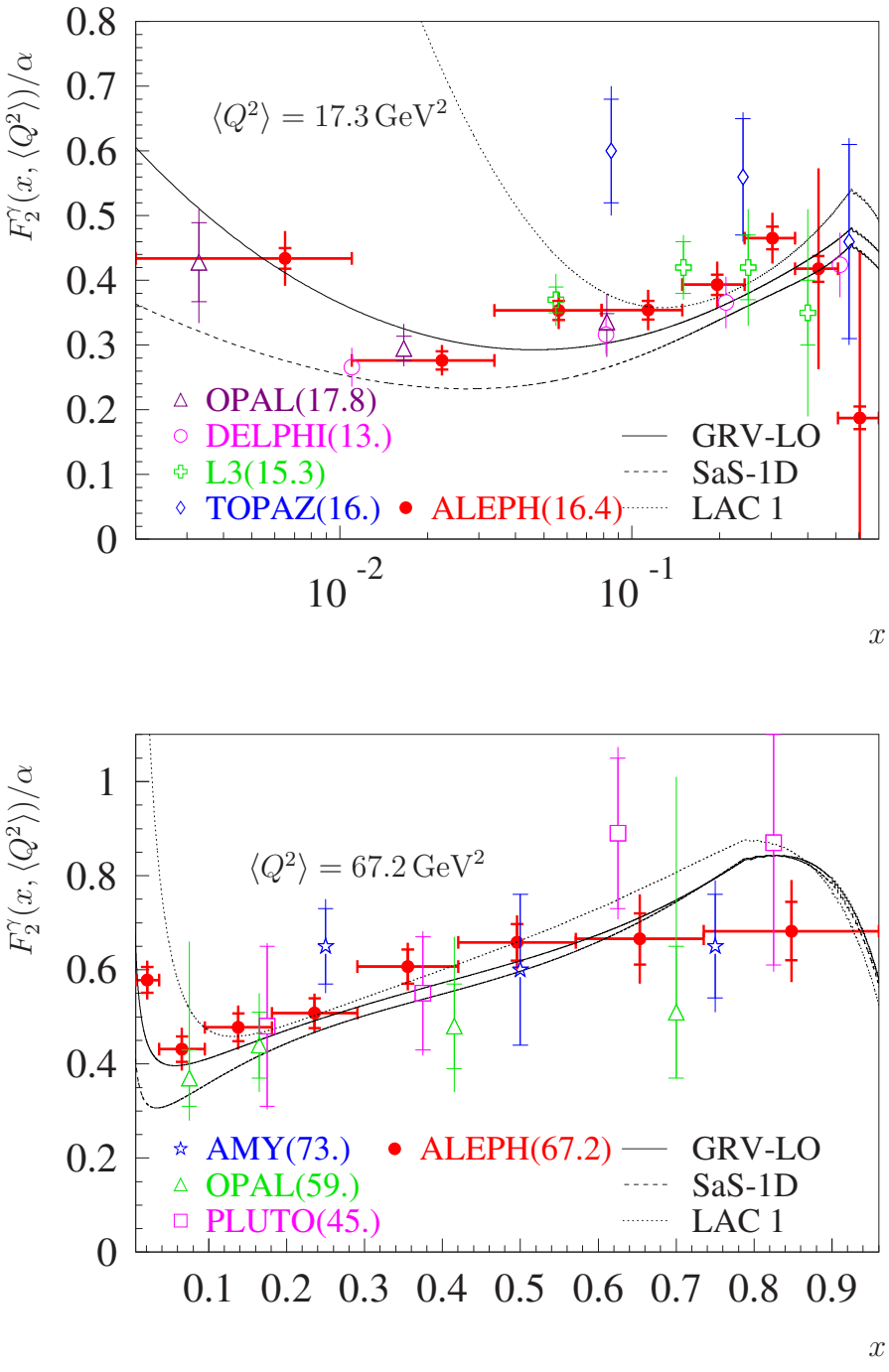

Figure 7.8: Final results for the measurement of the hadronic structure function $F_2^\gamma(x,\langle Q^2\rangle)/\alpha$ from ALEPH data in comparison to the results from other experiments.

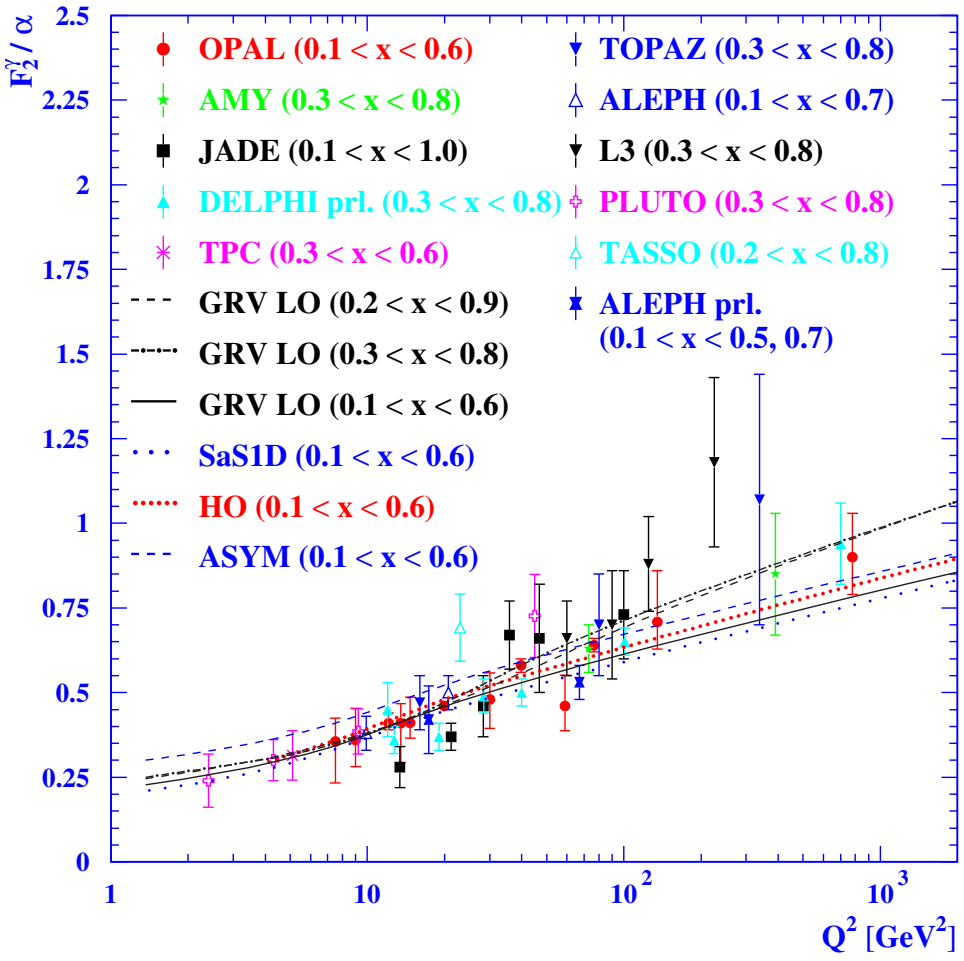

Figure 7.9: Q^2 evolution for medium values of x measured by different experiments. The results from this analysis is included for both bins in Q^2. Details about the plotted parameterisations are given in [13] where this plot was taken from. The plot is updated with our measurements denoted as ALEPH prl.

Chapter 8

Conclusions

A measurement of the hadronic structure function $F_2^\gamma(x, Q^2)$ has been performed with data taken by the ALEPH Collaboration in the years 1998 to 2000. At LEP centre-of-mass energies between 189 GeV and 207 GeV an integrated luminosity of $548.4\,\mathrm{pb}^{-1}$ has been analyzed in two bins of the virtuality Q^2. 15567 single-tag $\gamma^*\gamma$ events were selected in the low Q^2 region with $\langle Q^2 \rangle = 17.3\,\mathrm{GeV}^2$ and 9334 events at high Q^2 with $\langle Q^2 \rangle = 67.2\,\mathrm{GeV}^2$.

The properties of the selected events are compared to Monte-Carlo calculations. The simulation has been done with the HERWIG generator in version 6.2. Sets of Monte-Carlo events have been produced with two different theoretical models for the structure function F_2^γ, GRV-LO and SaS-1D. The distribution of important event variables are reasonably well reproduced by these Monte-Carlo calculations.

A regularized Tikhonov unfolding technique has been applied to correct for the detector acceptance and efficiency. It has been shown, that this method is suitable for the purpose of this analysis and delivers stable and reliable results. Emphasis is put on a complete treatment of statistical and systematic uncertainties including the matrix error and the approximation uncertainty that is necessarily introduced by the regularization. The detector-response matrix has been built from the HERWIG Monte-Carlo samples.

The final results show reasonable agreement with the GRV-LO model, although the absolute value of the measured cross section is slightly higher than predicted. The SaS-1D model predicts an even lower cross section but describes the overall shape quite well, too. Models for the parton density function that predict a relatively large gluon content are not consistent with data in the low x region. For medium and high values of the Bjorken variable x, the precision of the measurement does not allow to reject a particular model. Many more models with similar behavior are available which are not mentioned explicitly.

The Q^2 dependence of the structure function F_2^γ at medium values of x could only be compared to theoretical predictions and measurements from other experiments. The results obtained here agree within their uncertainties with available fits and measurements.

Appendix A

Full Error Propagation Including Matrix Uncertainties

For a matrix[1] A that is given with a limited accuracy, the uncertainty δA of the Matrix A has to be taken into account to calculate the statistical uncertainty of the solution $\mathbf{x}$ of the linear equation

$$A\mathbf{x} = \mathbf{y}. \tag{A.1}$$

Also the vector $\mathbf{y}$ is only known with a limited accuracy $\delta\mathbf{y}$. The matrix has to be written as $A = A_0 + \delta A$ and the first higher order, that does not vanish, is calculated for the approximation of the inverse matrix. For the solution of the Eqn. (A.1) one obtains

$$\begin{aligned}
\mathbf{x} &= A^{-1}\mathbf{y} \\
&= (A_0 + \delta A)^{-1}\mathbf{y} \\
&= \left[A_0\left(1 + A_0^{-1}\delta A\right)\right]^{-1}\mathbf{y} \\
&= \left(1 + A_0^{-1}\delta A\right)^{-1} A_0^{-1}\mathbf{y} \\
&\approx \left(1 - A_0^{-1}\delta A\right) A_0^{-1}\mathbf{y}
\end{aligned}$$

The covariance matrix C_x is then given as an expectation value $E_{y,\delta A}$ depending on the two uncertainties δA and $\delta\mathbf{y}$. The expectation value of the vector $\mathbf{y}$ is denoted by $\bar{\mathbf{y}}$.

$$\begin{aligned}
C_x &= E_{y,\delta A}\left(\left(A^{-1}\mathbf{y} - A_0^{-1}\bar{\mathbf{y}}\right)\left(\mathbf{y}^{\mathrm{T}}A^{-1\,\mathrm{T}} - \bar{\mathbf{y}}^{\mathrm{T}}A_0^{-1\,\mathrm{T}}\right)\right) \\
&\approx E_{y,\delta A}\left(\left[\left(1 - A_0^{-1}\delta A\right)A_0^{-1}\mathbf{y} - A_0^{-1}\bar{\mathbf{y}}\right]\right.
\end{aligned}$$

[1] The importance of the invertibility of the matrix A is briefly discussed in the first paragraph of section 4.4. All calculations performed here are correct with the provisions pointed out there.

$$
\begin{aligned}
&\left[\mathbf{y}^{\mathrm{T}} A_0^{-1\,\mathrm{T}} \left(1 - \delta A^{\mathrm{T}} A_0^{-1\,\mathrm{T}}\right) - \bar{\mathbf{y}}^{\mathrm{T}} A_0^{-1\,\mathrm{T}}\right]\Big) \\
= \;& E_y\left(A_0^{-1}(\mathbf{y}-\bar{\mathbf{y}})(\mathbf{y}-\bar{\mathbf{y}})^{\mathrm{T}} A_0^{-1\,\mathrm{T}}\right) + \\
& + E_{y,\delta A}\left(A_0^{-1}(\delta A A_0^{-1}\mathbf{y}\bar{\mathbf{y}} A_0^{-1\,\mathrm{T}}\delta A^{\mathrm{T}} A_0^{-1\,\mathrm{T}}\right) \\
= \;& A_0^{-1} E_y\left((\mathbf{y}-\bar{\mathbf{y}})(\mathbf{y}-\bar{\mathbf{y}})^{\mathrm{T}}\right) A_0^{-1\,\mathrm{T}} + \\
& + A_0^{-1} E_{y,\delta A}\left(\delta A A_0^{-1}\mathbf{y}\bar{\mathbf{y}} A_0^{-1\,\mathrm{T}}\delta A^{\mathrm{T}}\right) A_0^{-1\,\mathrm{T}} \\
= \;& A_0^{-1} C_y A_0^{-1\,\mathrm{T}} + A_0^{-1} E_{\delta A}\left(\delta A A_0^{-1} E_y\left(\mathbf{y}\bar{\mathbf{y}}^{\mathrm{T}}\right) A_0^{-1\,\mathrm{T}}\delta A^{\mathrm{T}}\right) A_0^{-1\,\mathrm{T}} \\
= \;& A_0^{-1} C_y A_0^{-1\,\mathrm{T}} + A_0^{-1} E_{\delta A}\left(\delta A A_0^{-1}\left(\bar{\mathbf{y}}\bar{\mathbf{y}}^{\mathrm{T}} + C_y\right) A_0^{-1\,\mathrm{T}}\delta A^{\mathrm{T}}\right) A_0^{-1\,\mathrm{T}}
\end{aligned}
$$

$$
\begin{aligned}
E_{\delta A}\left(\sum_{k,l} \delta A_{ik} B_{kl} \delta A_{lj}^{\mathrm{T}}\right) &= \sum_{k,l} B_{kl}\delta_{ij}\delta_{kl}\sigma^2(A_{ik}) \\
&= \delta_{ij}\sum_k B_{kk}\sigma^2(A_{ik}) \\
B &= A_0^{-1}\left(\bar{\mathbf{y}}\bar{\mathbf{y}}^{\mathrm{T}} + C_y\right) A_0^{-1\,\mathrm{T}}
\end{aligned}
$$

$$
\begin{aligned}
C_x &= \underbrace{A_0^{-1} C_y A_0^{-1\,\mathrm{T}}}_{=:\, C_x^{(1)}} + \\
&\quad + A_0^{-1}\Bigg(\delta_{ij}\sum_k \Bigg[\underbrace{\left(A_0^{-1}\left(\bar{\mathbf{y}}\bar{\mathbf{y}}^{\mathrm{T}} + C_y\right) A_0^{-1\,\mathrm{T}}\right)_{kk}}_{\left(\bar{\mathbf{x}}\bar{\mathbf{x}}^{\mathrm{T}} + A_0^{-1} C_y A_0^{-1\,\mathrm{T}}\right)_{kk}} \sigma^2(A_{ik})\Bigg]\Bigg) A_0^{-1\,\mathrm{T}} \\
&= C_x^{(1)} + A_0^{-1}\left(\delta_{ij}\sum_k \left[\left(\bar{\mathbf{x}}_k^2 + \left(C_x^{(1)}\right)_{kk}\right)\sigma^2(A_{ik})\right]\right) A_0^{-1\,\mathrm{T}} \\
&= C_x^{(1)} + A_0^{-1}\left(\delta_{ij}\sum_k \left[\left(\bar{\mathbf{x}}_k^2 + \left(\sigma_k^{(1)}\right)^2\right)\sigma^2(A_{ik})\right]\right) A_0^{-1\,\mathrm{T}} \qquad \text{(A.2)}
\end{aligned}
$$

The assumption has been made that the matrix elements A_{ij} are uncorrelated and their probability density function is Gaussian. In the case of a standard Tikhonov unfolding, the solution $\mathbf{x}$ solves the equation

$$\left(\alpha I + A^{\mathrm{T}} A\right)\mathbf{x} = A^{\mathrm{T}}\mathbf{y}$$

where α is the regularization parameter. Eqn. (A.1) is replaced by

$$R\mathbf{x} = \mathbf{y} \qquad \text{(A.3)}$$

with

$$R = A^{-1\,\mathrm{T}}\left(\alpha I + A^{\mathrm{T}} A\right).$$

To calculate the influence of the uncertainties in A on the final regularized result, R^{-1} has to be expanded into a series in A around the point

$$R_0 = A_0^{-1\,\mathrm{T}} \left(\alpha I + A_0^{\mathrm{T}} A_0\right) = \left(\alpha A_0^{-1\,\mathrm{T}} + A_0\right).$$

Terms that are of higher order in δA are neglected.

$$\begin{aligned} R &= \alpha A_0^{-1\,\mathrm{T}} + A_0 \\ &\approx \alpha \left(A_0^{-1\,\mathrm{T}} - A_0^{-1\,\mathrm{T}} \delta A^{\mathrm{T}} A_0^{-1\,\mathrm{T}}\right) + A_0 + \delta A \\ &= R_0 + \left(\delta A - \alpha A_0^{-1\,\mathrm{T}} \delta A^{\mathrm{T}} A_0^{-1\,\mathrm{T}}\right) \\ &= R_0 + \left(\delta A - A_0^{-1\,\mathrm{T}} \delta A \left(R_0 - A_0\right)\right) \\ &= R_0 + \delta R \end{aligned}$$

The covariance matrix of the regularized solution $C_{x,\,\alpha}$ then writes as

$$\begin{aligned} C_{x,\,\alpha} &= E_{y,\,\delta A}\left(\left(R^{-1}\mathbf{y} - R_0^{-1}\bar{\mathbf{y}}\right)\left(\mathbf{y}^{\mathrm{T}} R^{-1\,\mathrm{T}} - \bar{\mathbf{y}}^{\mathrm{T}} R_0^{-1\,\mathrm{T}}\right)\right) \\ &= R_0^{-1} C_y R_0^{-1\,\mathrm{T}} + \\ &\quad R_0^{-1} E_{\delta A}\left(\delta R R_0^{-1}\left(\bar{\mathbf{y}}\bar{\mathbf{y}}^{\mathrm{T}} + C_y\right) R_0^{-1\,\mathrm{T}} \delta R^{\mathrm{T}}\right) R_0^{-1\,\mathrm{T}} \end{aligned}$$

where the part of the expectation value, that depends on the matrix uncertainty δA can be calculated like

$$\begin{aligned} &E_{\delta A}\left(\delta R R_0^{-1}\left(\bar{\mathbf{y}}\bar{\mathbf{y}}^{\mathrm{T}} + C_y\right) R_0^{-1\,\mathrm{T}} \delta R^{\mathrm{T}}\right) = \\ &= E_{\delta A}\left(\left(\delta A - A_0^{-1\,\mathrm{T}} \delta A \left(R_0 - A_0\right)\right) R_0^{-1}\left(\bar{\mathbf{y}}\bar{\mathbf{y}}^{\mathrm{T}} + C_y\right) R_0^{-1\,\mathrm{T}}\right. \\ &\qquad \left.\left(\delta A^{\mathrm{T}} - \left(R_0^{\mathrm{T}} - A_0^{\mathrm{T}}\right)\delta A A_0^{-1}\right)\right) \\ &= E_{\delta A}\left(\delta A R_0^{-1}\left(\bar{\mathbf{y}}\bar{\mathbf{y}}^{\mathrm{T}} + C_y\right) R_0^{-1\,\mathrm{T}} \delta A^{\mathrm{T}}\right) + \\ &\quad + E_{\delta A}\left(A_0^{-1\,\mathrm{T}} \delta A^{\mathrm{T}}\left(R_0^{\mathrm{T}} - A_0^{\mathrm{T}}\right) R_0^{-1}\left(\bar{\mathbf{y}}\bar{\mathbf{y}}^{\mathrm{T}} + C_y\right) R_0^{-1\,\mathrm{T}}\left(R_0^{\mathrm{T}} - A_0^{\mathrm{T}}\right)\delta A A_0^{-1}\right) - \\ &\quad - E_{\delta A}\left(\delta A R_0^{-1}\left(\bar{\mathbf{y}}\bar{\mathbf{y}}^{\mathrm{T}} + C_y\right) R_0^{-1\,\mathrm{T}}\left(R_0^{\mathrm{T}} - A_0^{\mathrm{T}}\right)\delta A A_0^{-1}\right) - \\ &\quad - E_{\delta A}\left(A_0^{-1\,\mathrm{T}} \delta A \left(R_0 - A_0\right) R_0^{-1}\left(\bar{\mathbf{y}}\bar{\mathbf{y}}^{\mathrm{T}} + C_y\right) R_0^{-1\,\mathrm{T}} \delta A^{\mathrm{T}}\right) \\ &= \delta_{ij} \sum_k \left(R_0^{-1}\left(\bar{\mathbf{y}}\bar{\mathbf{y}}^{\mathrm{T}} + C_y\right) R_0^{-1\,\mathrm{T}}\right)_{kk} \sigma^2(A_{ik}) + \\ &\quad + A_0^{-1\,\mathrm{T}} \delta_{ij} \sum_k \left(A_0 R_0^{-1} - 1\right)\left(\bar{\mathbf{y}}\bar{\mathbf{y}}^{\mathrm{T}} + C_y\right)\left(R_0^{-1\,\mathrm{T}} A_0^{\mathrm{T}} - 1\right)\sigma^2(A_{ki}) + \\ &\quad + \left(\left[R_0^{-1}\left(\bar{\mathbf{y}}\bar{\mathbf{y}}^{\mathrm{T}} + C_y\right)\left(R_0^{-1\,\mathrm{T}} A_0^{\mathrm{T}} - 1\right)\right]_{ji} \sigma^2(A_{ij})\right) A_0^{-1} + \\ &\quad + A_0^{-1\,\mathrm{T}}\left(\left[\left(A_0 R_0^{-1} - 1\right)\left(\bar{\mathbf{y}}\bar{\mathbf{y}}^{\mathrm{T}} + C_y\right) R_0^{-1\,\mathrm{T}}\right]_{ji} \sigma^2(A_{ji})\right). \end{aligned}$$

Finally the complete covariance matrix C_x is given by

$$
\begin{aligned}
C_{x,\alpha} \;=\; & R_0^{-1} C_y R_0^{-1\,\mathrm{T}} + \\
& + R_0^{-1} \left(\delta_{ij} \sum_k \left(R_0^{-1} \left(\bar{\mathbf{y}} \bar{\mathbf{y}}^{\mathrm{T}} + C_y \right) R_0^{-1\,\mathrm{T}} \right)_{kk} \sigma^2(A_{ik}) \right) R_0^{-1\,\mathrm{T}} + \\
& + R_0^{-1} A_0^{-1\,\mathrm{T}} \\
& \quad \left(\delta_{ij} \sum_k \left(A_0 R_0^{-1} - 1 \right) \left(\bar{\mathbf{y}} \bar{\mathbf{y}}^{\mathrm{T}} + C_y \right) \left(R_0^{-1\,\mathrm{T}} A_0^{\mathrm{T}} - 1 \right) \sigma^2(A_{ki}) \right) \\
& \qquad A_0^{-1} R_0^{-1\,\mathrm{T}} + \\
& + R_0^{-1} \left(\left[R_0^{-1} \left(\bar{\mathbf{y}} \bar{\mathbf{y}}^{\mathrm{T}} + C_y \right) \left(R_0^{-1\,\mathrm{T}} A_0^{\mathrm{T}} - 1 \right) \right]_{ji} \sigma^2(A_{ij}) \right) A_0^{-1} R_0^{-1\,\mathrm{T}} + \\
& + R_0^{-1} A_0^{-1\,\mathrm{T}} \left(\left[\left(A_0 R_0^{-1} - 1 \right) \left(\bar{\mathbf{y}} \bar{\mathbf{y}}^{\mathrm{T}} + C_y \right) R_0^{-1\,\mathrm{T}} \right]_{ji} \sigma^2(A_{ji}) \right) R_0^{-1\,\mathrm{T}}
\end{aligned}
$$

Appendix B

Test of the Unfolding Procedure

The complete unfolding procedure has been performed on Monte Carlo test samples. For each centre–of–mass energy and Q^2 region, samples of the size of the real data sample have been treated in the same way as data. In particular, they are also unfolded with the use of detector-response matrices which were not build from the same model. All tests were successful. The method can be considered as reliable and stable for our purpose. In Fig. B.1 and B.2 the final results are shown for low and high Q^2 region and both input structure functions. As systematic uncertainties the approximation error as well as the uncertainty introduced by the use of different matrices are taken into account. The full statistical error is calculated and given by the inner error bars. In all cases the results are consistent with the theoretical model.

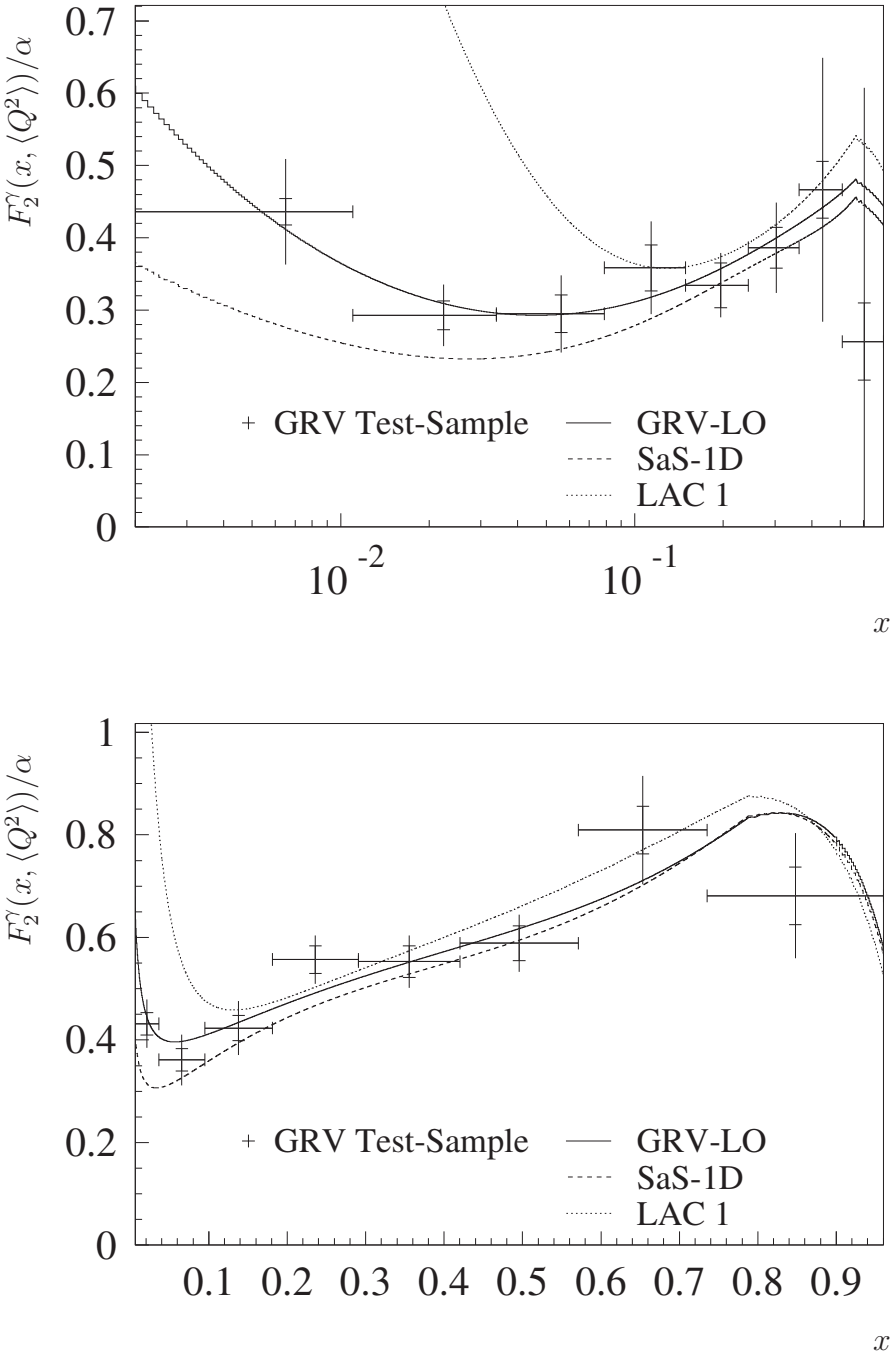

Figure B.1: Reconstruction of the photon structure function from a small GRV-LO Monte Carlo sample. The same number of events as in data have been randomly chosen for all centre-of-mass energies and treated like data through the complete process of the analysis. After the final combination the original structure function is consistent with the results within the experimental uncertainties. Total and statistical uncertainties are plotted.

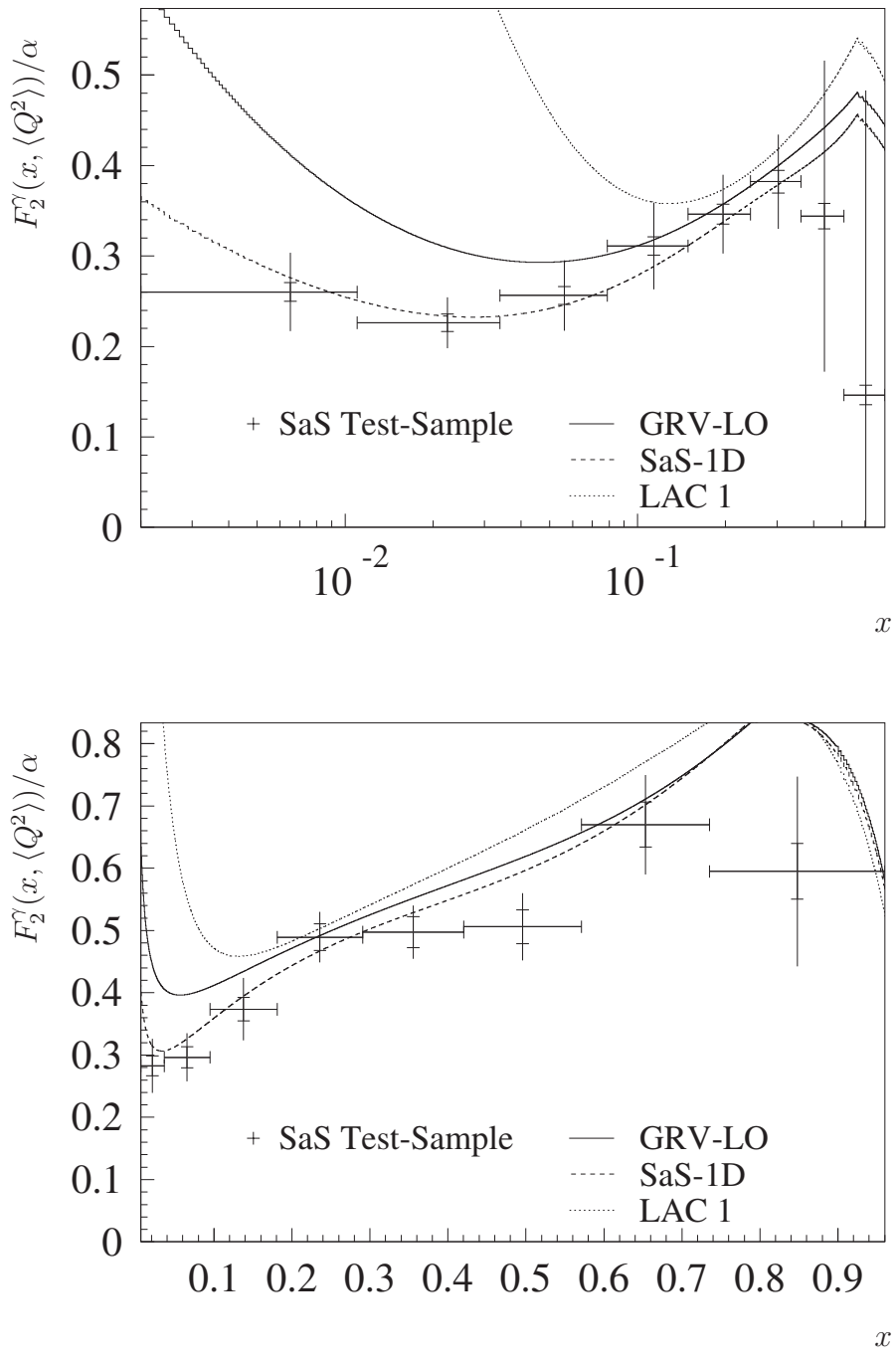

Figure B.2: Same test as in Fig. B.1 but performed with a SaS-1D Monte Carlo sample.

Bibliography

[1] V. M. Budnev, I. F. Ginzburg, G. V. Meledin, V. G. Serbo, Phys. Rep., **C15** (1975) 181-282.

[2] P. Kessler, Il Nuovo Cimento **17** (1960) 809-828.

[3] C. F. von Weizsäcker, Z. Phys., **88** (1934) 612-625.

[4] E. J. Williams, Phys. Rev., **45** (1934) 729-730.

[5] S. Frixione, M. L. Mangano, P. Nason and G. Ridolfi, Phys . Lett., **B319** (1993) 339-345.

[6] M. Dress, R. M. Godbole, Phys. Rev., **D50** (1994) 3124.

[7] G. A. Schuler, CERN-TH/96-297, hep-ph/9610406.

[8] M. Defrise, S. Ong, J. Silva and C. Carimalo, Phys. Rev., **D23** (1981) 663-668.

[9] J. J. Sakurai, Ann. Phys., **11** (1960) 1.

[10] L. Stodolsky, Phys. Rev., **B134** (1964) 1099.

[11] J. J. Sakurai and D. Schildknecht, Phys. Lett., **B40** (1972) 121.

[12] T. H. Bauer, F. M. Pipkin, R. D. Spital and D. R. Yennie, Rev. Mod. Phys., **50** (1978) 261.

[13] R. Nisius, "*The photon structure from deep inelastic electron-photon scattering*", Phys. Rep., **332** (2000) 165-317. updated figures available at: *http://www.mppmu.mpg.de/˜nisius/welcomeaux/struc.html*

[14] S. D. Drell and T. M. Yan, Phys. Rev. Lett., **25** (1970) 316.

[15] S. D. Drell and T. M. Yan, Phys. Rev. Lett., **66** (1971) 578.

[16] NA3 Collaboration, "*Experimental Determination of the pi Meson Structure Functions by the Drell-Yan Mechanism*", Z. Phys., **C18** (1983) 281-287.

[17] C. Peterson, T. Walsh and P. M. Zerwas, Nucl. Phys., **B174** (1980) 424-444.

[18] C. Peterson, P. M. Zerwas and T. Walsh, Nucl. Phys., **B229** (1983) 301-316.

[19] D. W. Duke and J. F. Owens, Phys. Rev., **D22** (1980) 2280-2286.

[20] TPC/2γ Collaboration, "*Measurement of the Photon Structure Function* $F_2^\gamma(x, Q^2)$ *in the Region* $0.2 < Q^2 < 7, \mathrm{GeV}^2$ ", Z. Phys., **C34** (1987) 1-13.

[21] T. F. Walsh and P. Zerwas, Phys. Lett., **B44** (1973) 195.

[22] P. Zerwas, Phys. Rev., **D10** (1974) 1485.

[23] R. L. Kingsley, Nucl. Phys., **B60** (1973) 45.

[24] G. Altarelli and G. Parisi, Nucl. Phys., **B126** (1977) 298.

[25] Yu. L. Dokshitzer, Sov. Phys. JETP, **46** (1977) 641.

[26] L. N. Lipatov, Sov. J. Nucl. Phys., **15** (1972) 438.

[27] V. N. Gribov and L. N. Lipatov, Sov. J. Nucl. Phys., **15** (1972) 438.

[28] G. Altarelli, Phys. Rev., **81** (1982) 1.

[29] K. Hagiwara, M. Tanaka, I. Watanabe and T. Izubuchi, Phys. Rev., **D51** (1995) 3197-3219.

[30] E. Witten, Nucl. Phys., **B120** (1977) 189-202.

[31] M. Krawczyk, "*Structure Functions for the Virtual and Real Photons.*" In: A. J. Finch (Editor): Proceedings of PHOTON2000. Ambleside, England: AIP Conference Proceedings Vol. 571, Melville, New York (2000).

[32] H. Abramowicz, K. Charchula and A. Levy, Phys. Lett., **B269** (1991) 458-464.

[33] M. Drees and K. Grassie, Z. Phys., **C28** (1985) 451-462.

[34] M. Glück, E. Hoffmann and E. Reya, Z. Phys., **C13** (1982) 119-130.

[35] M. Glück, E. Reya and A. Vogt, Z. Phys., **C53** (1992) 651-655.

[36] M. Glück, E. Reya and A. Vogt, Z. Phys., **C53** (1992) 127.

[37] M. Glück, E. Reya and I. Schienbein, Eur. Phys. J., **C10** (1999) 313-317.

[38] H1 Collaboration, "*Measurement of the Proton Structure Function $F_2(x, Q^2)$ in the Low-x Region at HERA*", Nucl. Phys., **B407** (1993) 515-535.

[39] ZEUS Collaboration, "*Measurement of the Proton Structure Function F_2 in ep Scattering at HERA*", Phys. Lett., **B316** (1993) 412-426.

[40] E. Gotsman, A. Levy and U. Maor, Z. Phys., **C40** (1988) 117.

[41] G. A. Schuler and T. Sjöstrand, Z. Phys., **C68** (1995) 607-623.

[42] ALEPH Collaboration, "*ALEPH: a detector for electron-positron annihilation at LEP* ", Nucl. Inst. Meth., **A294** (1990) 121.

[43] ALEPH Collaboration, "*Performance of the ALEPH detector at LEP* ", Nucl. Inst. Meth., **A360** (1995) 481.

[44] C. Bowdery, "*ALEPH Handbook*", **Vol. 1**, Geneva: CERN, 1995.

[45] C. Bowdery, "*ALEPH Handbook*", **Vol. 2**, Geneva: CERN, 1997.

[46] Ngac An Bang, private communication.

[47] G. Cowan, "*Statistical Data Analysis*", Oxford: Clarendon Press, 1998.

[48] R. Kress, "*Numerical Analysis*", Graduate Texts in Mathematics, New York, Berlin a. o.: Springer-Verlag, 1997.

[49] H. W. Engl, M. Hanke and A. Neubauer, "*Regularization of Inverse Problems*", Dordrecht: Kluwer Academic Publishers, 1996.

[50] A. Ben-Israel and T. N. E. Greville, "*Generalized Inverses: Theory and Applications*", New York: John Wily & Sons, 1974.

[51] D. L. Phillips, "*A technique for the numerical solution of certain integral equations of the first kind*", J. ACM, **9** (1962) 84.

[52] A. N. Tikhonov, "*Regularization of incorrectly posed problems*", Soviet Math. Dokl. **4** (1963) 1624-1627.

[53] A. N. Tikhonov, "*Solution of incorrectly formulated problems and the regularization method*", Soviet Math. Dokl. **4** (1963) 1034-1038.

[54] C. E. Shannon, Bell Sys. Tech. J., **27** (1948) 379.

[55] K. Affholderbach, "*Messung der hadronischen Structur des Photons*", Fachbereich Physik, Universität Siegen, Ph.-D. Thesis (2000).

[56] G. Prange, "*Messung des hadronischen Wirkungsquerschnitts doppelt markierter 2-Photon Ereignisse*", Fachbereich Physik, Universität Siegen, Ph.-D. Thesis (2001).

[57] B. Bloch-Devaux, "*KINGAL User's Guide. (new version)*", ALEPH 91-082 PHYSIC 91-075, internal note (1991).

[58] E. Lange, "*An interface between Herwig and Kingal/Galeph.*", ALEPH 89-036 PHYSIC 89-012, internal note (1989).

[59] H. Plothow-Besch, "*PDFLIB Proton, Pion and Photon Parton Density Functions, Parton Density Functions of the Nucleus, and α_s Calculations*", Users's Manual, Version 8.04, CERN-ETT/TT (2000).

[60] G. Marchesini and B. R. Webber, Nucl. Phys., **B310** (1988) 461.

[61] I. G. Knowles, Nucl. Phys., **B310** (1988) 571.

[62] S. Catani, G. Marchesini and B. R. Webber, Nucl. Phys., **B349** (1991) 635.

[63] G. Abbiendi and L. Stanco, Comp. Phys. Commun., **66** (1991) 16.

[64] M. H. Seymour, Z. Phys., **C56** (1992) 161.

[65] G. Marchesini et al. , Comp. Phys. Commun., **67** (1992) 465.

[66] F. Ranjard, ALEPH 86-015, internal note (1986).

[67] CERN Program Library Long Writeup: "*GEANT: Detector Description and Simulation Tool.*" (1995).

[68] J. Knobloch, ALEPH 90-115, internal note (1990).

[69] G. A. Schuler, Comp. Phys. Commun., **108** (1998) 279.

[70] PLUTO Collaboration, "*First Measurement of the Photon Structure Function F_2* ", Phys. Lett., **107B** (1981) 168-172.

[71] OPAL Collaboration, "*Measurement of the low-x behaviour of the photon structure function F_2^γ*", Eur. Phys. J., **C18** (2000) 15-39.

[72] TOPAZ Collaboration, "*Measurement of the photon structure function F_2^γ and jet production at TRISTAN* ", Phys. Lett., **B332** (1994) 477-487.

[73] L3 Collaboration, "*The Q^2 evolution of the hadronic photon structure function F_2^γ at LEP* ", Phys. Lett., **B447** (1999) 147-156.

[74] I. Tyapkin, for the DELPHI Collaboration "*Study of the photon structure function F_2 at LEP1 and LEP2*", in: A. Buijs, F. C. Erneé (Eds.), Photon'97, Incorporating the XIth International Workshop on Gamma-Gamma Collisions, Egmond aan Zee, 10-15 May 1997, World Scientific, Singapore, 1998, 26-30.

[75] OPAL Collaboration, "*Measurement of the Q^2 Evolution of the Photon Structure Function F_2^γ* ", Phys. Lett., **B411** (1997) 387-401.

[76] AMY Collaboration, "*A measurement of the photon structure function F_2* ", Phys. Lett., **B252** (1990) 491-498.

[77] PLUTO Collaboration, "*Measurement and QCD Analysis of the Photon Structure Function $F_2^\gamma(x, Q^2)$* ", Nucl. Phys., **B281** (1987) 365-380.

[78] ALEPH Collaboration, "*Search for $\gamma\gamma \to \eta_b$ in e^+e^- collisions at LEP2* ", Phys. Lett., **B530** (2002) 56.

List of Tables

List of Figures

Acknowledgments

I am grateful to many people for their support during the last years. This analysis could not have been done without their contributions.

First I would like to thank Prof. Dr. Siegmund Brandt and Prof. Dr. Claus Grupen for the opportunity to work in their group and to get in touch with a fascinating experiment like ALEPH and the CERN institute. I enjoyed their continual support and encouragement.

Priv. Doz. Dr. Armin Böhrer was especially helpful during the whole period of my PhD. studies. He was permanently available for all kind of fruitful discussions about particle physics, $\gamma\gamma$-physics in particular, analysis techniques and further ideas. His enthusiasm for physics is enormous and he let us take part in it, especially his η_b-analysis [78] was great fun and instructive for me as his student.

Prof. Dr. Hans-Jürgen Reinhardt helped me kindly to find the appropriate mathematical techniques and was prepared to discuss the difficulties and specific problems that appeared. The communication with him was clarifying in many points.

I enjoyed the discussions about both, life and physics with Prof. Dr. Hans Dieter Dahmen. They lead to many new aspects.

It was a great pleasure and always fun to work in the ALEPH Collaboration, especially in the $\gamma\gamma$–working group. At first place I would like to thank Dr. Alex J. Finch for his patience and answers to many questions. The members of the ALEPH group in Siegen, Dr. Uwe Sieler, Dr. Gerrit Prange, Dipl.–Phys. Ngac An Bang, Dr. Klaus Affholderbach, Dr. Andrzej Misiejuk, Prof. Dr. Arif Mailov, Dipl.–Phys. Olaf Krasel, Dipl.–Phys. Andreea Koob, Rodica Tcaciuc, the cosmic ray community and the cryptograph Dipl.–Phys. Dieter Schmidt created a friendly environment where I enjoyed working and could get a lot of constructive support.

I am very thankful for all the help I got from Tilo Stroh. He certainly became more a friend than a colleague. The value of his support cannot be overestimated.

Outside the physics community I am especially obliged to my parents who made my studies possible and supported me in many different ways over the years.

Physics is nice, but life is much more: Thanks to all of my friends for the nice time outside the institute, and especially to Ute.